N73-31993

NATIONAL AERONAUTICS AND SPACE ADMINISTRATION

Technical Memorandum 33-626

Thermoelastic Analysis of Solar Cell Arrays and Their Material Properties

M. A. Salama
W. M. Rowe
R. K. Yasui

JET PROPULSION LABORATORY
CALIFORNIA INSTITUTE OF TECHNOLOGY
PASADENA, CALIFORNIA

September 1, 1973

NATIONAL AERONAUTICS AND SPACE ADMINISTRATION

Technical Memorandum 33-626

Thermoelastic Analysis of Solar Cell Arrays and Their Material Properties

M. A. Salama
W. M. Rowe
R. K. Yasui

JET PROPULSION LABORATORY
CALIFORNIA INSTITUTE OF TECHNOLOGY
PASADENA, CALIFORNIA

September 1, 1973

Prepared Under Contract No. NAS 7-100
National Aeronautics and Space Administration

PREFACE

The work described in this report was performed by the Engineering Mechanics and the Guidance and Control Divisions of the Jet Propulsion Laboratory.

ACKNOWLEDGMENT

The linear thermal expansion measurements described herein were performed by M. D. Campbell of Convair, a division of General Dynamics. The mechanical property tests on the silicon were performed by J. R. Brown of the Southern Research Institute. R. Hemmerlin of Magnaflux Testing Laboratories, Magnaflux Corporation, was responsible for the elastic modulus and ultimate strength tests on the RTV silicone adhesives. The Poisson's ratio test methods and determinations on the RTV silicone adhesives were done at the General Electric Company, Corporate Research and Development, by G. A. Mellinger and W. V. Olszewski. The mechanical property tests on the interconnect metals were performed by J. A. VanEcho and E. Swetnam of Battelle Institute, Columbus Laboratories.

The authors would also like to express their appreciation for the valuable advice and support provided by the JPL Staff. To mention only a few: J. V. Goldsmith, M. Trubert, C. Savage, R. G. Ross, C. Mosher, R. Mueller, R. Greenwood, W. Wall, J. Person, D. Ritchie, and W. Hasbach.

CONTENTS

CONTENTS (contd)

TABLES

FIGURES

CONTENTS (contd)

FIGURES (contd)

CONTENTS (contd)

FIGURES (contd)

CONTENTS (contd)

FIGURES (contd)

ABSTRACT

This report presents a thermoelastic stress analysis procedure for predicting the thermally induced stresses and failures in silicon solar cell arrays. A prerequisite for the analysis is the characterization of the temperature-dependent thermal and mechanical properties of the solar cell materials. Extensive material property testing was carried out in the temperature range -200 to +200°C for the filter glass, P- and N-type silicon, interconnector metals, solder, and several candidate silicone rubber adhesives. Results are included.

The analysis procedure is applied to several solar cell array design configurations, which were tested in the Space Molecular Sink. Results of the analysis indicate the optimum design configuration, with respect to compatible materials, effect of the solder coating, and effect of the interconnector geometry. Good agreement was found between results of the analysis and the test program.

I. INTRODUCTION

The present trends of solar cell array design emphasize, among other things, low cost, higher reliability, and longer lifetimes during which severe thermal changes may be expected. These trends have direct bearing on the design procedure and factors to be considered in seeking satisfactory designs. For example, it is well known that high numbers of thermal cycles and extreme thermal changes induce severe stresses that can cause serious failures in the components of solar cell arrays. The designer must, therefore, be able to reliably predict potential failures in a given design and correct them prior to proceeding further with a costly and elaborate test program.

Previous efforts in this direction are numerous. References 1 and 2 are cited here as examples. The analysis and failure prediction procedure described in Ref. 1 serves in many ways as a foundation for the present work. In absence of the material property data required for the analysis, several simplifying assumptions were made in Ref. 1. These involved material property values as well as simplifications in the method of analysis itself. The aim of this report is to improve the results of the analysis by using measured material properties and a more rigorous method of analysis, and to show the correlation between the analysis and results of tests made on a number of solar cell designs.

II. EXPERIMENTAL SAMPLE PANEL TEST PROGRAM

The analysis described in Section III was supported by an experimental test program to evaluate the various failure modes of new and past solar array designs. The purpose of the test program was to determine the capability of the various adhesives, interconnector geometries and materials, and both solderless and solder-coated cells to meet the thermal environment imposed on the solar cell array during the Viking Mars Orbiter 1975 (VO'75) mission. Because a separate report is presently being prepared, which will cover this area in greater detail, only highlights which depict typical failure modes during testing will be discussed.

A. Sample Panel Description and Test Procedure

Five separate sample panels, each consisting of various candidate solar array designs were assembled for this evaluation. The substrate of each sample panel is a representative section of an actual Viking solar panel substrate. The nominal dimensions of each section are 35.6 cm by 35.6 cm (14 by 14 in.) by 1.3 cm (0.5 in.) thick. Each sample panel is comprised of various components and candidate materials. Fig. 1 shows a layout of one of the five sample panels. Figures 2 to 5 show some of the solar cell configurations which are referenced in Fig. 1.

The test plan for the sample panels consisted of thermal cycling over the range of temperature indicated in Fig. 6, which depicts the predicted VO'75 cell temperature profile during sun occultation. Sixty such cycles (orbits) are predicted. Each of the five panels was tested separately in the Space Molecular Sink, commonly referred to as the Molsink. Figure 7 shows a sample panel suspended near the honeycomb spherical shroud, which is cooled by liquid helium. The front (or active) cell surface of the panel is heated using tungsten radiant wire heaters to induce the proper thermal profile. A vacuum pressure of 0.013×10^{-5} N/cm^2 (10^{-5} torr) was maintained throughout the testing period. Visual inspection (× 20) and electrical performance measurements under air mass zero solar simulation was made before and after the environmental test.

B. Test Results

As a result of the inspection and evaluation of the sample panel after completion of the sixty thermal cycles, certain failure modes were observed. Most of these failure modes were strongly associated with certain configurations.

The most prevalent failure mechanism, which led to significant electrical degradation was one in which hairline fractures developed between the N-interconnector and the solder joint fillets, as shown in Figs. 8 and 9. This type of failure was typical of the C7-12 and the D1-12 group of Fig. 1. In some instances, the hairline fractures propagated through the entire connection, thus resulting in electrical degradation.

Other failure modes included delamination between the filter cover and the silicon cell accompanied by either extensive plastic deformation of the filter-to-silicon-cell adhesive, Fig. 10, or by extensive cratering of the silicon cell itself, Fig. 11. The delamination failures are characteristic of configurations in which the dimethyl silicone (RTV-602) is used as an adhesive between the filter and the silicon cell. All modules 7 to 12 of Fig. 1 employ this adhesive. It is of interest to note here that the A7-12 group represent the basic Mariner 1969/1971 design, which had passed the relatively milder environmental requirements for these missions. In a few isolated instances failures of the types mentioned were observed on a much smaller scale in other configurations.

The nature of the failures shown in Figs. 8 through 11 emphasize the need for design improvements to isolate and correct the observed failure mechanisms. Otherwise, as the environmental requirements become more and more severe it will become increasingly difficult to assess solar array damage during its space mission. Concept C, which is the proposed configuration for VO'75 mission is the result of such design improvements. By employing the analysis of Section III, an improved design was obtained in which no failures were observed during subsequent environmental testing.

III. ANALYSIS PROCEDURE

A. Solar Cell Loading and Environment

Under operating conditions solar cell arrays can be subjected to a variety of loading conditions, the sources of which may be classified as either mechanical or thermal. Some loading conditions are more severe than others. Mechanical loads arise from static distortion of the substrate, or from dynamic excitations induced at a wide range of frequencies. In arrays with relatively rigid substrates (such as aluminum corrugation for the Mariner 1969/1971 or sandwich honeycomb construction for the VO'75 design) thermally induced loads on the solar cells typically overshadow the mechanically induced loads. This may not be necessarily true for arrays with more flexible substrates. Because the aim of this report is directed toward designs compatible with the VO'75 solar arrays (rigid substrate), emphasis is placed here on the thermally induced environments.

The most severe of the thermally induced loads in solar cells are cyclic in nature. The total temperature change from the high to the low end of the thermal cycle, as well as the total number of cycles, are important factors in causing thermal fatigue and subsequent failure in components of solar cells. A complete analysis of thermal fatigue problems is both complex and impractical, indeed. It must account for several complicated phenomena which manifest themselves on both the microscopic and macroscopic levels of the material behavior. For example, temperature changes and their time rate of change can result, among other things, in phase transformations, aging, recrystallization, and grain growth in metals. In turn, these phenomena can considerably affect the macroscopic behavior of the materials and result in continuous changes in the stress-strain relationships, the yield limit, and subsequent plastic flow characteristics, crack propagation, and damage accumulation from one thermal cycle to the next. All of these factors are known to govern the thermal fatigue life in different ways, which nevertheless, are least understood even for the common structural materials.

Because of the complexities cited above, thermal fatigue life predictions are usually based on empirical formulas, which to date have not been substantiated. However, it is a well-known fact that the lower the thermally induced stresses during one cycle, the longer the fatigue life one may expect. This simple rule is utilized here as a basis for comparing the performance of candidate solar cell designs. And although the present approach does not attempt to predict the fatigue life to failure, it seeks to give reliable stress distribution in a given solar cell design during a typical thermal cycle. For this purpose, the experimentally measured material properties of Section IV are used in the analysis for comparison between designs.

In conjunction with this approach, the final selected design will still need to be qualified by tests, as described in Section II, to insure its ability to survive more than the required number of thermal cycles. Such tests are necessary, whether or not a prediction of fatigue life exists.

B. Computational Scheme in the Analysis

The finite element technique, in conjunction with the general-purpose computer program VISCEL[1] were used in this study to obtain the stresses in the components of the solar cells as a function of temperature. The program is documented in Refs. 3 and 4 and can be obtained from the Computer Software Management and Information Center (COSMIC), the NASA agency for the distribution of computer programs.

The present thermoelastic analysis using VISCEL incorporates important improvements over the previously described analysis of the computer program ELAS (Ref. 1). In ELAS, the thermal deformation and stresses in the model can be obtained for only one temperature increment (or decrement), during which no changes in material properties are allowed. For large temperature changes as shown in Fig. 6, most solar cell materials are strongly temperature dependent. As Section IV shows, some materials, such as the adhesives, change properties by several orders of magnitude as they approach their glass transition temperatures. VISCEL is well suited for such cases. Deformations and stresses in a given model can be obtained on a cumulative basis from one thermal (or time) step to the next. During each step the material properties can be different from those in the previous steps. In this manner the temperature dependence of material properties is accounted for during the thermal cycle.

Starting from time zero, the computational scheme in VISCEL assumes that the material properties (modulus of elasticity E, shear modulus G, coefficient of thermal expansion α), as well as the set of external disturbances (applied loads or temperature changes T) are expressed as functions of a single parameter ξ. This parameter may be time, reduced time, or any other suitable variable. All the functional relationships between the quantities mentioned must be synchronized with respect to the variable ξ. That is, any dependence or interaction between the quantities is either ignored, or must be included in a predetermined tabulated values of these quantities as a function of the independent variable ξ. One must therefore input the tabulated values for every increment or step of ξ. These increments may or may not be equal.

---

[1] The acronym VISCEL stands for VISCoELastic analysis.

The effect of the time rate of change of temperature on the properties of materials of solar cell arrays is a subject in itself, which requires extensive and costly testing techniques. For thermal environments of the type shown in Fig. 6, temperature changes occur relatively slowly during the largest part of one thermal cycle so that thermal equilibrium is essentially achieved. With this assumption, only the effect of temperature on material properties when thermal equilibrium was reached was evaluated in Section IV, and the thermoelastic rather than the viscoelastic properties were obtained. For consistency, the analysis accounts for the thermoelastic properties without regard to the time rate of change of temperature. As such, the independent variable ξ was taken as the temperature change, and the tabulated input property data were functions of the temperature increments. The temperature increments used in the analysis ranged from ±25 to ±50°C. A series of such temperature increments was used to simulate a thermal cycle for a given solar cell design. At the end of each increment, the accumulated deformations and stresses at every node of a given model were output by the program.

C. Structural Modeling and Input Data

The modeling procedure utilizes the finite element concept, where the actual cell composite is subdivided into several finite elements connected together at node points. The choice of the type of elements as one-, two-, or three-dimensional elements to represent the various components of a given design as closely as possible is determined by the analyst. Each solar cell design requires the construction of a different model, since each design is geometrically different. However, the different designs considered in this report share similar features that provide some common modeling considerations. For example, all designs consist of a number of individual solar cells connected together in parallel and series to constitute a module of the array. The basic difference between the various designs is in the P-interconnector and the N-interconnector geometries. Some variations in the material of some components and thicknesses of some layers also exist. For accurate computation of the stress distributions in a given configuration, as many elements and nodes as possible should be included in the model. However, limitations on the number of elements and nodes which may be included in the model are imposed by the computer memory storage capacity and the computational time required. Thus, in order to maintain computational accuracy the following considerations were taken for all designs wherever possible:

(1) Partitioning of a solar cell into separate smaller segments.

(2) Utilizing symmetry boundary conditions along lines where geometry dictated complete or near complete symmetry.

To illustrate, consider the basic Mariner 1969/1971 design in Figs. 2 and 12a. Each cell was considered as a separate unit (with the proper boundary conditions), since the stresses are similarly distributed within each cell. Furthermore, in order to account for as many features in the model as possible and still not exceed the computer storage limit of about 130,000 decimal words[2] (twice the usual 65,000), a typical cell and its interconnectors were partitioned into two segments, as shown in Fig. 12(b) and (c). Each of these segments was modeled separately, and symmetry boundary conditions were applied along edges BC, and DC for segment (1), as in Fig. 12(c), and along edges EH, HG, IK, and at J for segment (2), as in Fig. 12(b). Complete symmetry along DC, EH, J, and the near side of IK, is guaranteed by the geometry of the assembled cells. Although symmetry along BC and GH is only partial, it is strong enough so that complete symmetry may be assumed there without producing appreciable errors in the results. In this manner, the two models for segments (1) and (2) together give the stress distributions in the most stressed areas of a typical cell.

As Fig. 2 shows, the cell is composed of several components. The fused silica filter is bonded on the P-type silicon wafer by a layer of transparent silicone rubber adhesive. The bottom side of the silicon wafer may be either solder coated or solderless. The wafer with the P-interconnector attached to its bottom side at some local areas is then bonded to the dielectric and aluminum honeycomb substrate by another layer of opaque silicone rubber adhesive. The N-interconnector is soldered to a portion of the top edge of the cell on a thin layer of silver/titanium.

---

[2] Limitations in the current Univac 1108 system at JPL.

Models for segments (1) and (2) in Fig. 12 complement each other in that the model for segment (1) emphasizes stress computations in the cell interior, including the P-interconnector, while the model for segment (2) emphasizes stress computations along the edge in the neighborhood of the N-interconnector, including the bent portion of the P-interconnector. In modeling both segments, three-dimensional solid tetrahedron and hexahedron finite elements were used to represent the geometry of the several layers and components just mentioned.

Appendix A contains a schematic of the model used for a modified Mariner 1969/1971 configuration and a listing of the inputs used for the VISCEL computer program. In this example, temperature changes from 0 to -185°C were imposed as the external disturbances. This was achieved in six successive temperature increments of -25°C, and one last increment of -35°C.

The inputs for VISCEL (Appendix A), its contents and formats are essentially those of ELAS with some modifications. Reference 3 should be consulted for detailed explanation. In summary, the input data can be classified in two groups. The first group contains data which are not allowed to change from one solution step to the next. They include geometrical description of the model under consideration (node point coordinates in an overall X, Y, Z system and definition of each finite element in the model and the nodes to which each element connects), as well as any externally applied forces and displacement boundary conditions. The second group contains data which may vary from one solution step to the next. The thermal increments or decrements along with their synchronized material properties (averaged over the increment) are typical of this second group of data.

Several models corresponding to several geometrical configurations and candidate materials were constructed and analyzed by the procedure just mentioned. These models correspond to cell designs included in the experimental sample panel tests described in Section II. The material properties used throughout the analysis are discussed in the following section.

IV. MATERIAL PROPERTIES

Certain thermal and mechanical material properties of the solar array components must be accurately known before a valid stress analysis may be performed. As previously mentioned, the specific material properties needed for calculating the stresses resulting from thermal cycling are the coefficients of thermal expansion, the elastic moduli, the Poisson's ratios and the stress-strain characteristics. Since most of the candidate materials of the solar cell/interconnector construction are non-structural, very little information was found in the literature on these properties, especially at the subzero temperatures.

To obtain needed data, tests were conducted at temperatures from -186 to +200°C on solid cylindrical rods for the solar cell silicon, rolled-sheet stock for the interconnector metals, and cast sheet and rods for the RTV-type silicone rubber adhesives.

A. Silicon Solar Cell and Fused Silica Filter Materials

The vast majority of information in the literature on silicon and fused silica is for physical, electrical, and optical properties. There is very little on mechanical properties; when available, the specimens and the procedures used were found, in most cases, to be incompatible with the requirements of this program. The coefficient of linear thermal expansion for silicon had been measured during earlier work (Ref. 1) and was obtained for the Code 7940 fused silica from Corning Glass Works (Ref. 5).

1. Coefficient of Linear Thermal Expansion

In preparing the specimens for the thermal expansion tests, several material processing variables were taken into consideration. These variables included: the effects of growing junctions in the material by diffusion of impurity elements, the effects of the crystal lattice growth orientation with respect to specimen configuration and the effects of relative amounts of impurity element doping on a parts-per-million basis of the base silicon. The specimens consisted of P-type single-crystal material oriented with the long dimension (the one measured) parallel to the [100] crystal growth direction, and N-type single-crystal material oriented with the long dimension parallel to the [111] crystal growth direction. On some of the specimens, junctions were made by thermally diffusing impurity elements into the silicon. The junction depths were of the same magnitude as used in normal solar cell fabrication. Other specimens remained undiffused, while a third group was hyperdiffused with lithium. The electrical resistivity of the bulk silicon, which is a function of the initial impurity element content, was also varied among the specimens. The samples tested are listed in Table 1. The results obtained and reported in Ref. 1 indicated that the coefficient of linear thermal expansion was not significantly affected by any of the listed processing variables or by crystal growth orientation. The data were compiled and an average was determined for all the specimens. Figure 13 shows the coefficient of expansion versus temperature curve of the solar cell grade silicon and that of the Code 7940 fused-silica filter glass material.

2. Elastic Modulus, Poisson's Ratio and Ultimate Strength

The only known data on the mechanical strength properties of solar cell grade silicon were from room-temperature flexural tests (Ref. 1) which did not provide the required information for the analysis program. Conventional-type tension and compression specimens were needed that could be monitored during loading to obtain stress-strain data for elastic modulus and Poisson's ratio determinations. To provide these specimens, cylindrical rods of P- and N-type single-crystal material were grown to rough dimensions by Centralab, a division of Globe Union, Inc. The other solar cell silicon supplier, Heliotek, a division of Textron, Inc., fabricated rods that had been core drilled from larger diameter crystals. The crystal growth orientation of the silicon rods was maintained in the same preferred directions that were employed on the thermal expansion specimens. The N-type rods were oriented with their long axes parallel to the [111] direction and P-type rods with their long axes parallel to [100] direction. A total of thirty rods were procured from the two suppliers.

A test plan was developed whereby a maximum amount of information could be obtained from the limited number of silicon specimens. This plan involved the use of nondestructive evaluations for determining elastic modulus and Poisson's ratio at several temperatures. In this manner, numerous elastic modulus and Poisson's ratio determinations were made on specimens without their destruction. Ultimate strength tests were subsequently performed at the end of the test program. The test procedures are given in Appendix B.

There was some breakage of specimens during the nondestructive evaluations for elastic modulus and Poisson's ratio despite careful precautions, including the use of test fixtures with gas-bearings (designed especially to eliminate eccentricity in loading for testing of brittle materials). This caused a shortage of test specimens for later ultimate strength determinations. For this reason additional testing is now in progress on other specimens to provide more ultimate strength data on the silicon and also some limited data on the Code 7940 fused silica.

The results of the elastic modulus and Poisson's ratio tests of the single-crystal silicon at the various temperatures are shown in Figs. 14 through 17 as plots of elastic modulus and Poisson's ratio versus temperature. The stress-strain relationships for the silicon material were linear and therefore are not shown in this report. The elastic modulus values in compression (Fig. 15) are generally consistent with one exception: the average compressive modulus value for one N-type specimen was approximately 2.068×10^6 N/cm^2 (3×10^6 psi) lower than the remainder of this type of specimen. The overall average compressive modulus value for the N-type specimens was 18.34×10^6 N/cm^2 (26.6×10^6 psi) between -186 and 200°C. There was a very slight decrease in the compressive modulus with decrease in temperature for both the N- and P-types of silicon. This trend was just the opposite for the tensile modulus values, where there was a slight increase in the average value with temperature decrease. This is illustrated in Fig. 14.

The elastic modulus values measured in tension were not as consistent as those measured in compression, but were still confined to fairly narrow bands. The average value for the N-type silicon was again higher than that for the P-type with very little difference from the compressive values. The average values for the tensile modulus were approximately 18.62×10^6 N/cm^2 (27×10^6 psi) for the N-type and 12.82×10^6 N/cm^2 (18.6×10^6 psi) for the P-type silicon.

The Poisson's ratio values measured in compression for the N-type and P-type specimens are shown in Fig. 17. They are generally consistent at -50°C and above with an average value of approximately 0.28 for P-type, and 0.20 for N-type material. There was some scatter in the values for the N-type specimens. However, the Poisson's ratio values measured in tension (Fig. 16) were even more scattered. In the range from -185 to -100°C there is an apparent overlap in the data points between the P-type and N-type material. The noticeable scatter in all tensile data as compared with compressive data may be explained, in part, by: (1) the use of a single lateral strain gauge on tensile specimens, and (2) the much smaller radii of the tensile specimens (0.33-cm diam) on which the strain gauges were attached. The radii of the compressive specimens were 1.27 cm. There is no explanation, except possibly residual strain effects, for the inconsistent results at the various temperatures for a given specimen.

Included in each of the Figs. 14 through 17 is a linear regression analysis of the elastic modulus and Poisson's ratio variation with temperature. This regression was fitted using the method of least squares. Tests of significance of the regression coefficients indicate that slopes of all lines except for the N- and P- type moduli in tension and the Poisson's ratio in compression of the P-type silicon are likely to be different from zero. The slopes of the tensile and compressive moduli regressions are of opposite sign.

The elastic modulus and Poisson's ratio of the Code 7940 fused silica were obtained from the literature (Ref. 5) and are shown in Fig. 18.

Because of specimen breakage during tests for elastic modulus and Poisson's ratio, only limited data was obtained on the ultimate strength of the silicon. Ultimate tensile strength results were obtained for only seventeen specimens. These data, which are shown in Tables 2 and 3, were obtained for specimens that had been previously cycled to lower stress levels (below the precision elastic limit. See Appendix B). As expected for brittle glassy-type materials, the silicon is much stronger in compression than tension. One trend noted thus far in the ultimate strength testing of silicon is that the P-type material appears to be slightly stronger in both tension and compression than the N-type. This characteristic also occurred during earlier flexural tests (Ref. 1) on actual solar-cell wafer blanks.

The higher strengths achieved by the P-type specimens may be explained by their crystallographic orientation with respect to the loading direction. The P-type specimens were stressed with the weaker [110] crystal direction at an angle of 40 to 50 deg to the longitudinal (stressed) dimension. Failure occurred preferentially along this direction in the weak (111) planes resulting in inclined fractures. On the other hand, the N-type specimens were oriented with their longitudinal axes parallel to the stronger [111] growth direction. With this orientation, the weak (111) planes are perpendicular to the direction of loading, and fractures occur normal to the specimen centerlines. Failure for silicon almost always occurs along the weak (111) planes. In crystallography nomenclature, planes always lie at right angles to their corresponding growth axes. Since the surface areas of (111) planes are greater in stressed cross-sections of P-type specimens, their breaking loads are subsequently higher. The reader is referred to the literature (Ref. 6) for more detailed discussion of silicon structure, crystal habit and orientation. Other workers (Ref. 7) have noted silicon fracture behavior at similar temperature ranges on smaller size specimens. Below 600°C specimens grown with their long axes in the [111] direction showed only elastic deformation prior to failure. Fractures occurred by cleavage, starting at a point near the external surface and propagating across the specimen in steps, fanning out from the origin. Using interference fringing to study the fractures these investigators noted that fracture initiated on a plane normal to the specimen's axis then shifted to the (111) cleavage plane. In their samples the (111) planes were not exactly perpendicular to the specimen axes. Similar cleavage plane patterns were noted in the fractures of the silicon specimens tested during this program. More ultimate strength data for silicon is presently being obtained. This data and data for fused silica will be reported at a later time.

B. Silicone Rubber Adhesives

Experience has shown that for the extremely low temperatures expected on future interplanetary space flights that RTV-type silicone rubber adhesives are among the best materials for solar cell-to-substrate and filter glass-to-solar cell bonds. Two generic types of RTV silicone rubbers, the methyl-phenyls and the dimethyls, have found use in these bonding applications for photovoltaic devices. The methyl-phenyls have the superior low temperature properties, whereas the dimethyls have been more widely used in past space flights by JPL. In this test program seven candidate RTV silicone rubber adhesives were evaluated. These materials are listed in Table 4.

The RTV 41 and 602 are the adhesives which have been previously used for solar arrays by JPL, whereas the remaining materials are new candidates. The RTV 566 and DC 93-500 represent fairly recently introduced silicone rubbers. They have been specially processed to remove volatile condensable constituents that outgas during space flights. The XR 63-489 is a special grade of silicone which is manufactured for optimum optical transmission. It is chemically very similar to the DC 93-500, and both are derivatives of the basic Sylgard 184 silicone resin from the Dow Corning Corp.

1. Coefficient of Thermal Expansion

In previous work (Ref. 1) the coefficient of linear thermal expansion was determined for six of the above silicone materials. Figure 19 is a plot of the coefficient of expansion versus temperature for the six silicone rubbers that were tested. It is noted that the two dimethyl silicones have extremely high coefficient of expansion values in the vicinity of -40 to -50°C, which is indicative that the material has passed into the crystalline phase. In these tests, the specimens were soaked at the coldest temperatures and then gradually brought up in temperature. The measurements were made each 15 minutes as the specimen temperature was increased. There is some possibility of lag in the dimensional change associated with the increase in temperature, which may explain the apparent higher crystalline transition for the two dimethyl materials from that reported by the manufacturer. At the crystalline transition temperature the dimethyl materials become stiff; this state is also appropriately referred to as the stiffening temperature. To eliminate this effect in silicones, the manufacturers have replaced some of the methyl groups in the silicone polymer chain with more bulky phenyl groups, resulting in a superior low-temperature material known as methyl-phenyl silicone. These latter silicones have no apparent crystalline transition and remain amorphous until the glass transition temperature is reached. The glass transition temperature for both the methyl-phenyl and dimethyl silicones is approximately -125° C. Figure 20 illustrates these phenomena for the two types of silicone rubbers.

2. Elastic Modulus and Ultimate Strength

Tests were conducted on cured specimens of the RTV-type silicone rubber materials to determine elastic moduli and ultimate strengths in both tension and compression. The tension testing was performed on thin cured dumbell-shaped sheet specimens of the various materials using the Die C configuration of ASTM 412. The compression testing was performed on cast, 1.27-cm (0.5 in.) diam by 5.08-cm (2.0 in.) long specimens. Data was obtained at six temperatures ranging from -185 to +200° C. The test procedures are included in Appendix C. The results of these tests are included in Figs. 21 to 24. Figure 21 is a plot of the initial elastic modulus in tension for each of the rubbers versus temperature. These plots illustrate that the two dimethyl silicone types (RTV 41 and 602) have undergone crystalline transition at the -100°C test point, whereas the methyl-phenyl materials remain amorphous and rubbery at this test point. A similar observation is noted in the elastic modulus in compression versus temperature plots of Fig. 22. There are orders of magnitude increases in elastic modulus when the materials have passed into the brittle glassy phase. The elastic modulus in the crystalline and glass transition regions are of interest with respect to the accompanying changes in thermal expansion coefficient. Since only limited data in these regions were obtained in the first set, more tests are currently under way to define more precisely the shape of the curves. From preliminary indications, it appears that rapid increases in the expansion coefficient with very little temperature change in conjunction with huge increases in the elastic modulus might account for the failures noted on certain solar cell-coverglass adhesive combinations.

Figures 23 and 24 are plots of ultimate tensile strength versus temperature and compressive strength versus temperature for the silicone rubber adhesives tested. Similar observations to what were noted in the elastic modulus plots can be made between the dimethyl and methyl-phenyl silicone materials. The clear RTV 602 (dimethyl silicone) is very weak in its normal amorphous state; however, it becomes appreciably stronger in the crystalline state. The methyl-phenyl materials exhibit a more gradual increase in strength with decreasing temperature, as noted in Figs. 23 and 24. In addition to the data for elastic modulus and ultimate strength versus temperature, stress-strain curves were also obtained. Typical stress-strain curves for each material at the various test temperatures are shown as Figs. 25 through 31. The shapes of these curves vary considerably but do maintain a certain degree of similarity between materials of the same family, e.g., XR 63-489 and DC 93-500. Apparently the chemical structure of the polymer chains composing these materials, in addition to any fillers that may be present, exert an influence on the stress-strain behavior of these materials. The silicone rubbers filled with similar materials had similar shaped curves in several instances, e.g., iron oxide in RTV 560 and 566 and the titanium dioxide in RTV 41 and 511/577.

3. Poisson's Ratio

The measurement of Poisson's ratio for the RTV-type silicones was not as easily determined as the elastic modulus and ultimate strength values. No standard test method has been developed to date. The application of strain gauges to these materials was not practical over the wide temperature range of interest because of difficulties in effecting and maintaining good bonds. A photographic method was developed specifically for these materials for recording the strains on the specimens as the stresses are applied. The apparatus, experimental setup, and procedures employed are included in Appendix C.

The compressive mode of loading the specimens was selected in order to simplify the method of gripping. Right cylindrical specimens were used. A camera was placed outside an environmental test chamber in a position in such a way that the specimens could be photographed through a window. Photographs were then taken of the specimens at various loads, and the resulting deformations were recorded on film. Calculations were then made and plots were obtained of radial strain versus stress and axial strain versus stress from which Poisson's ratio was determined.

The results are shown in Fig. 32 for each of the seven candidate RTV-type silicone rubber materials. All materials appeared to have reasonable results, with the exception of RTV 602, which exhibits a fairly erratic response. For the RTV 602, the earlier decrease in Poisson's ratio with decrease in temperature is explained by the fact that the material enters into a semicrystalline state at a higher temperature than usually expected for the methyl-phenyl types of silicones. Crystalline materials generally have low Poisson's ratio values. However, the reason for the apparent decrease from the room-temperature value with a temperature increase was not determined. These inconsistencies for the RTV 602 did not occur in the tests for elastic modulus and ultimate strength.

Poisson's ratio of all the RTV materials generally does not deviate very much as a function of temperature above the glass transition temperature of the materials (-125°C). However, the dimethyls (RTV 41 and 602) begin to change in their physical appearance when they reach their crystalline transition temperature (-57°C). Thus, an earlier decrease in the value of Poisson's ratio would be expected for these two materials. RTV 560 (a methyl-phenyl silicone) exhibits a definite and sizeable decrease in its Poisson's ratio value at approximately -70°C, which is unexpected. One possible explanation for this earlier indication of brittleness is the "super cooling" effect (Ref. 9) noted in silicone materials. This effect occurs when a polymer is cooled so rapidly through its stiffening temperature that the molecules do not have time to align themselves into the normal freezing pattern. Instead, they are believed to form a pattern typically found at the glass transition temperature. When the specimen is warmed slightly, it will first begin to soften and then harden again as the temperature rises to approach the stiffening temperature. This effect is more commonly found in the dimethyl silicones, since the methyl-phenyls generally show no apparent crystalline transition. A second and perhaps more plausible explanation might be that the material, having had a previous lower temperature, had insufficient time to stabilize at the -100°C temperature before the measurement.

Below the glass transition temperature, Poisson's ratio decreases signficantly. In fact, the values of 0.1 to 0.2 appear almost too low in comparison to other glassy materials. However, these low values were obtained consistently for all the samples.

C. Interconnector Metals and Solder Materials

In addition to the property measurements made on the silicon and the various silicone rubber adhesives, the properties of several candidate interconnector metals were also determined. These metals included: Kovar, molybdenum, palladium, silver, and a lead-tin solder alloy containing a small percentage of silver. Data were obtained from the literature on the coefficient of expansion for Kovar, molybdenum, aluminum, and palladium. Measurements were made specifically for this test program on the solder and the silver and previously described techniques were employed (Ref. 1). Mechanical property tests in tension for the elastic modulus, ultimate strength and Poisson's ratio were also performed.

1. Coefficient of Thermal Expansion

The coefficients of linear thermal expansion were more readily available from the literature for this group of materials than for the silicone rubbers or the silicon. Figure 13 includes data on the expansion coefficients versus temperature for the six materials in this group. With the exception of the solder and the silver, these values were obtained from the literature. The coefficients of expansion for the silver and the solder alloy were measured for this program. Figure 13 shows that the solder, aluminum, and silver have somewhat similar thermal coefficient values (approximately 15 to 20 $\times 10^{-6}$ cm/cm/° C). Kovar and molybdenum have fairly low values, as do the silicon and fused silica. The latter values are of the order of -4 to 7 $\times 10^{-6}$ cm/cm/° C.

2. Elastic Modulus, Ultimate Strength, and Poisson's Ratio

Values of ultimate strength, elastic modulus in tension, and Poisson's ratio were measured for the five materials shown in Table 5.

The flat sheet specimen configuration with the test equipment and procedures employed are shown in Appendix D. Tests were conducted at -196, -100, -25° C, room temperature (25° C), 100 and 200° C. The load-strain curves for a representative specimen of each material at each of the six test temperatures are presented in Figs. 33 through 37. Figures 38 through 42 show the elastic modulus, ultimate strength, and Poisson's ratio versus temperature for each of the various metals. In all cases, except for palladium (Fig. 40), the ultimate strength decreases with an increase in test temperature. This was also true for the 0.2% offset-yield strength and the proportional limit values shown in Appendix D. At 200° C, the palladium shows a slight increase in ultimate tensile strength over that measured at 100° C. The elastic modulus and Poisson's ratio values for Kovar, molybdenum, and palladium reach their maximum at the lower temperatures (-100 and 196° C). However, the silver and the solder show maximum values at the higher temperatures. The elastic modulus values for molybdenum, silver, and solder show a decrease with increasing test temperature, but the Kovar and palladium attain their highest level at 200° C. The ultimate strength of a material generally decreases with an increase in test temperature, but this is not always true. The measured increase in the tensile strength of palladium at 200° C over that at 100° C has also been noted by other investigators (Ref. 10).

All fractured ultimate strength specimens were given a cursory visual examination upon completion of test, but at least one specimen from each material at each temperature was examined carefully. The results of this examination are recorded in Table 6. The tension-type ductile fractures resulted in wedge-shaped fracture surfaces, whereas the shear-type ductile fractures exhibited rupture faces approximately 45 deg to the flat surface of the specimen. The brittle-type fractures noted on the molybdenum at -196°C was accompanied by some elongation. At test temperatures of 100 and 150°C, the solder specimens were extremely ductile, with deformation of 177 and 285% after rupture.

The elastic modulus usually is very little affected by moderate temperature increases, especially for molybdenum (Fig. 39). As test temperatures approach the melting point of a material, the elastic modulus value decreases as shown in the case of the solder alloy (Fig. 42). In the case of Kovar (Fig. 38) where the elastic modulus appears to fluctuate in the area of -80°C, a phase transformation could be in progress. When this phenomenon occurs in Kovar, there is a change in its crystalline structure. The transformation can be partial or complete and is accompanied by an increase in thermal expansion and possibly a change in the mechanical properties. The critical temperature for standard Kovar is below -78°C. However, by varying the amount of alloy additions, this temperature can be suppressed to a value below -269°C. Special heats can be ordered from the manufacturer with the lower transformation temperatures specified. The material tested was supposedly from a heat exhibiting the lower transformation temperature, but from these results it appears that there may have been a partial transformation. Other factors can also affect the elastic modulus. Chevenard and Crussard (Ref. 11) found that an alloy containing almost equal parts of iron and nickel will vary in its elastic modulus value by as much as 13% depending on the amount of cold work. A material can become cold worked during test, resulting in different properties. The effectiveness of the cold work will depend on the test temperature, since annealing can occur concurrently. Koster and Scherb (Ref. 12) have seen this effect in silver.

Poisson's ratio is generally believed to be a constant, but only over a limited temperature span near ambient temperatures. There is only a limited amount of information on this value at subzero temperatures. The general trend of Poisson's ratio is to increase gradually up to 0.5 near the melting point of the material.

Starting at ambient conditions, four of the five metals investigated in this part of the program showed an increase in Poisson's ratio with increasing temperature. An increase in Poisson's ratio is also reported with decreasing temperature for all materials except solder.

Poisson's ratio values obtained at 100 and 150°C on solder (Fig. 42) are believed to be subject to more error than the other values. These temperatures are approaching the melting temperature of the solder. Loads on the specimens were very small so that normal experimental variations could become significant on a percentage basis. In addition, there could be an effect of the strain gauge backing material, cement, and coating. When loads are very small, the effect of these extraneous factors may be significant.

It is generally assumed that Poisson's ratios should not exceed 0.5. Values in excess of 0.5 have been obtained by other investigators (Ref. 11). Such values are unusual and are believed to be related to the anisotropy of a material.

V. RESULTS OF ANALYSIS

The nature of failure and its location in the components of a solar cell depend upon a variety of factors. Failures that occur in the cell interior away from the N-interconnector (Figs. 10 and 11), depend upon the thicknesses and material characteristics of the filter cover, the adhesives on both sides of the silicon wafer, the silicon wafer itself, whether the silicon wafer is solder coated or solderless, and on the P-interconnector geometry and material. Such failures are investigated in the analysis by examining the stresses computed in the models of segment (1) in Fig. 12. On the other hand, failures in the neighborhood of the N-interconnector of the type shown in Fig. 8 depend primarily upon the material and geometry of the N-interconnector as well as upon the solder joint and silicon wafer geometry and material properties. These types of failures are obtained from the analysis of segment (2) type models. Results of analyses made on each of the two segments are discussed next.

A. Stresses in Cell Interior and P-Interconnector

Referring to the various configurations of the layout (Fig. 1) several models were constructed for type (1) segments. Each model corresponds to one of the configurations in Fig. 1. For example, model A1-6 corresponds to modules number 1 through 6 of column A, model A7-12 corresponds to modules number 7 through 12 of column A, etc. Other configuration considered are A13-14, A15-16, B1-6, B13-14, C1-6, C13-14, and concepts A and C, a total of ten configurations. The nominal thickness of the different layers were used in the models to compute the stress distribution within each of the filter, filter-to-cell adhesive, cell wafer, solder coating (if any), P-interconnector, and cell-to-substrate adhesive layers.

The results obtained for each model consist of six components of stresses (three normal stresses σ_{ix}, σ_{iy}, σ_{iz}, and three shear stresses τ_{ixy}, τ_{ixz}, τ_{iyz}) at each node within each layer of the model, for each increment of temperature. However, because a stress component at a given node is not by itself meaningful in terms of determining the relative merit of two given configurations, the six stress components were combined at each node i to give an effective stress quantity[3] $(\sigma_{eff})_i$, so that:

$$(\sigma_{eff})_i = \left[I_{i1}^2 - 3\, I_{i2}\right]^{1/2} \tag{1}$$

where

I_{i1} = the first invariant of the stress tensor at node i

$= \sigma_{ix} + \sigma_{iy} + \sigma_{iz}$

I_{i2} = the second invariant of the stress tensor at node i

$= \sigma_{ix}\sigma_{iy} + \sigma_{iy}\sigma_{iz} + \sigma_{iz}\sigma_{ix} - \tau_{ixy}^2 - \tau_{iyz}^2 - \tau_{ixz}^2$

In this manner, an equivalent effective stress $(\sigma_{eff})_i$ was computed for every node in a given model, for each increment of temperature. As was done in Ref. 1, an estimate of how close the computed stresses are to the failure limit can be obtained by comparing the maximum computed effective stress at all nodes in a given material in the model to the effective stress (σ_{eff}^*) measured in a uniaxial test specimen at the temperature in question. Under a uniaxial loading condition (see data on ultimate strength σ^* in Sec. IV), only $\sigma_x = \sigma^*$ exists, while $\sigma_y = \sigma_z = \tau_{xy} = \tau_{yz} = \tau_{xz} = 0$. According to Eq. (1), $(\sigma_{eff}^*) = \sigma^*$. Thus, an estimate of failure in a given material of the solar cell components is obtained by examining the ratio max $(\sigma_{eff})_i/\sigma^*$ for the temperature in question. When this ratio approaches unity for a given material in the model at a given temperature, this indicates that the solar cell component is stress critical. When this ratio is greater than unity, it is interpreted as indicating that the component in question has already reached failure at a prior temperature level. For thermal cycling, an acceptable design should have maximum effective stress ratio smaller than unity for all of its components at all temperatures between the extremes of a single cycle. In this sense, the smaller the

---

[3] Additional discussion of this quantity can be found in Ref. 1.

maximum effective stress ratio the better the design, in that it can survive a greater number of cycles.

A summary of the results in the form of effective stress ratios for the ten configurations previously mentioned is given in Table 7. Each of the ten designs were subjected to thermal changes from 0 to -185°C. Variations in the material properties with temperature are already reflected in these ratios. When a material such as the silicon exhibited different σ_c^* in compression from that in tension σ_t^*, an average value was used to compute the effective stress ratio. Similarly, when a material property, such as the elastic modulus E, exhibited different values for tension and compression, an average of these was used in the analysis.

On the basis of Table 7, the following conclusion can be made:

(1) The effective stress ratio is highest at the low end of the temperature cycle (-185°C). This is clear from the values obtained for each of the layers (columns 1 through 6 of Table 7) at -50, -100, and -185°C for configurations A1-6 and A7-12. To insure that the sudden changes in adhesive properties during phase changes are accounted for, the analysis of A1-6 and A7-12 were repeated with smaller temperature increments of -25°C. The results showed about 10% increase in the stress ratios for A7-12 between -50 and -100°C. However, these ratios still reached their highest values at -185°C, thus indicating that failures in the cell interior is most likely at the low end of the temperature cycle.

(2) The only difference between A1-6 and A15-16 is that the silicon wafer is solder coated in A1-6 but it is solderless in A15-16. The results shown by Table 7 indicate definite better performance when solder coating is used. Solder coating seems to act as a buffer on the silicon, P-interconnector as well as on both adhesives.

(3) Two adhesive groups were primarily used in the experimental sample panel program and in the analysis. In one group, RTV 602 and RTV 41 were used as a filter adhesive and cell-to-substrate adhesive, respectively. In the other group,

XR63-489 and RTV-560 were used as a filter adhesive and cell-to-substrate adhesive, respectively. The first group (RTV-602/41) was used, for example, in A7-12 and A13-15, whereas the second group (XR63-489/RTV-560) was used in A1-6 and A15-16 configurations. By comparing the results of these designs, the XR63-489/RTV-560 group is definitely superior over the (RTV-602/41). The superiority of the XR63-489/RTV-560 is more obvious when used with the solder-coated designs.

(4) A comparison between the suitability of Kovar versus palladium for the P-interconnector in the basic Mariner design can be made from the A1-6 versus C1-6 configuration and the A13-14 versus C13-14 configurations. In both cases, results reveal that Kovar is a much more compatible material for the P-interconnector. As is shown in a latter section, Kovar is also a better material for the N-interconnector. The silver-mesh type as an interconnector was also investigated. Since silver-mesh interconnectors are basically different in geometry from the basic Mariner interconnector, a direct comparison that accounts for material properties only is not straight forward.

(5) The effect of different geometries for the P-interconnector may be evaluated by examining the results of the A1-6, the silver mesh concept (B1-6, B13-14), concepts A and C. Among these configurations, concept A exhibited low effective stress ratios for all of its components except for the cell-to-substrate adhesive. Its disadvantage, however, is that the P-interconnector is much heavier than its counterpart in other designs. In terms of overall performance, concepts A (when solder coated) and concept C seem to be the best choice. Also, configuration A1-6 is expected to perform satisfactorily.

Although Table 7 presents the results of the analyses in a very condensed form for the purpose of comparing the different configurations, other forms of presenting the results are possible. Figure (43a) through (43g) is used here as an example in which the contour lines of the effective stresses within each layer are plotted for the Al-6 configuration at -185°C. Such a presentation has the advantage of depicting the effective stress distribution throughout each layer.

B. Stresses in the N-interconnector and P-bend area

Stresses and failures in the N-interconnector, Fig. 8, the bend portion of the P-interconnector, the solder joint between the N-interconnector and the silicon wafer, as well as in a narrow strip of the silicon wafer are investigated in models of the type (2) segment in Fig. 12(b). In these models, the geometry of the interior portion of the P-interconnector is immaterial. It is not included in the type (2) segment, since its effect on the stress distribution in the neighborhood of the N-interconnector is negligible. For this reason, it was necessary to construct different models for the type (2) segments only when geometries of components in the neighborhood of the N-interconnector changed.

Five main configurations were analyzed. Their respective geometries and materials are shown in Fig. 44. The main difference between configura-ations [1] and [2] is that the material of the N-interconnector and P-bend is tin-plated Kovar for [1], while it is pure palladium for [2]. Configuration [2] is the same as configuration [3] except for the cell-to-substrate adhesive. Although it has the same thickness 0.01016 cm (0.004 in.) in both, RTV-560 was used for [2] as well as for [1, 4, 5], whereas RTV-41 was used for [3]. Modifications in thickness and geometry of the interconnectors are reflected in [4] and [5].

Results of the analysis of the five configuration are given in Table 8 as effective stress ratios (as previously discussed in connection with Table 7). The most stressed areas in the five cases are noted in Fig. 45 by the labels A_1 through A_{10} and B_0 through B_{10}. Table 8 makes reference to these labels to indicate the locations associated with the given stress ratios.

The following may be concluded from Table 8;

(1) Palladium as a material for the N- or P-interconnectors is inferior to Kovar. This is evident from the comparison of configuration [1] with configurations [2] and [3]. Kovar was

used in [1], whereas palladium was used in [2] and [3]. Although the solder joint, silicon wafer, and substrate adhesives in the neighborhood of the N-interconnector are hardly affected by whether Kovar or palladium is used ([1] versus [2]), configuration [3] indicates that unfavorable results can be expected when palladium is used for the interconnector along with RTV-41 for cell-to-substrate adhesive. This was found to be the case also in C1-6 of Table 7.

(2) Configuration [4], which was used in concept C, represents geometric modifications in the N-interconnector and the P-bend where curvatures are uniformly maintained. This uniformity in curvature reduces the effective stresses in the interconnectors, but results in a small contact area with the silicon. Because the load transfers from the N-interconnectors to the silicon wafer through the contact area, which is smaller in configuration [4], higher stresses are obtained in the solder and silicon in this configuration. Configuration [4], therefore, tends to reduce stresses in the interconnectors which are already low enough in [1], at the expense of increasing stresses in the solder and silicon (which are relatively high in [1]). For this reason configuration [1] is preferred to configuration [4].

(3) Configuration [1] can be improved by reducing the effective stresses in the solder joint and the silicon wafer. Reducing the N-interconnector thickness from 0.0254 cm (0.010 in.) to 0.0152 cm (0.006 in.), and modifying the P-interconnector bend to assume the more uniform curvature results in configuration [5]. This latter configuration, although it has not been tested, seems to have the advantage of reducing the stresses in the critical areas of the solder and silicon while still maintaining relatively low stresses in the interconnectors.

From the above, it is concluded that configuration [5] has the best chance of surviving the largest number of thermal cycles among the configurations considered. Other means of reducing the effective stresses in the junction under consideration were attempted. For example, the effect of reducing or increasing the height of the N-interconnector above the cell was investigated. The results did not show significant advantages in reducing the maximum effective stresses uniformly throughout the junction.

In summary, the analyses show that under the present thermal loading defined in Fig. 6, among the different designs reviewed in this report the optimum one combines the solder-coated version of concept C, or Al-6 with configuration [5] for the Kovar N- and P-interconnectors. The compatible adhesives for this design are the XR63-489 for the fused silica filter to the P-type silicon wafer adhesive, and the RTV-560 for the silicon-to-substrate adhesive.

VI. SUMMARY AND CONCLUSIONS

Throughout this report and in previous efforts (Refs. 1, 2), it was emphasized that knowledge of the thermal and mechanical properties of the components of solar cell arrays is essential for correct stress analysis and failure prediction. In this program the characterization of material properties was completed for the majority of the materials of interest. In the course of determining these properties special techniques were employed. They include special testing procedures for the silicon and fused silica materials using "gas bearings" to assure precise specimen alignment during mechanical loading and the photographic method developed for measuring Poisson's ratio of the RTV rubber adhesive.

The thermal and mechanical properties of the interconnector metals were consistent in terms of uniformity of the results and their variation with temperature. However, two exceptions were observed: (1) the decrease in the elastic modulus with the decrease in temperature for Kovar, which is contrary to expectations, and (2) the Poisson's ratio values for solder in excess of 0.5 above room temperature which is contrary to accepted theory.

For the RTV silicone rubber materials, wide variations were observed for their properties, especially at and below their transition temperatures. Several orders of magnitude changes in the elastic moduli (E), the ultimate strengths (σ^*), and the coefficients of thermal expansion (α), were found as a result of the silicone materials transition into brittle phases. Because of their more gradual and lower temperature transition, the phenyl-methyl type of RTV adhesive is considered superior to the dimethyl type for solar array applications. The effects of this relatively lower gradual transition of the phenyl-methyl adhesives was noted on all of their properties. In this sense their behavior is more compatible with the behavior of other materials in the solar cell composite (silicon, filter glass, solder, and interconnector metals) than the behavior of the dimethyl types.

Property determination of the silicon material comprised an important part of this program. Some of the important findings pertain to the fact that the P-type silicon mechanical properties were somewhat different from those of the N-type silicon. However, the coefficients of thermal expansion were basically identical. It was also found that the silicon materials, both P- and N-types, are very sensitive to methods of surface preparation. Wafers prepared by grinding must be stress relieved by chemical etching and polishing to assure optimum strength. The present tests on the ultimate strength of silicon materials, although limited in their statistical value because of sample breakage, indicated that, like other porous ceramic materials, silicon's strength in compression is several times higher than in tension. This fact, as well as other factors already discussed in connection with the behavior of the RTV silicone rubber adhesives, indicate that other failure criteria besides the effective stress criterion may be more suitable for the silicon and the silicone rubber adhesives.

The suitability of various failure criteria for the different materials considered is currently under further study. Nevertheless, the conclusions reached by the analysis in conjunction with the effective stress criterion were confirmed in stronger or lesser terms by the test program. As may be expected, there were also cases where the test program did not reveal the same conclusions obtained by analysis. These latter cases are relatively few.

Failures in the cell interior, where filter cracking and delamination was accompanied by silicon cell cratering (Fig. 11) was predicted by the analysis to occur at the low end of the temperature cycle, and was also observed during testing. Both analysis (Section V-A,) and test results strongly show that the XR63-489/RTV-560 adhesive group is much superior to the RTV-602/RTV-511 or the RTV-602/RTV-41 adhesive groups. Test results show less than 0.5% of this type of failure in all designs (with the

XR63-489/RTV-560) combined. In designs which employ the RTV 602 for filter adhesive, the percentage of filter cracking and silicon cratering failures were found to have drastically increased to 37% in the basic Mariner 1969/1971 design (A7-12), 40% in the silver mesh design (B7-12), 42% in the Mariner 1969/1971 design with palladium interconnects, and to 25% in the E. O. S. design (D7-12). All of these have solder-coated cells. Whether solder coating on the back of the cells lessened (as shown by analysis) or aggravate this type of failure was not obvious from test results.

On the other hand, failures exhibited in Fig. 10, where filter delaminations were accompanied by excessive deformation and curling of the filter adhesive, seem to occur during the temperature rise period of the thermal cycle. The cause could very well be unclean surfaces, which prevent good adhering.

A case where the analysis showed somewhat weaker indications for possible failure than the tests was that of the cell-to-substrate adhesive in the concept A design. Unlike other configurations, the cell-to-substrate adhesive in this design covered only a circular spot of about 1.6-cm in diameter. Although the analysis (Table 7) showed higher effective stress ratio in the cell-to-substrate adhesive for concept A than the ones computed for designs using the same adhesive group (such as the modified Mariner A1-6 design, silver mesh B1-6 design, or concept C design), the stress ratios were not much higher. On the other hand, tests on concept A showed indications of substantially higher stresses in the form of impending cracking in the cell around the periphery of the adhesive spot.

That Kovar is superior over palladium as an interconnector material was previously emphasized in the analysis for the P-interconnector (Section V-A) and for the N-interconnector (Section V-B). Its superiority as a P-interconnector over palladium was inferred in the test results by the percentage of filter delamination and silicon cratering failures already discussed (37% for Kovar designs versus 42% for palladium designs — both using the RTV-602 filter adhesive). Similar results were also observed with regard to the percentage of failures in the form of hairline cracks around the contact of the N-interconnector (Fig. 8). Design A1-6 with

Kovar interconnector exhibited 3% hairline crack failures, while design C1-6 with palladium interconnector showed 5% of these failures. In addition, when palladium was used along with the RTV-602/RTV-511 adhesive group the percentage of failure increased to 10%.

In terms of overall performance and susceptibility for failures, concept C was recommended on the basis of the analyses. It also showed no failures of any kind during the test program which covered sixty thermal cycles. Further improvements in the N-interconnector geometry, as suggested by configuration [5] in Section V-B, should increase the capability of this design to sustain larger number of thermal cycles than its current capability.

Other means of improving on this design include finding the optimum combination of thickness of the filter, silicon, solder, and adhesive layers. This should be possible because it is the relative thickness of the various layers, as much as the relationships of their elastic and shear moduli and coefficients of thermal expansion that determine the compatibility between them so that stresses are minimized in the composite. However, controlling the thickness of solder and adhesives would require more rigorous manufacturing methods.

Finally, because of the factors discussed in Section III-A, predictions of the number of thermal cycles to failure on the basis of stress analysis as was attempted by Ref. 2 can only be very inaccurate. A more reliable prediction of the number of thermal cycles to failure could only emerge from a statistical interpretation of tests on the candidate designs. This latter approach is currently under investigation.

REFERENCES

1. Salama, A. M., Rowe, W. M., and Yasui, R. K., "Stress Analysis and Design of Silicon Solar Cell Arrays and Related Material Properties," in Conference Record of the Ninth IEEE Photovoltaic Specialists Conference, pp. 146-157, Silver Spring, Md., May 1972.

2. Rauschenbach, H. S., and Gaylord, P. S., "Prediction of Fatigue Failures in Solar Arrays," in Proceeding of the Seventh Intersociety Energy Conversion Engineering Conference, San Diego, Calif., September, 1972.

3. Gupta, K. K., Akyuz, F. A., and Heer, E., "VISCEL - A General Purpose Computer Program for Analysis of Linear Viscoelastic Structures: User's Manual," Technical Memorandum 33-466, Vol. 1, Rev. 1, Jet Propulsion Laboratory, Pasadena, Calif., October, 1972.

4. Gupta, K. K., and Akyuz, F. A., "VISCEL - A General Purpose Computer Program for Analysis of Linear Viscoelastic Structures: Program Manual," Technical Memorandum 33-466, Vol. II, Jet Propulsion Laboratory, Pasadena, Calif., July, 1972.

5. R. E. Smith, Corning Glass Works, Nov. 12, 1971 (private communications).

6. Runyan, W. R., Silicon Semiconductor Technology, McGraw-Hill Book Co., Inc., New York, 1965.

7. Sylwestrowicz, W. D., "Mechanical Properties of Single Crystals of Silicon," Philosoph. Mag., 7-8th Series, pp. 1825-1845, 1962.

8. Thorne, J. A., "The Effect of Extreme Low Temperatures on Silicone Elastomeric Materials," Report No. 172 A, Dow Corning Corp., Aerospace Applications Laboratories, Midland, Mich., May 24, 1966.

9. Lewis, W., "A Comparison of the Low Temperature Characteristics of Various Silicone Elastomers," Dow Corning Corp., Midland, Mich., 1966.

10. Douglas, R. W., et al., "Summary Report on High Temperature Properties and Alloying Behavior of the Refractory Platinum-Group Metals." Office of Naval Research, Washington, D. C., Aug. 31, 1961.

11. Chevenard, P., and Crussard, C., Compt. rend., Vol. 215, p. 58, 1942 and Vol. 216, p. 685, 1943.

12. Koster, W., and Scherb, J., Z. Metallkunde: Vol. 49 p. 501, 1958.

13. "BMD-Biomedical Computer Programs," pp. 42-48, Health Sciences Facility, Dept. of Preventive Medicine and Public Health, School of Medicine, UCLA, Calif., Sept. 1, 1965.

14. Schwartzberg, F. R., et al., Cryogenic Materials Handbook, AD609562, TDR, No. ML-TDR-64-280. Air Force Materials Lab, Wright Patterson Air Force Base, Ohio, August 1964.

15. Aerospace Structural Materials Handbook, Vol. II, J. Wolf and W. F. Brown, Eds. Syracuse University Press, New York, 1971.

16. Nix, F. C., and MacNair, D., Phys. Rev., Vol. 61, pp. 74-78, January 1942.

17. Masumoto, H., and Sawaya, S., Japan Instit., Metals, Vol. II, No. 1, pp. 51-55, January 1970.

18. Corning Glass Works Product Bulletin, Corning, N.Y., March 1966.

Table 1. Solar cell silicon specimens tested for linear thermal expansion

Silicon type	Bulk resistivity	Type of diffusion
N	30 Ω-cm	Undiffused (control)
N	30 Ω-cm	Normal lithium diffusion (one side)
N	30 Ω-cm	Hyper lithium diffusion (both sides)
N	30 Ω-cm	Boron diffused (P/N)
P	3 Ω-cm	Undiffused (control)
P	3 Ω-cm	Phosphorous diffused (N/P)
P	10 Ω-cm	Undiffused (control)
P	10 Ω-cm	Phosphorous diffused (N/P)
Two of each type of specimen were tested.		

Table 2. Ultimate stress for single-crystal silicon tensile specimens

Type specimen and supplier	Ultimate stress, N/cm^2 (psi) × 10^{-3}			Cycles to 6895 N/cm^2 before failing	Fracture description
	+25°C	-100°C	-150°C		
P-type, Centralab No. 4		19.0 (27.5)		33	Multiple fractures, on a single smooth plane at 40 deg to specimen ℄
P-type, Heliotek (PEL) No. 1	21.4 (31.1)			—	Multiple fractures at 45 deg to specimen ℄
P-type, Heliotek No. 3		20.8 (39.1)		36	Multiple fractures, on 2 smooth planes at 40 deg to specimen ℄
N-type, Centralab No. 3		16.5 (24.0)		36	Double fracture at 90 deg to specimen ℄
N-type, Centralab No. 4		16.3 (33.6)		42	Single fracture, 90 deg to specimen ℄
N-type, Heliotek No. 1		12.7 (18.5)		36	Double fracture, 90 deg to specimen ℄
N-type, Heliotek No. 2			14.6 (21.2)	24	Single fracture, 90 deg to specimen ℄
N-type, Heliotek No. 3			16.0 (23.2)	24	Single fracture, 90 deg to specimen ℄
N-type, Heliotek No. 4		11.9 (17.3)		24	Multiple fractures, 90 deg to specimen ℄

Table 3. Ultimate stress for single-crystal silicon compressive specimens

Specimen	Maximum stress, N/cm^2 (psi) $\times 10^{-3}$		Stress at crack indication	Fracture description
	+25°C	-100°C		
P-type, Centralab (PEL) No. 2	32.2 (46.7)			Shattered. Had been loaded to -62,000 N/cm^2 (-90 ksi)
P-type, Centralab No. 3		140.4 (203.7)		Several longitudinal cracks in foot
P-type, Centralab No. 4		148.2 (215.0)	140.5 (203.8)	Did not fail
P-type, Heliotek No. 2		140.5 (204.4)	90.0 (130.6)	Multiple longitudinal cracks and inclined fractures
P-type, Heliotek No. 3		143.8 (208.5)		At least two longitudinal cracks
N-type, Centralab No. 1		130.7 (189.6)	97.2 (140.9)	Shattered
N-type, Centralab No. 3		75.8 (109.9)	50.7 (73.6)	Multiple longitudinal cracks and varied fracture
N-type, Heliotek No. 1 (PEL)	132.0 (191.5)			Single longitudinal crack and fracture at 90 deg to specimen ℄. Had been loaded to -48,000 N/cm^2 (-70 ksi)

Table 4. Candidate RTV-type silicone rubber adhesives

Trade Name	Manufacturer	Color	Generic type	Application
RTV 560	General Electric	Red	Methyl-phenyl	Solar cell-substrate
RTV 41	General Electric	White	Dimethyl	Solar cell-substrate
RTV 511/577	General Electric	White	Methyl-phenyl	Solar cell-substrate
RTV 566	General Electric	Red	Methyl-phenyl	Solar cell-substrate
RTV 602	General Electric	Transparent	Dimethyl	Filter glass-solar cell
DC 93-500	Dow Corning	Transparent	Methyl-vinyl (-phenyl)	Filter glass-solar cell
XR 63-489	Dow Corning	Transparent	Methyl-vinyl (-phenyl)	Filter glass-solar cell

Table 5. Sheet interconnector materials

Materials	Nominal composition	Thickness		Source
		cm	in.	
Kovar	29Ni-17Co-54Fe	0.152	0.060	Westinghouse, Corp.
Molybdenum	99.95% Pure	0.076	0.030	Climas Molybdenum, Inc.
Palladium	99.95% Pure	0.076	0.030	Engelhard Industries, Inc.
Silver	Pure	0.076	0.030	Engelhard Industries, Inc.
Solder	62SN-36Pb-2Ag	0.127	0.050	Alpha Metal, Inc.

Table 6. Results of visual observation of fracture surfaces of interconnector metal tensile specimens

Material	Visual observations at indicated test temperature, °C					
	-196	-100	-25	+25	+100	+200
Kovar	A	A	A	B	B	B
Molybdenum	C	D	D	D	D	D
Palladium	A	A	B	B	B	B
Silver	A	B	B	B	B	B
Solder (62Sn-36Pb-2Ag)	C	E	E	E	E	F

A = ductile-transgranular fracture with shear-type fracture surface

B = ductile-transgranular fracture with tensile-type fracture surface

C = highly brittle-type fracture

D = brittle-type fracture accompanied by moderate ductility before failure

E = necking prior to failure with brittle fracture surfaces

F = extremely ductile, deformed to needle point at +150° C

Table 7. Summary of effective stress ratios in cell interior and P-interconnector analysis

Case description and identification	Filter	Filter adhesive	P-Type silicon	Solder	P-Interconnector	Cell-to-substrate adhesive
A1-6, at -50°C, Kovar, solder-coated cell, XR63-489/RTV560	0.00065	0.0036	0.00075	0.0067	0.0009	0.005
A1-6, at -100°C, Kovar, solder-coated cell, XR63-489/RTV560	0.00175	0.0072	0.0017	0.011	0.00125	0.014
A1-6, at -185°C, Kovar, solder-coated cell, XR63-489/RTV560	0.5	0.147	0.075	0.10	0.023	0.033
A7-12, at -50°C, Kovar, solder-coated cell, RTV602/511	0.0003	0.0085	0.00077	0.0069	0.0009	0.0087
A7-12, at -100°C, Kovar, solder-coated cell, RTV602/511	0.055	0.140	0.0165	0.031	0.0057	0.011
A7-12, at -185°C, Kovar, solder-coated cell, RTV602/511	4.5	3.6	1.55	2.0	0.41	0.50
A13-14, at -185°C, Kovar, solderless cell, RTV602/41	0.75	0.41	1.25	—	0.267	0.67
A15-16, at -185°C, Kovar, solderless cell, XR63-489/RTV560	0.5	0.235	0.15	—	0.073	0.15

Table 7 (contd)

Case description and identification	Filter	Filter adhesive	P-Type silicon	Solder	P-Interconnector	Cell-to-substrate adhesive
B1-6, at -185°C, silver mesh, solder-coated cell, XR63-489/RTV560	0.15	0.117	0.10	0.08	0.04	0.1167
B13-14, at -185°C, silver mesh, solderless cell, RTV602/41	1.0	5.0	5.0	—	5.0	10.0
C1-6, at -185°C, palladium, solder-coated cell, XR63-489/RTV560	0.70	0.235	0.125	0.16	0.07	0.0875
C13-14, at -185°C, palladium, solderless cell, RTV602/41	2.25	5.67	3.75	—	3.29	2.4
Concept A, at -185°C, Kovar, solderless cell, XR63-489/RTV560	0.10	0.076	0.02	—	0.01	0.183
Concept C, at -185°C, Kovar, solder-coated cell, XR63-489/RTV560	0.35	0.141	0.0325	0.06	0.02	0.075

Table 8. Summary of effective stress ratios in N-interconnector and P-interconnector bend analysis

Configuration No.	P-interconnector bend	N-interconnector	Solder	Silicon	Adhesive to substrate
[1]	0.12 at B_0	0.09 at A_4	0.4 at B_7	0.2 at A_9	0.1 at A_{10}
[2]	0.23 at B_0	0.23 at A_4	0.42 at B_7	0.2 at A_9	0.1 at A_{10}
[3]	1.0 at B_0	1.11 at A_1	2.1 at A_7	0.32 at A_8	0.5 at A_{10}
[4]	0.09 at B_0	0.05 at A_4	0.5 at B_7	0.4 at A_9	0.12 at A_{10}
[5]	0.10 at B_0	0.13 at A_2	0.27 at B_7	0.175 at A_9	0.11 at A_{10}

HELIOTEK SOLAR CELLS:

MODULES #1 THRU #12 - 2X2 cm X 14 MIL THK, 2Ω-cm, Ag-Ti PLATING, SOLDER COATED

MODULES #13 THRU #16 - 2X2 cm X 14 MIL THK, 2Ω-cm. a Ag-Ti-Al PLATING, SOLDERLESS

OCLI COVERSLIDE:

MODULES #1 THRU #12 - 2X2 cm X 6 MIL THK, 0211 MICROSHEET WITH 410 CUTOFF + AR COATING

MODULES #13 THRU # 16 - 2X2 cm X 6 MIL THK, 7940 FUSED SILICA WITH 410 CUTOFF + AR COATING

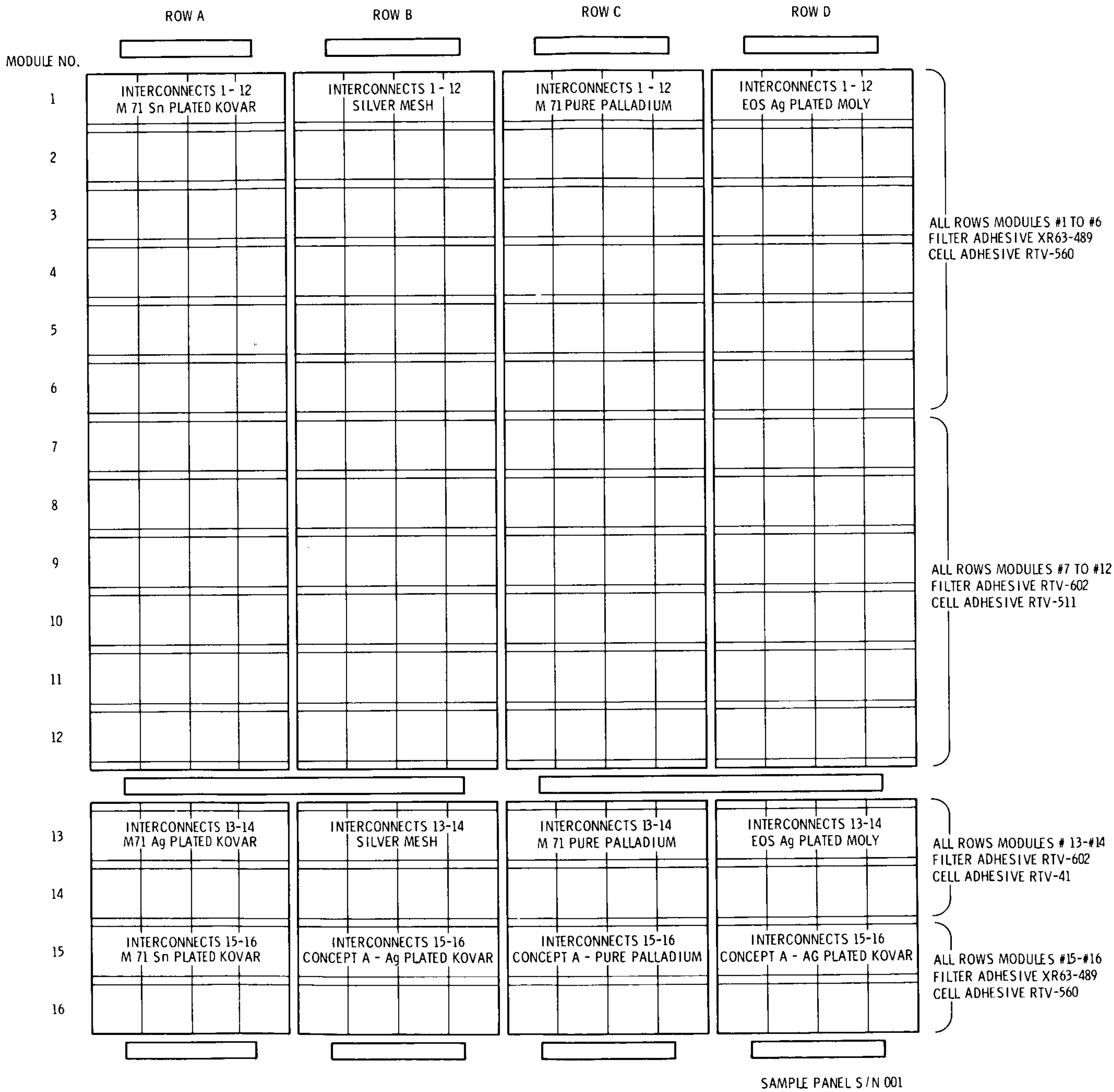

Fig. 1. Viking Orbiter 1975 sample solar panel

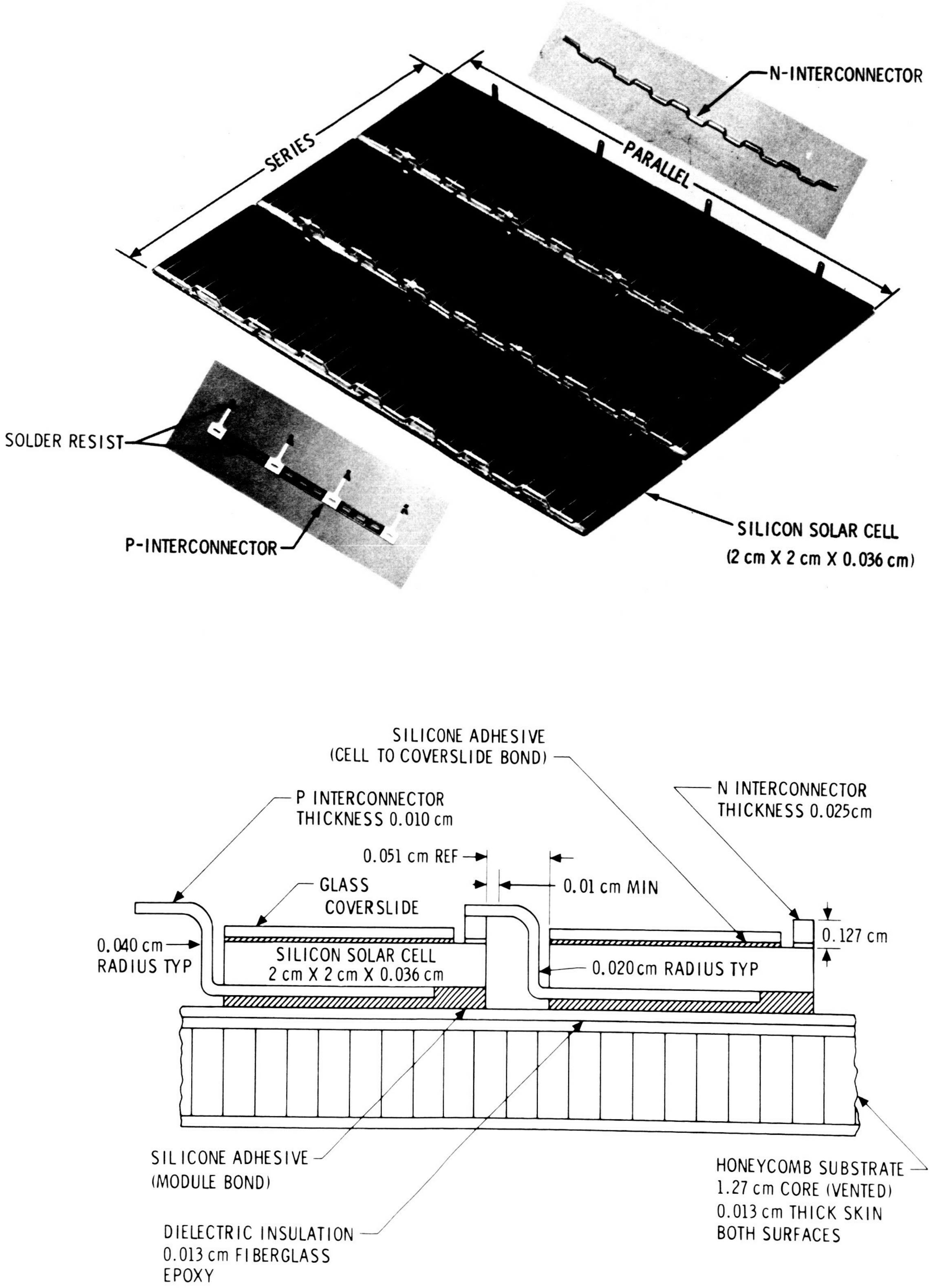

Fig. 2. Mariner 1969/1971 solar cell configuration

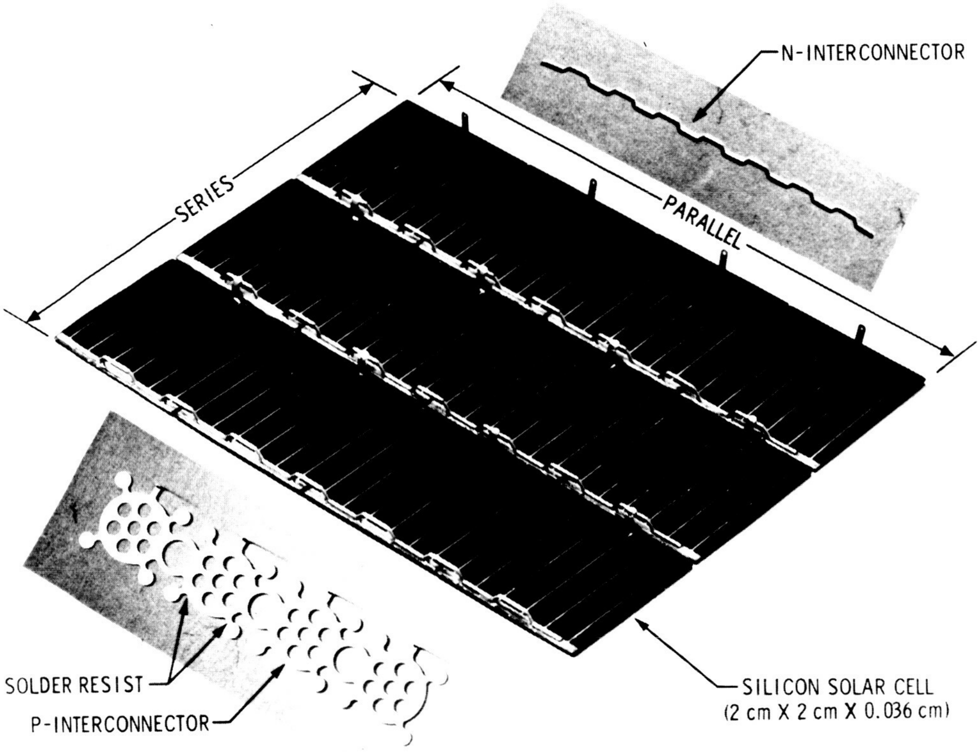

SEE CROSS SECTION ON FIG. 2

Fig. 3. Concept A solar cell configuration

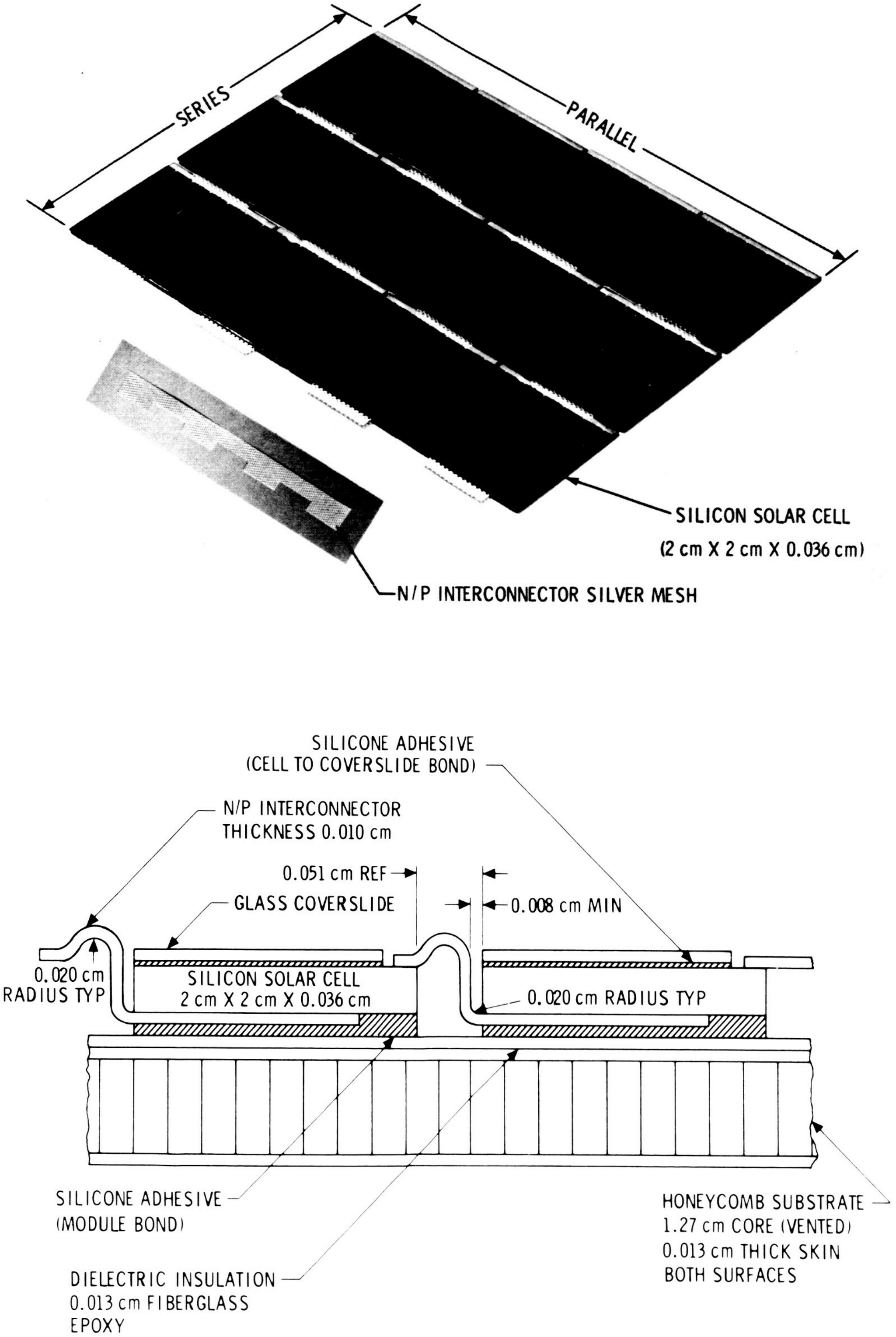

Fig. 4. Silver-mesh interconnector concepts

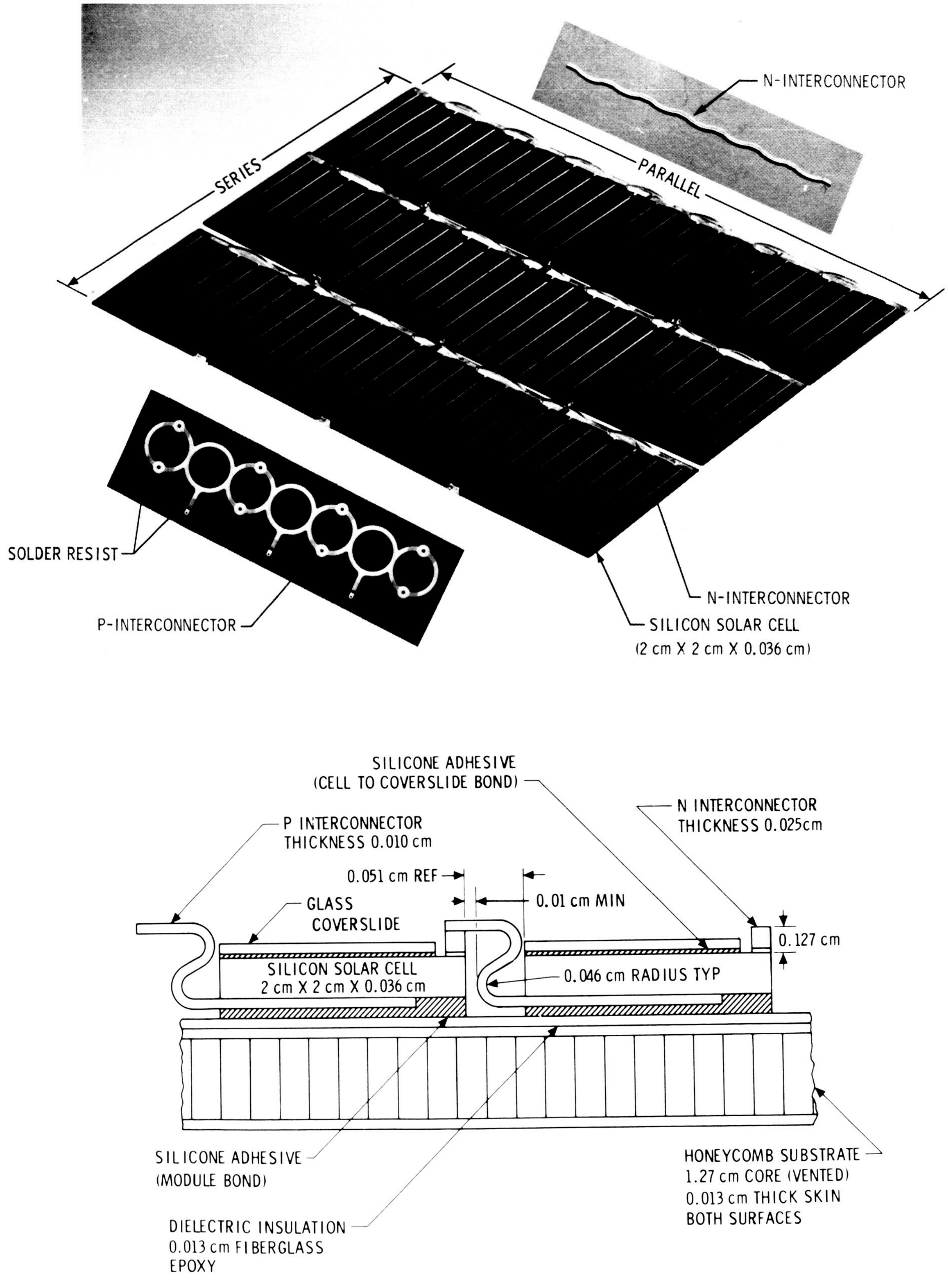

Fig. 5. Concept C solar cell configuration

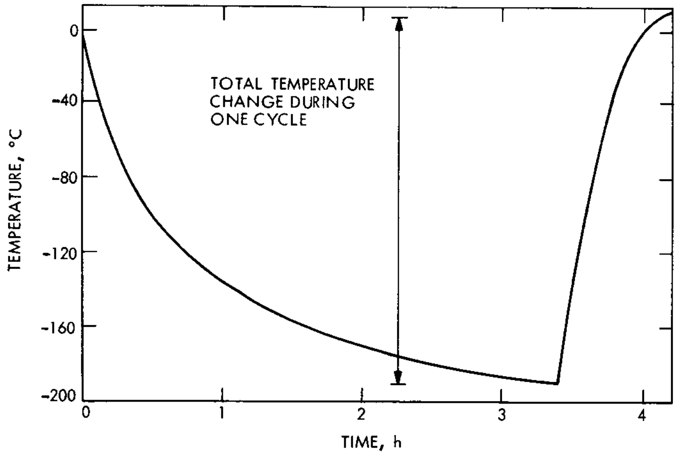

Fig. 6. Typical solar cell temperature profile during sun occultation

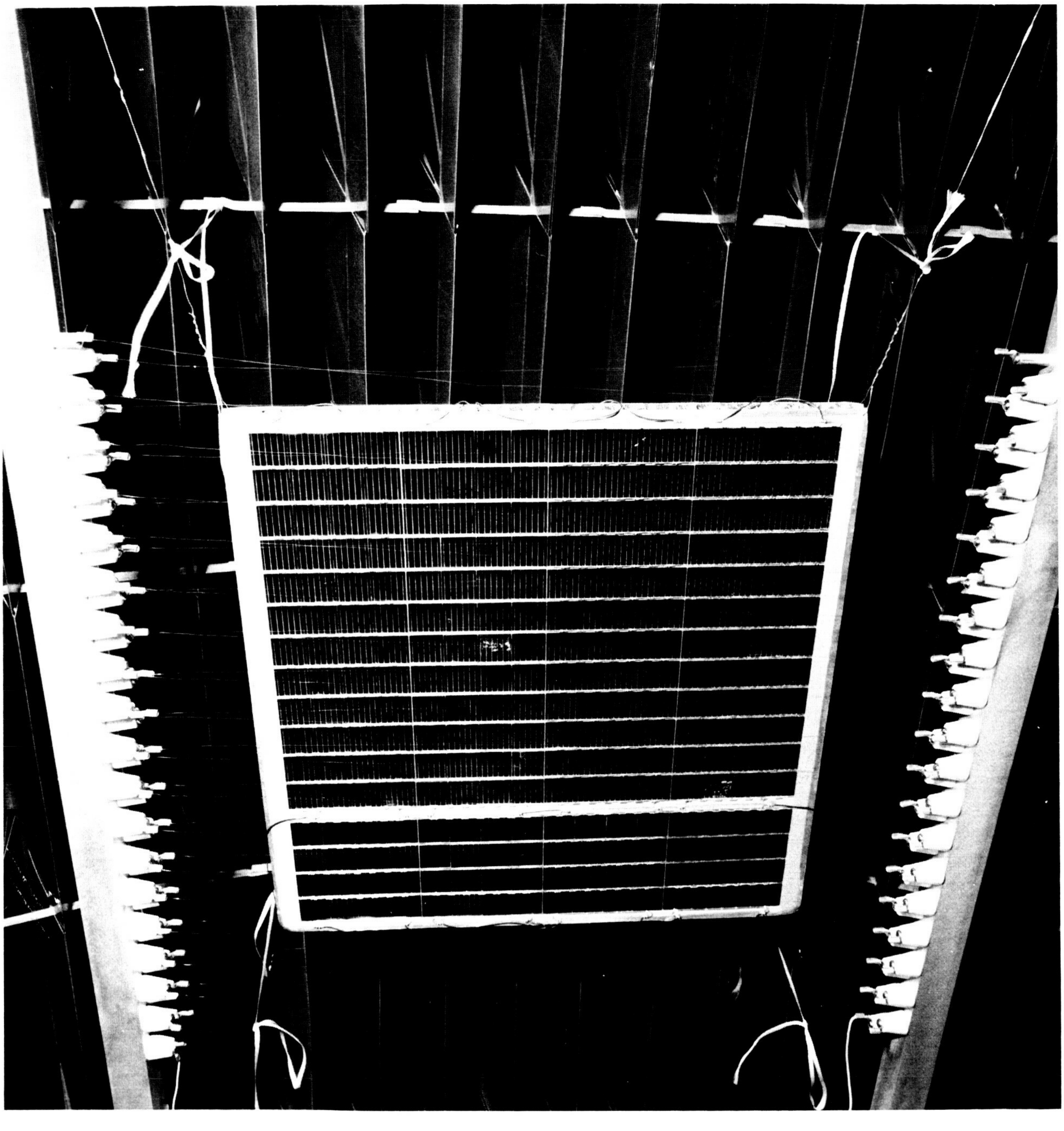

Fig. 7. Viking Orbiter sample panel 002 post-environmental test setup in Molsink showing delamination and damage to coverslide

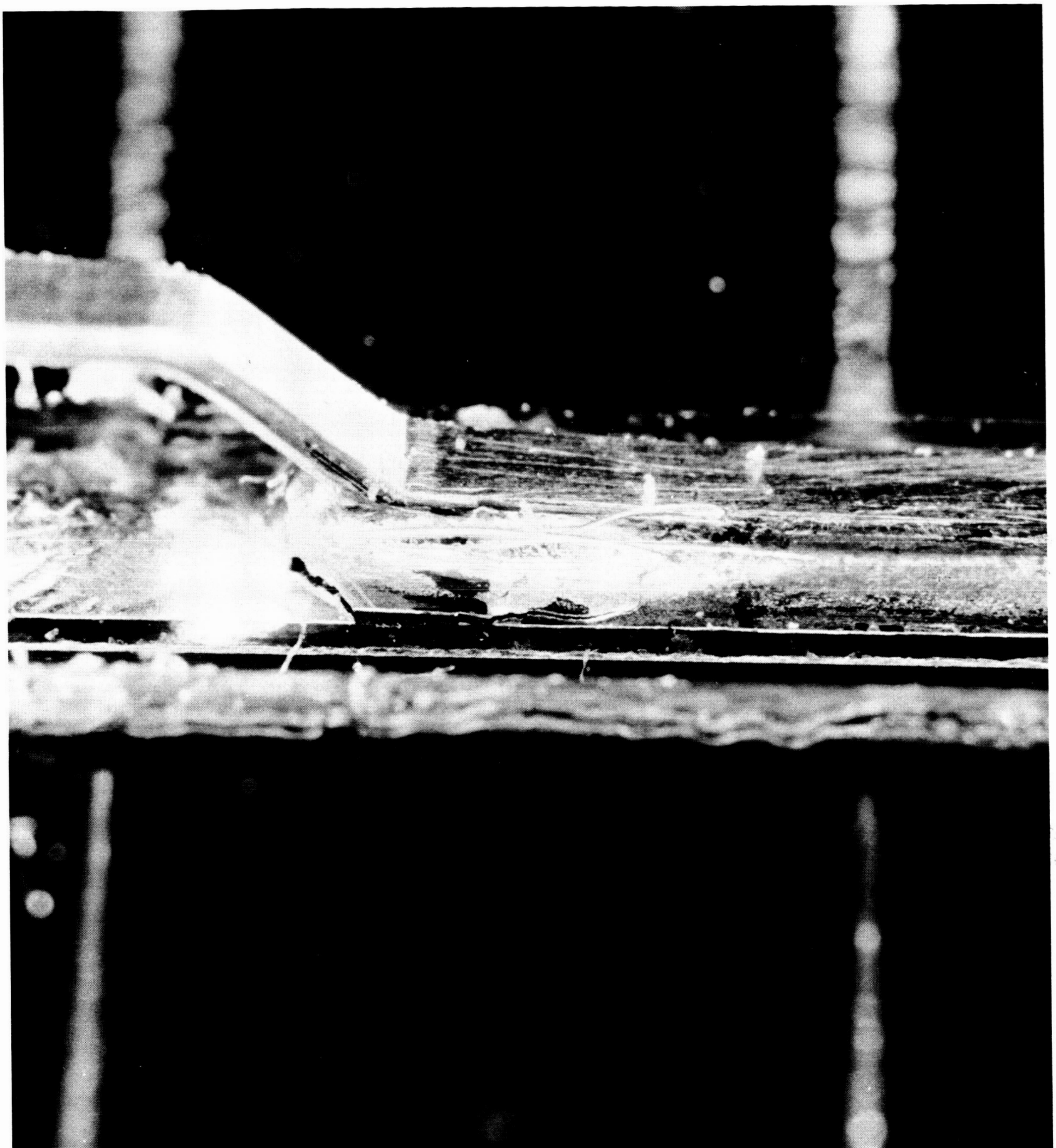

Fig. 8. N-interconnector solder joint failure (configuration C7-12)

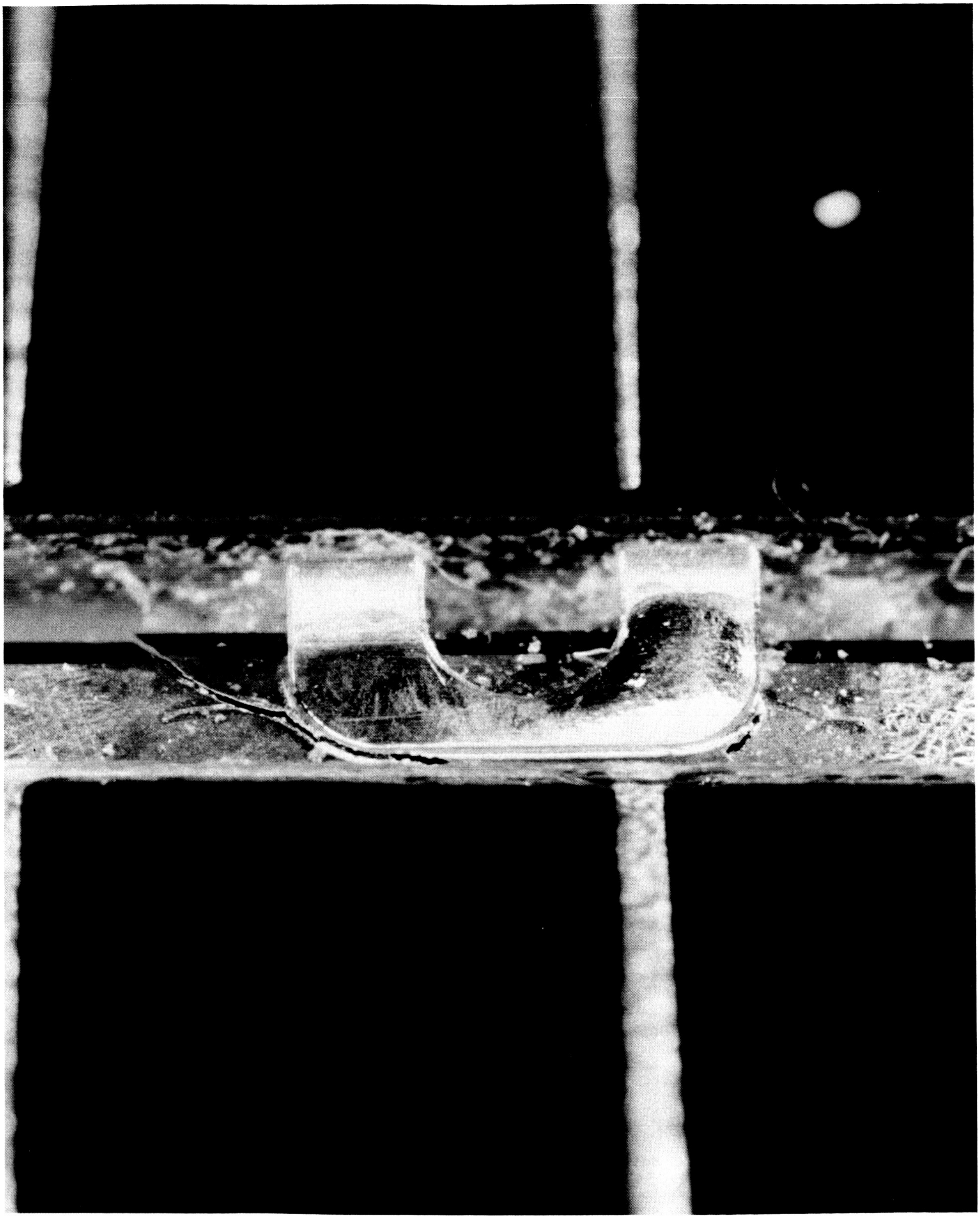

Fig. 9. N-interconnector solder joint failure (configuration D1-12)

Fig. 10. Typical coverglass bonding adhesive delamination followed by shrinkage of adhesive after thermal cycling test

Fig. 11. Extensive damage in silicon cell surface after exposure to thermal cycling test

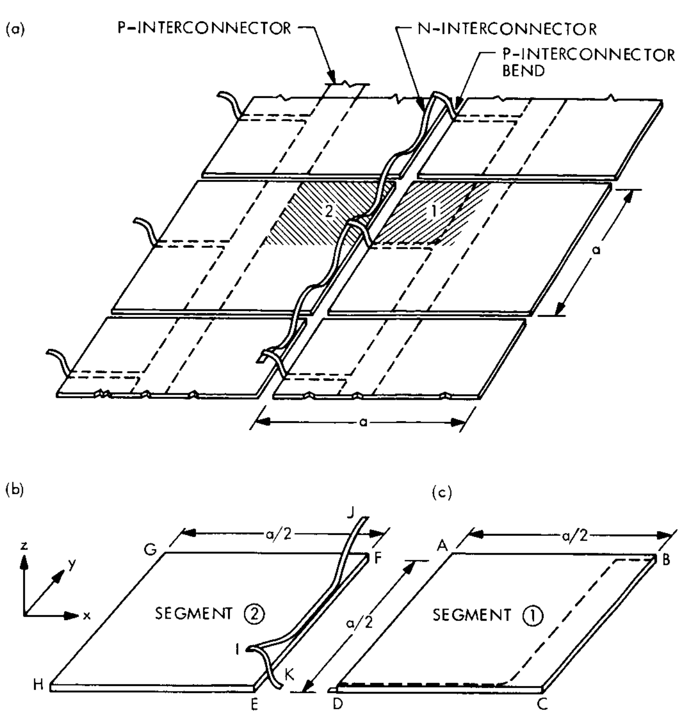

Fig. 12. Basic Mariner 1969/1971 solar cell configuration partitioned for modeling purposes into two segments: (a) array solar cell; (b) segment (2) partition; (c) segment (1) partition

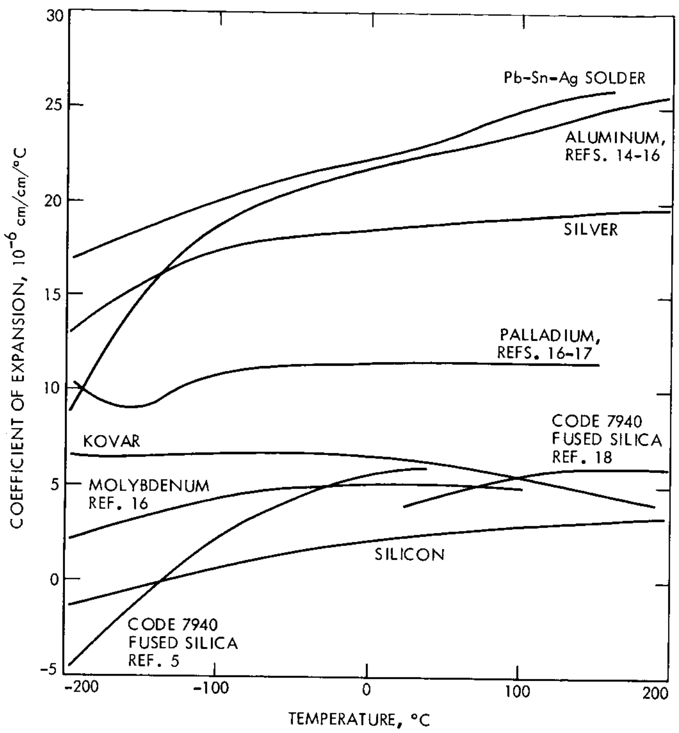

Fig. 13. Coefficient of thermal expansion versus temperature for silicon, fused silica and various metals and alloys

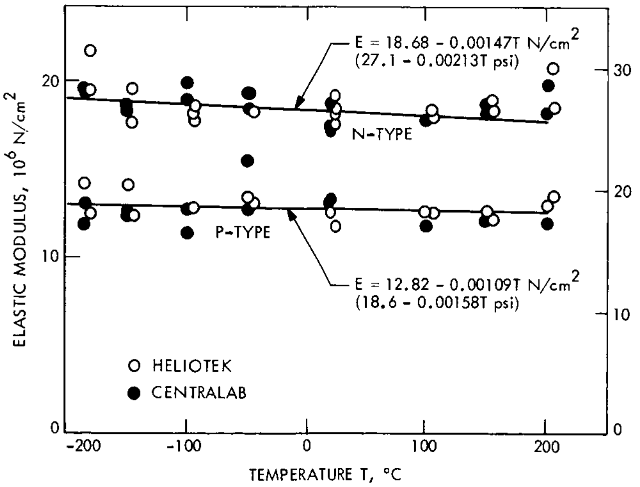

Fig. 14. Variation of elastic modulus with temperature for nondestructive tensile evaluations of single-crystal silicon

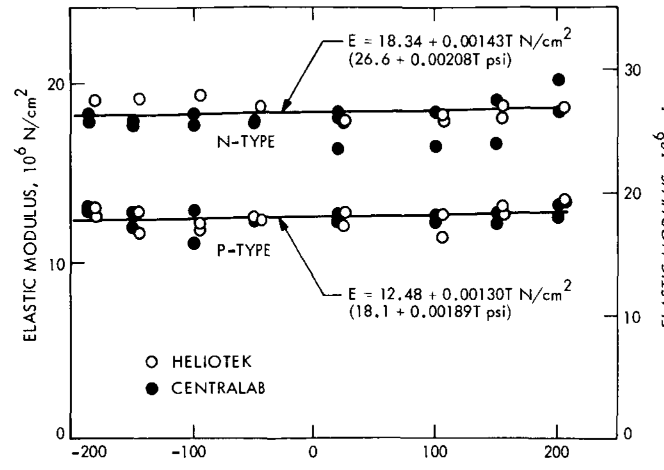

Fig. 15. Variation of elastic modulus with temperature for nondestructive compressive evaluations of single-crystal silicon

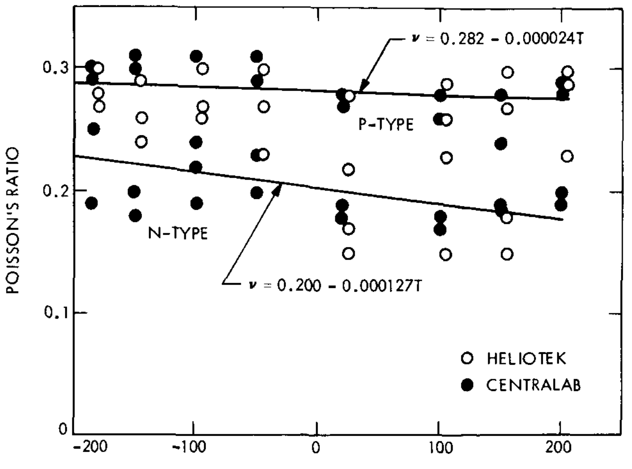

Fig. 17. Variation of Poisson's ratio with temperature for nondestructive compressive evaluations of single-crystal silicon

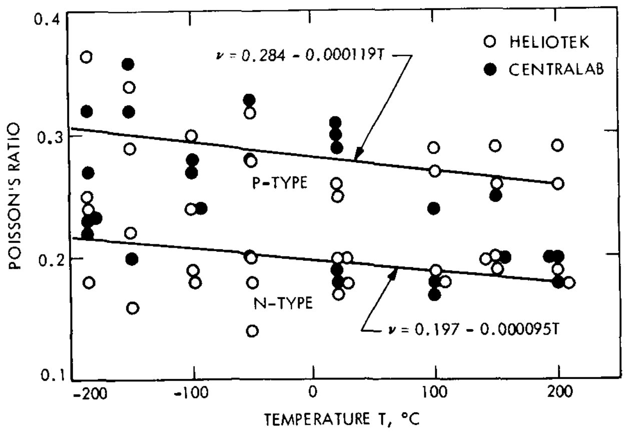

Fig. 16. Variation of Poisson's ratio with temperature for nondestructive tensile evaluations of single-crystal silicon

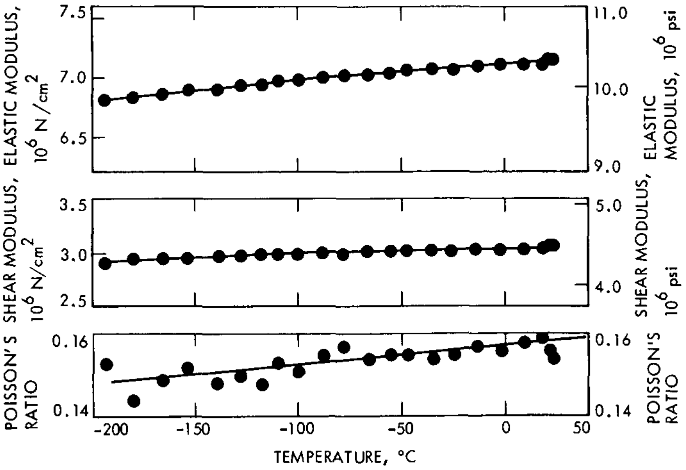

Fig. 18. Low-temperature elastic properties of glass code 7940 fused silica

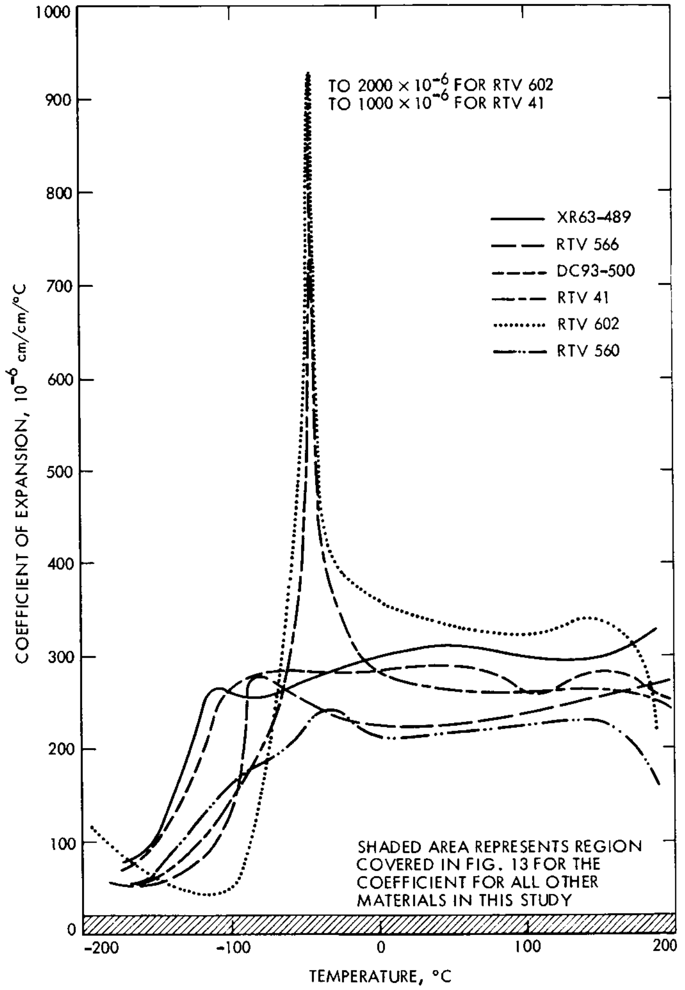

Fig. 19. Coefficient of thermal expansion versus temperature for six RTV-type silicone rubber adhesives

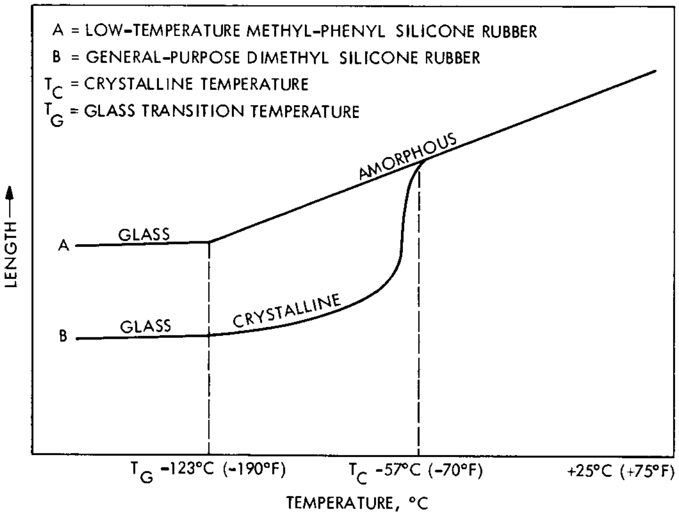

Fig. 20. RTV silicone rubber transition temperatures

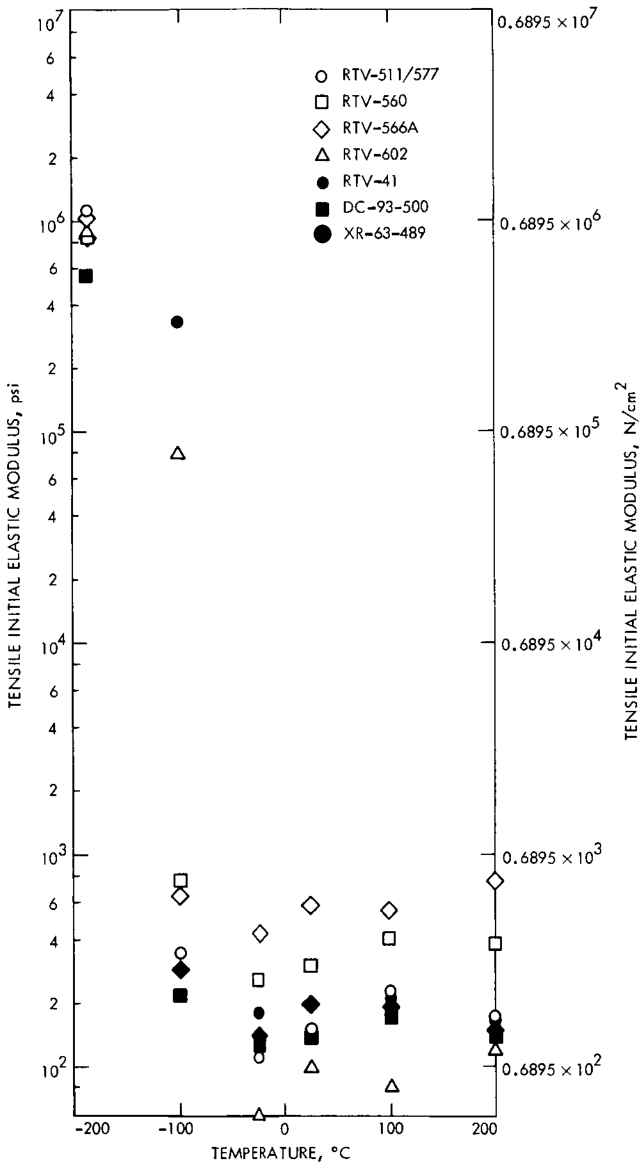

Fig. 21. Initial elastic modulus in tension versus temperature

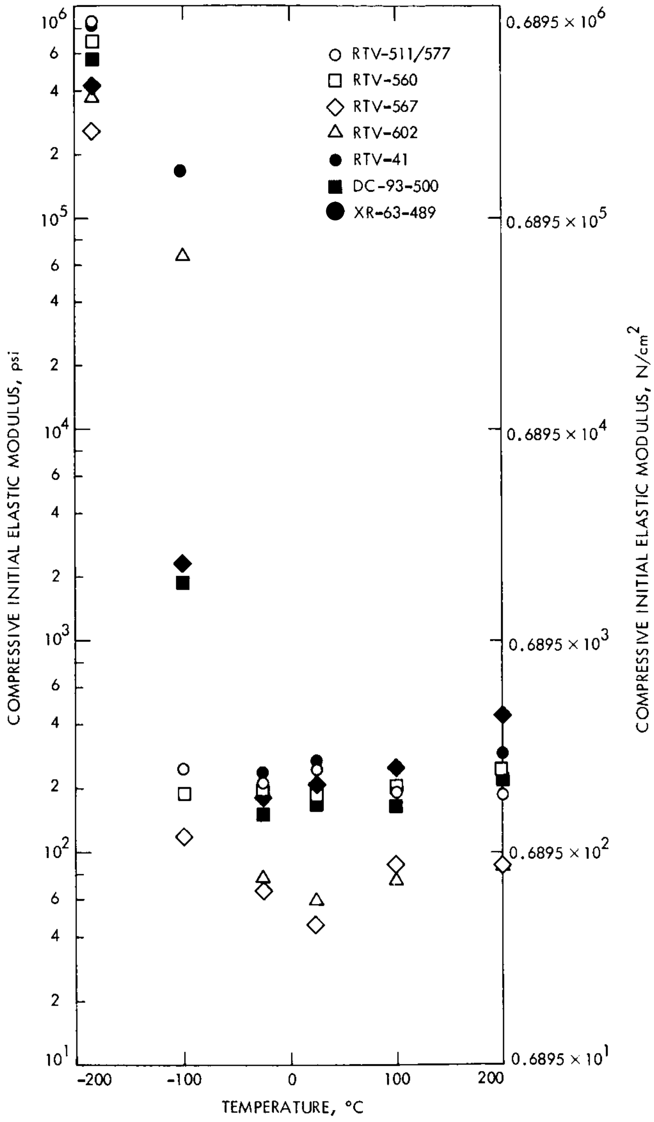

Fig. 22. Initial elastic modulus in compression versus temperature of RTV silicone adhesives

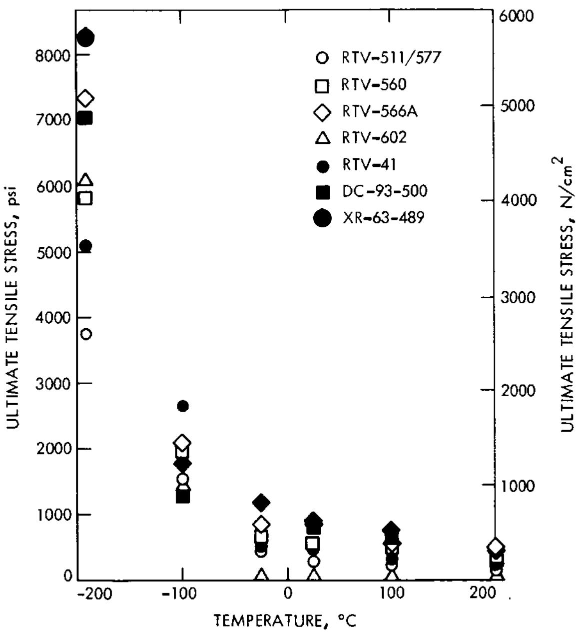

Fig. 23. Ultimate tensile stress versus temperature of silicone adhesives (average)

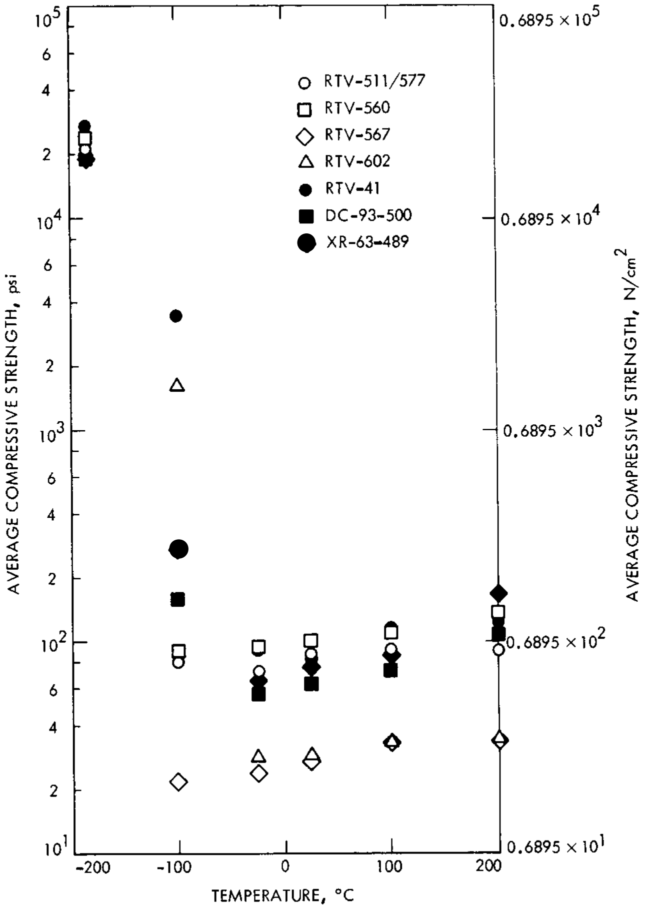

Fig. 24. Compressive strength versus temperature of RTV silicone adhesives

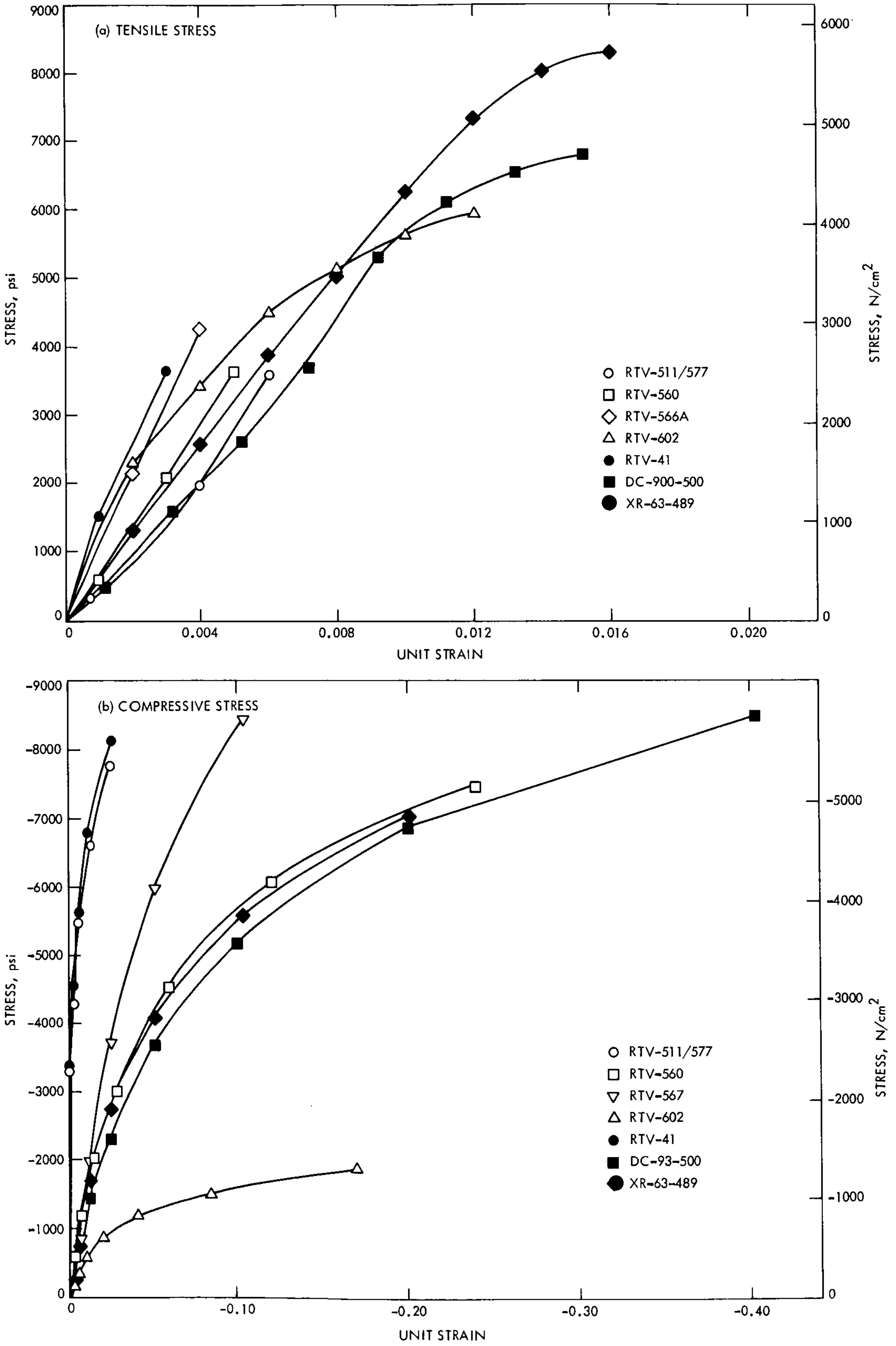

Fig. 25. Stress versus strain of RTV silicone adhesives at -184°C

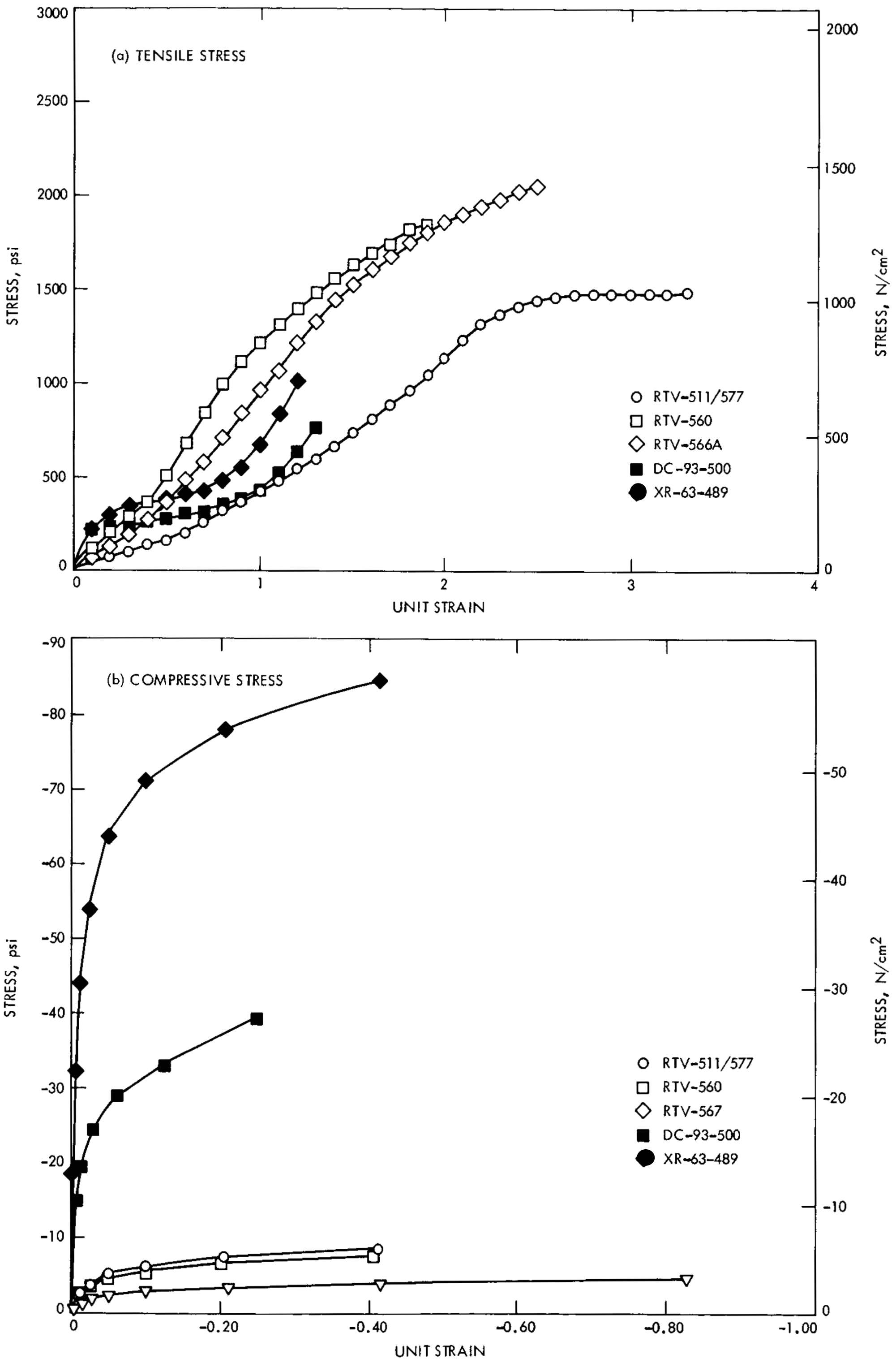

Fig. 26. Stress versus strain of RTV silicone adhesives at -100°C for five samples

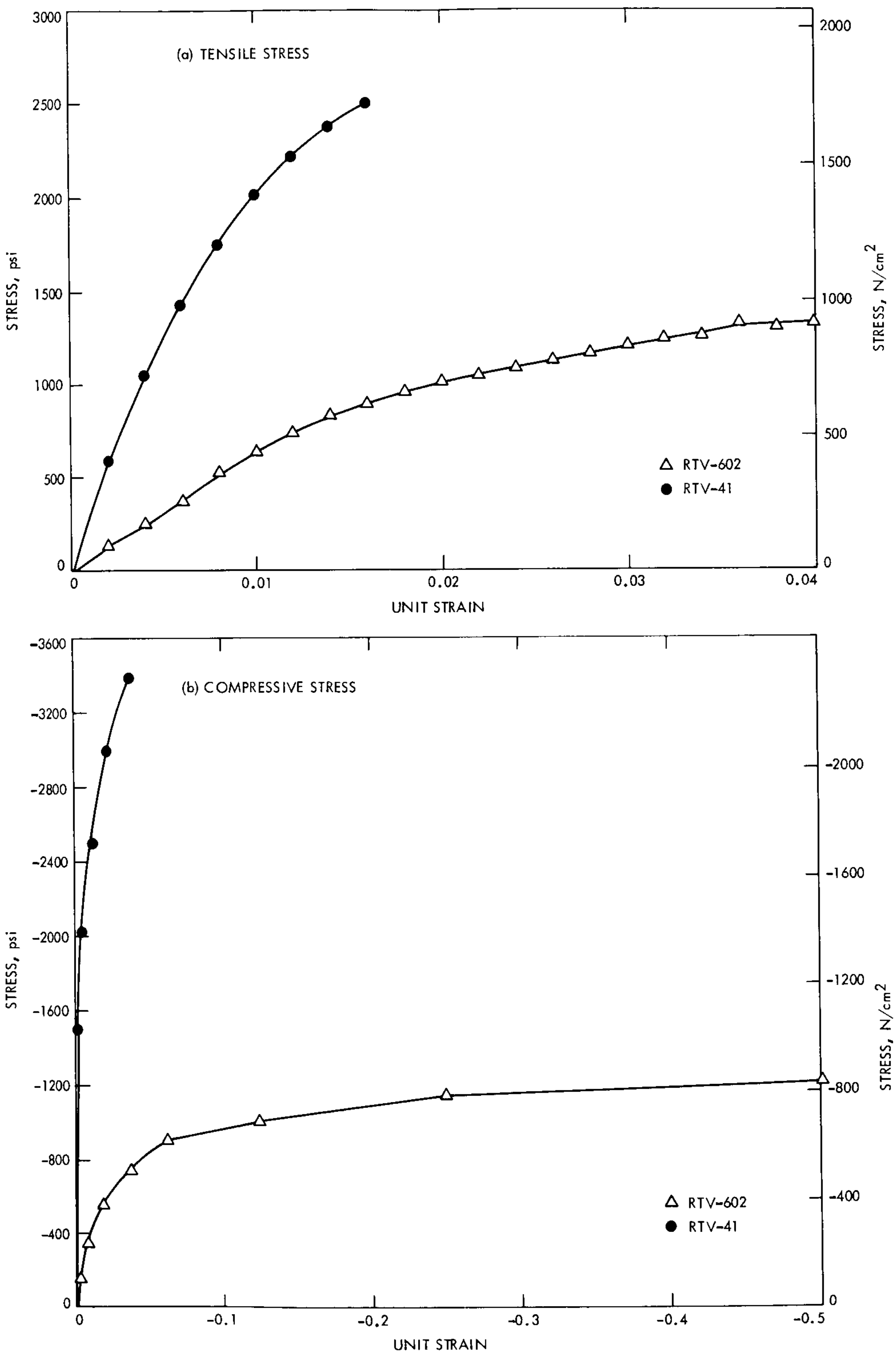

Fig. 27. Stress versus strain of RTV silicone adhesives at -100°C for two samples

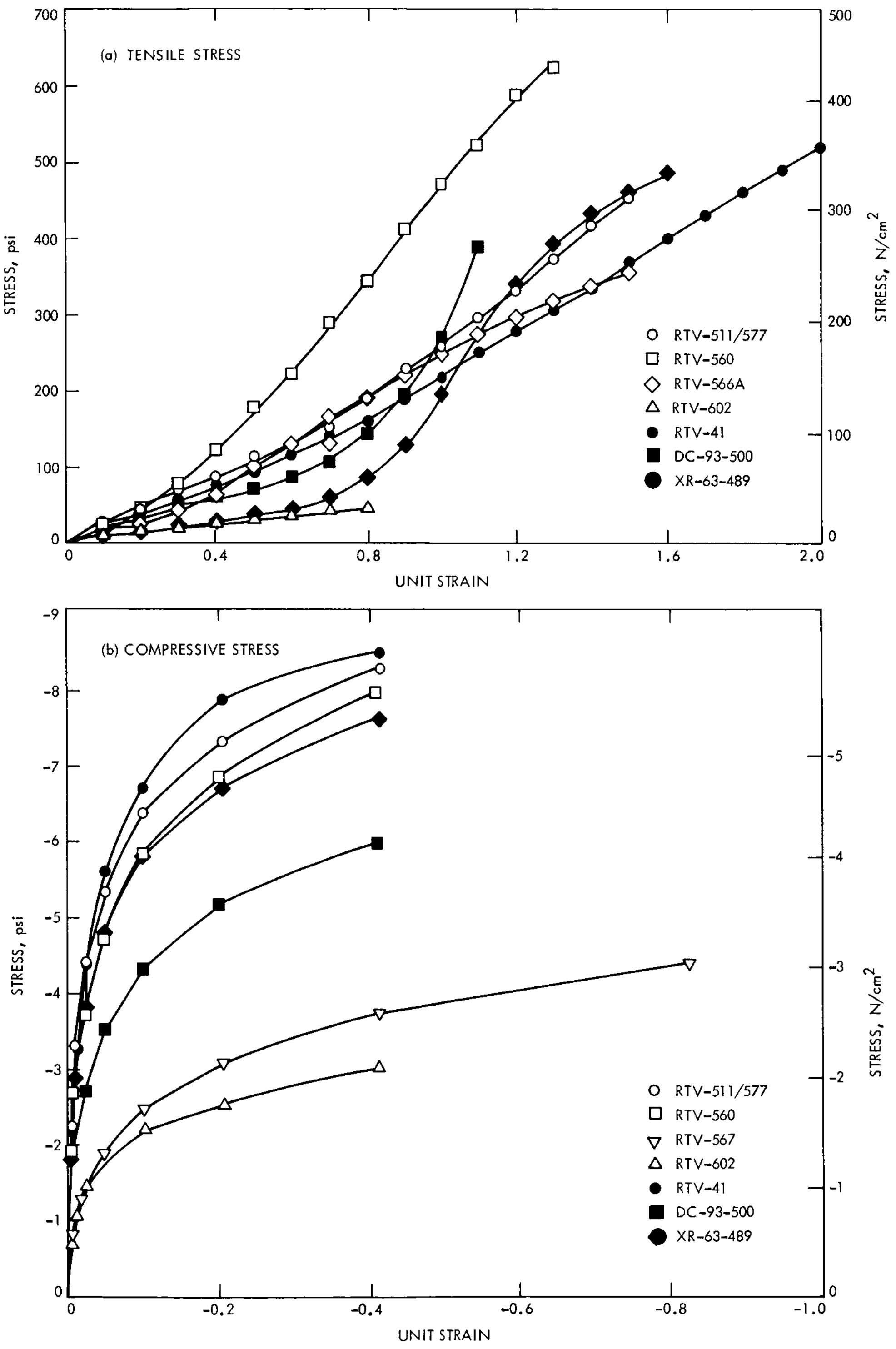

Fig. 28. Stress versus strain of RTV silicone adhesives at -25°C

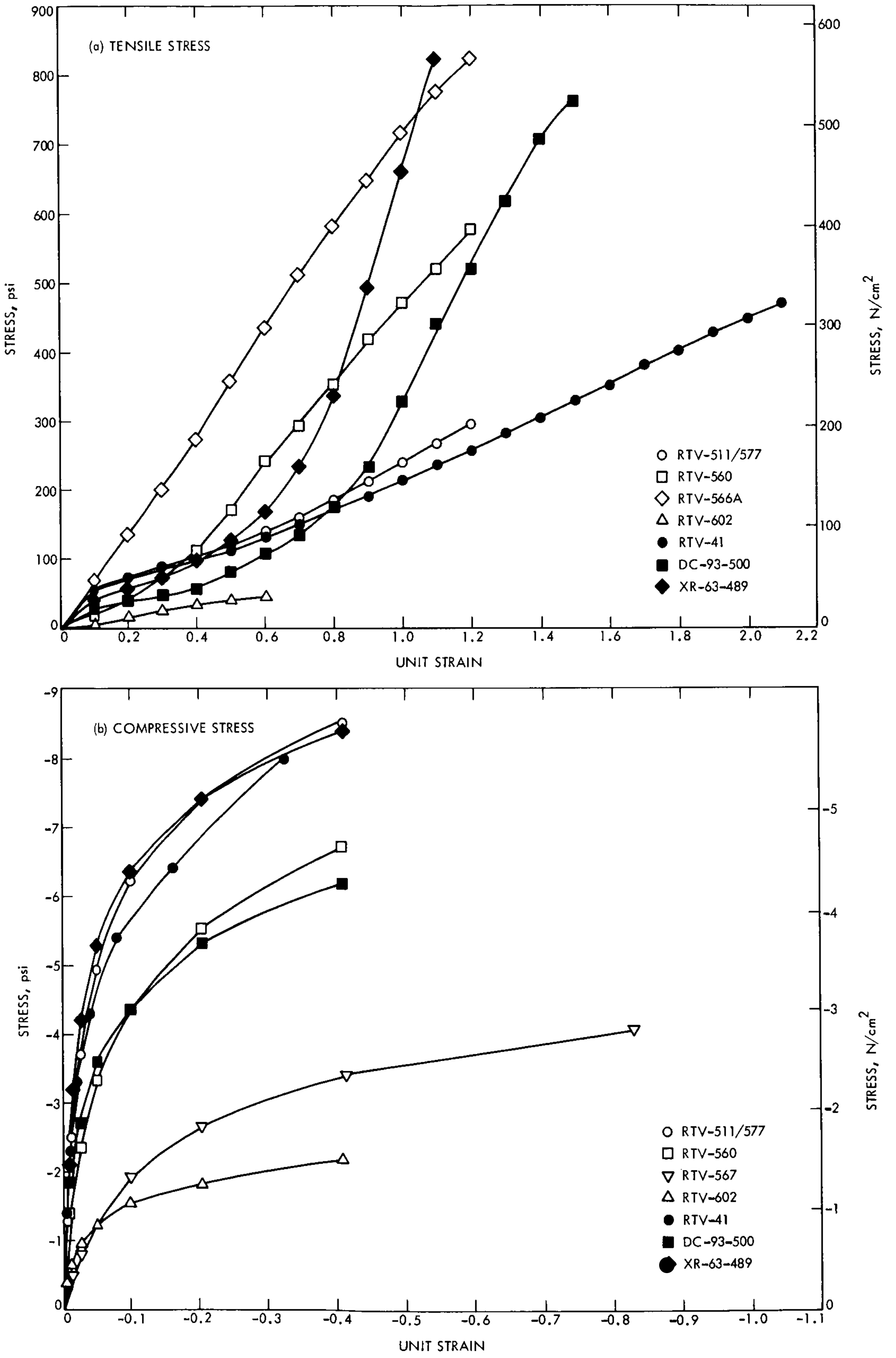

Fig. 29. Stress versus strain of RTV silicone adhesives at 25°C

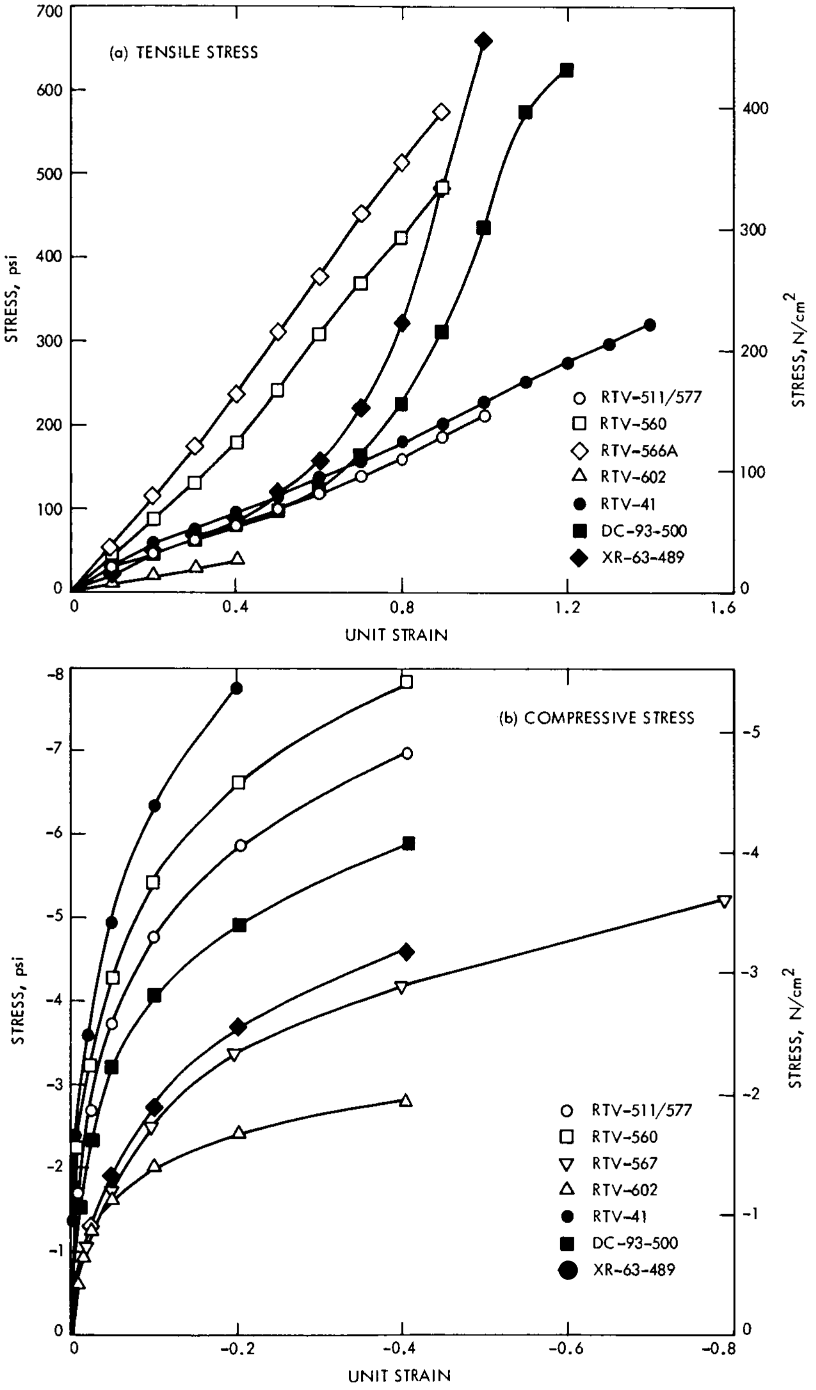

Fig. 30. Stress versus strain of RTV silicone adhesives at 100°C

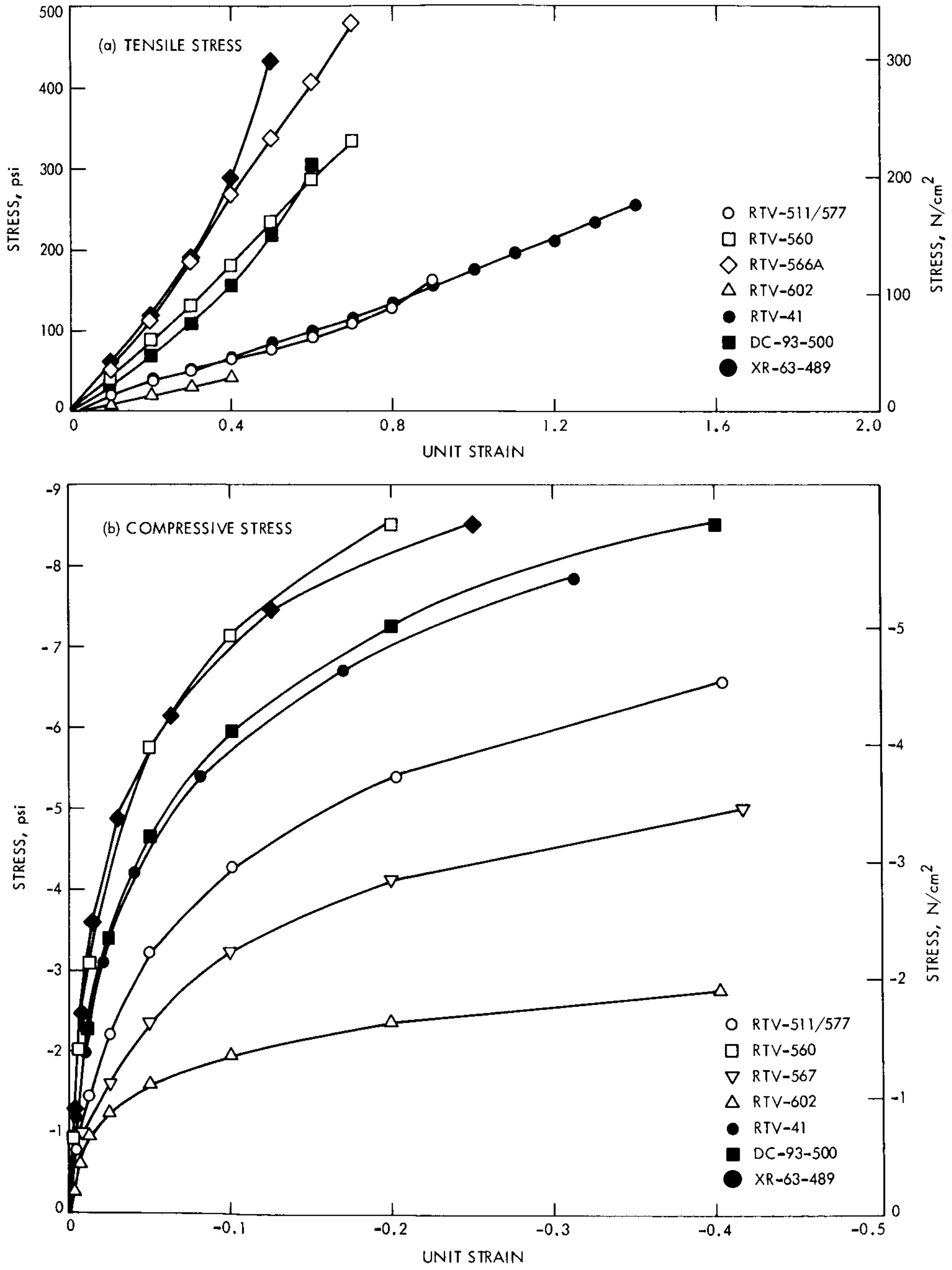

Fig. 31. Stress versus strain of RTV silicone adhesives at 200°C

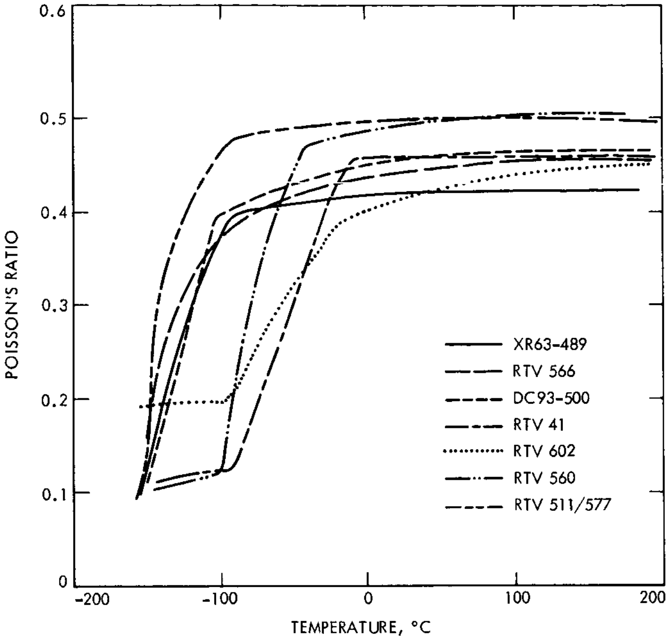

Fig. 32. Poisson's ratio versus temperature for various RTV silicone adhesives

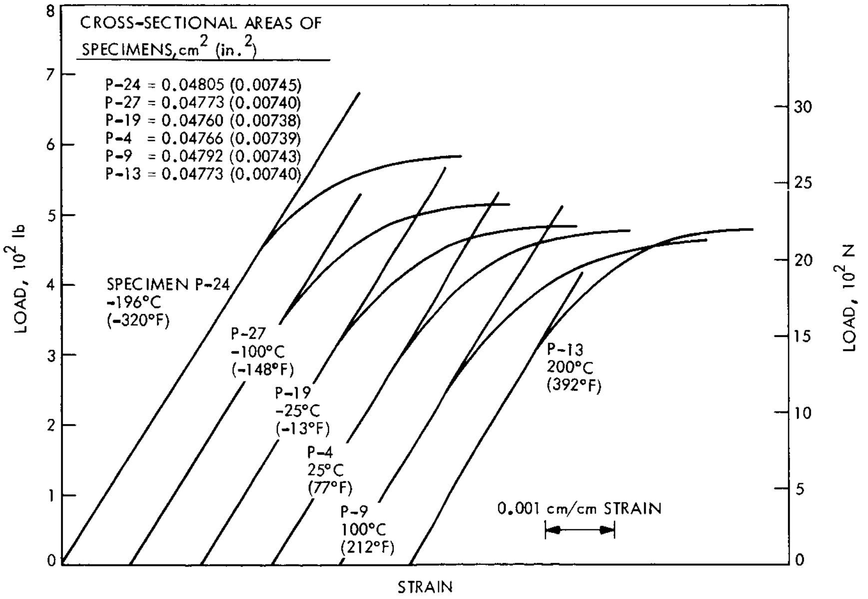

Fig. 33. Longitudinal stress-strain curves for pure palladium

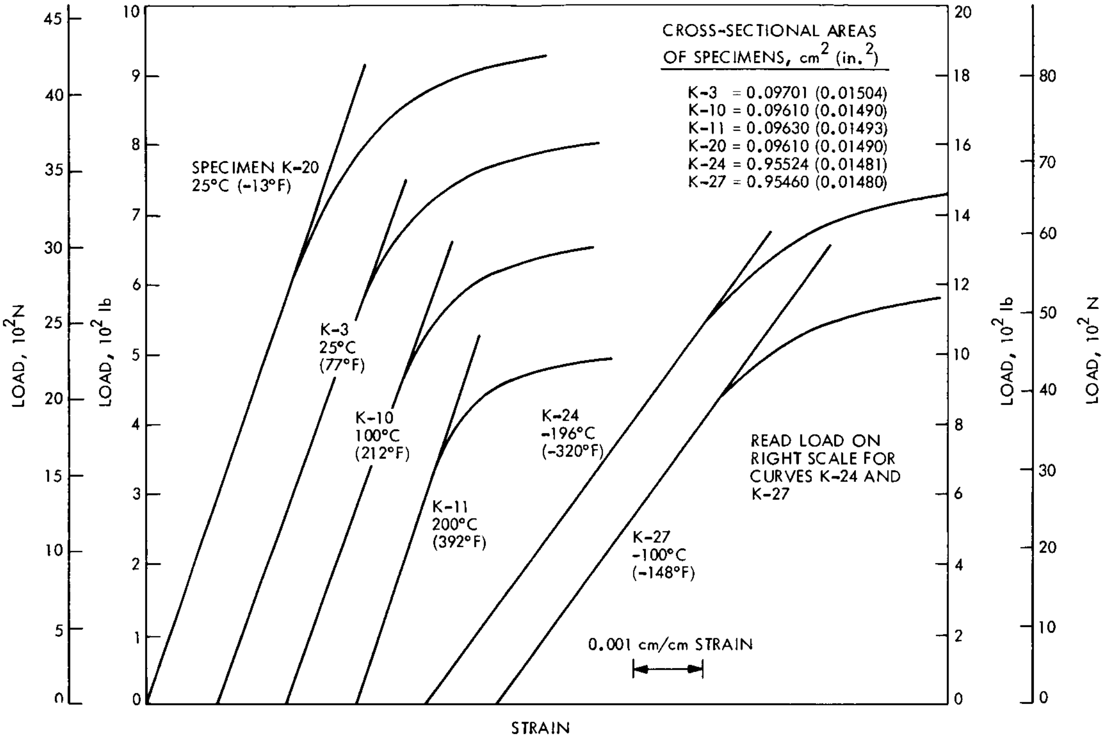

Fig. 34. Longitudinal stress-strain curves for Kovar

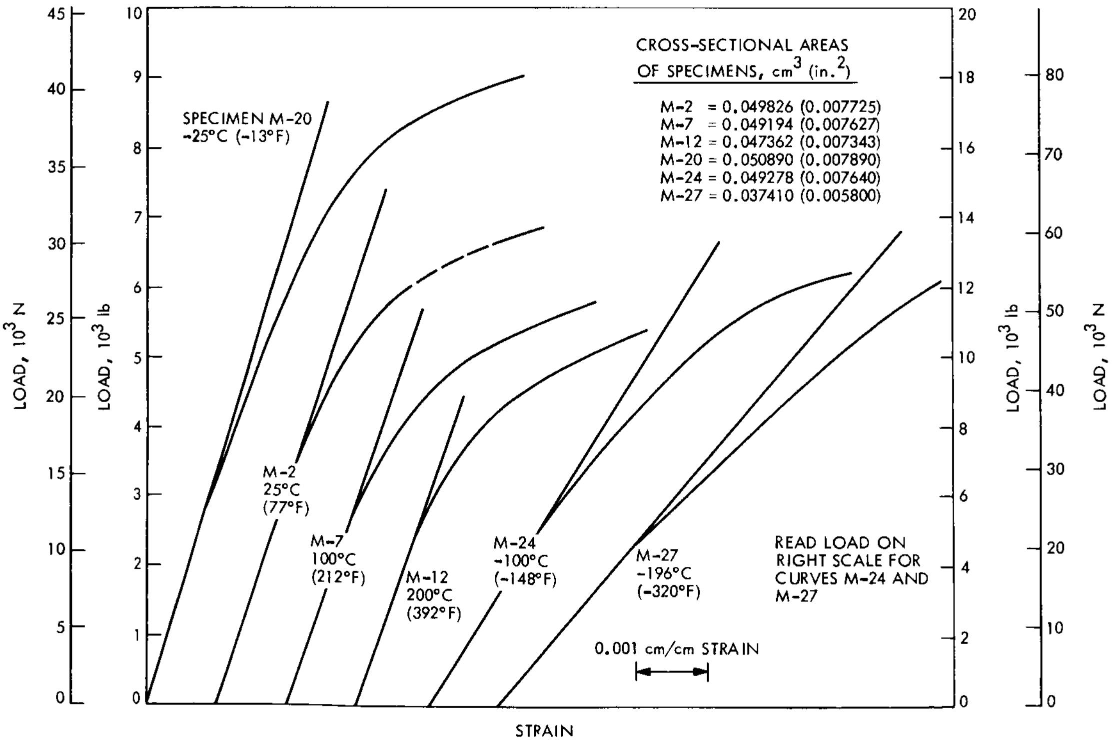

Fig. 35. Longitudinal stress-strain curves for pure molybdenum

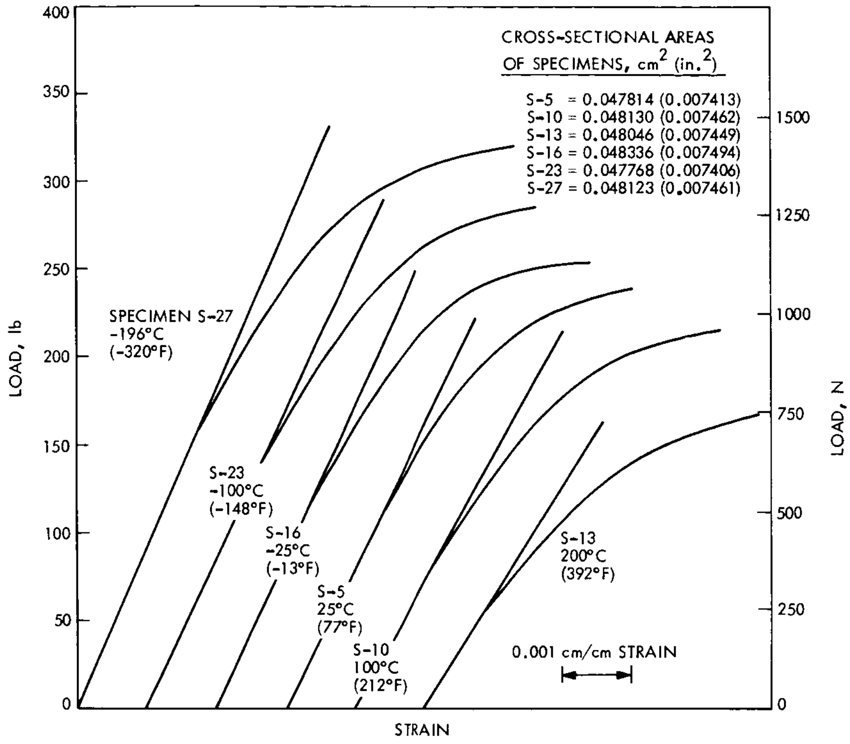

Fig. 36. Longitudinal stress-strain curves for pure silver

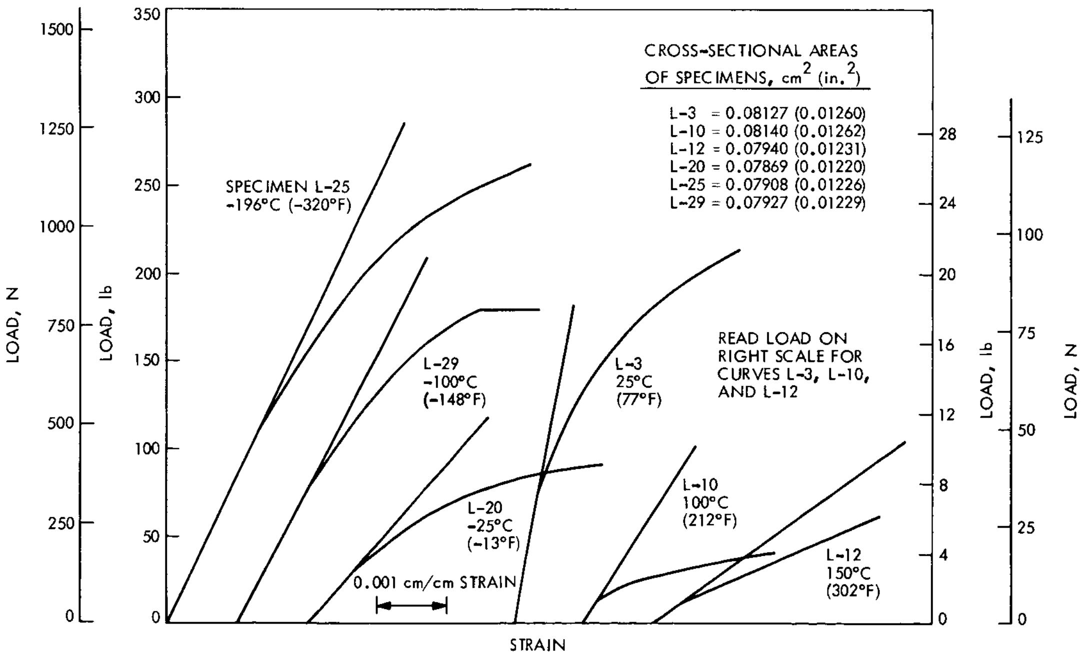

Fig. 37. Longitudinal stress-strain curves for solder (62Sn-36Pb-2Ag)

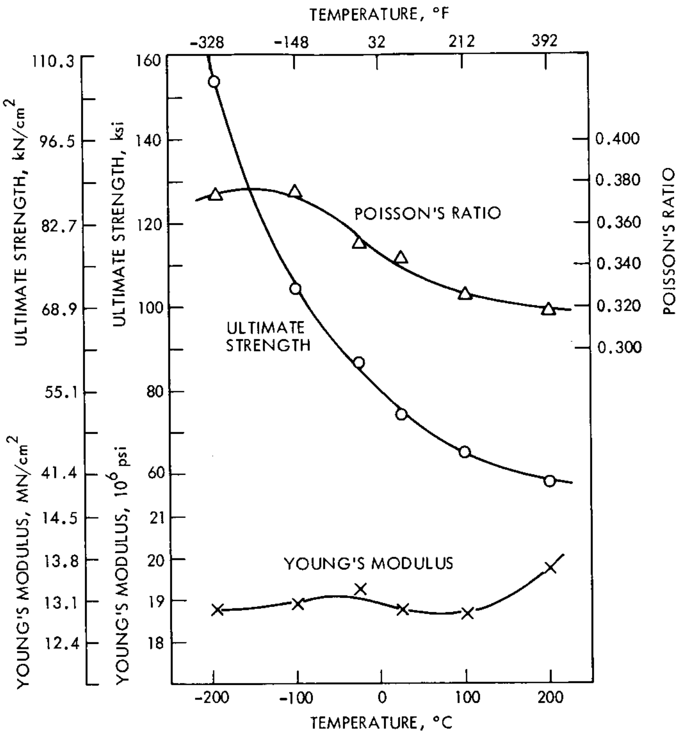

Fig. 38. Mechanical properties versus temperature for Kovar

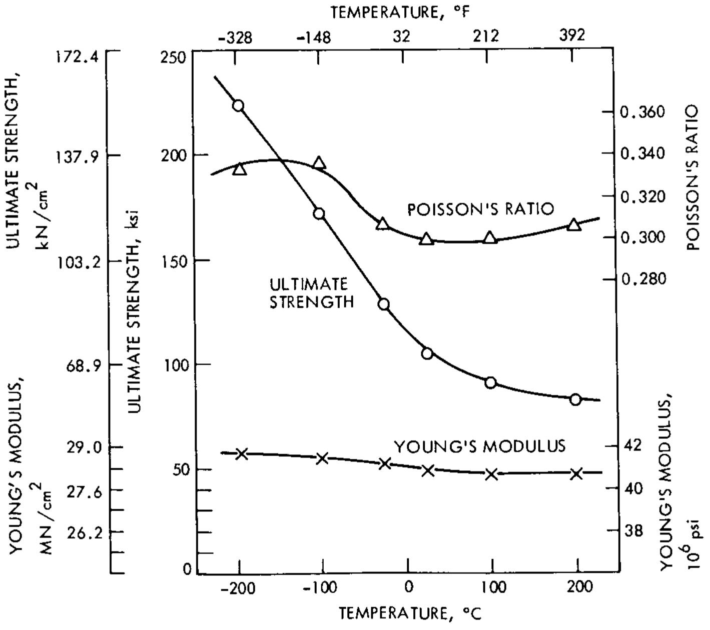

Fig. 39. Mechanical properties versus temperature for pure molybdenum

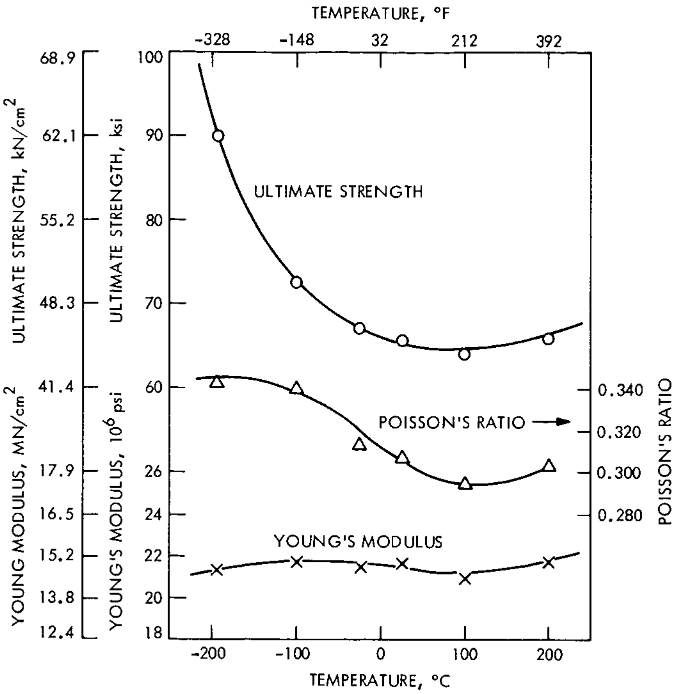

Fig. 40. Mechanical properties versus temperature for pure palladium

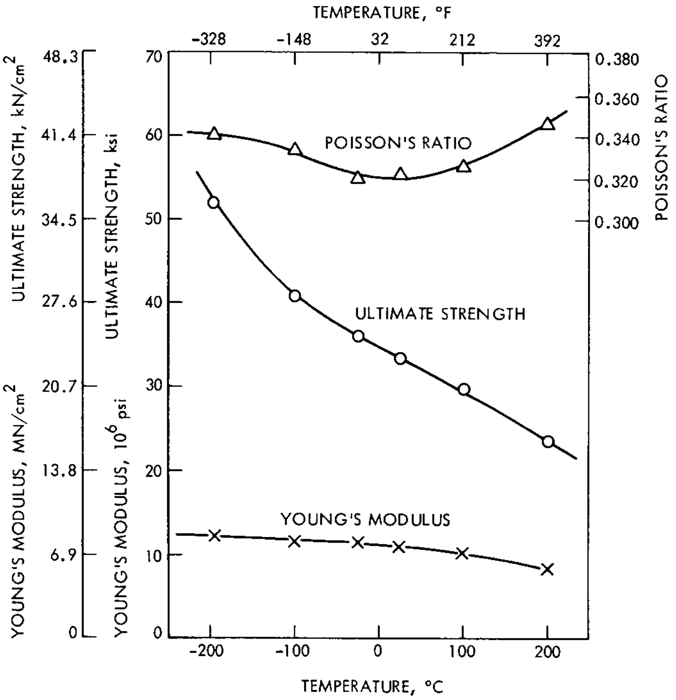

Fig. 41. Mechanical properties versus temperature for pure silver

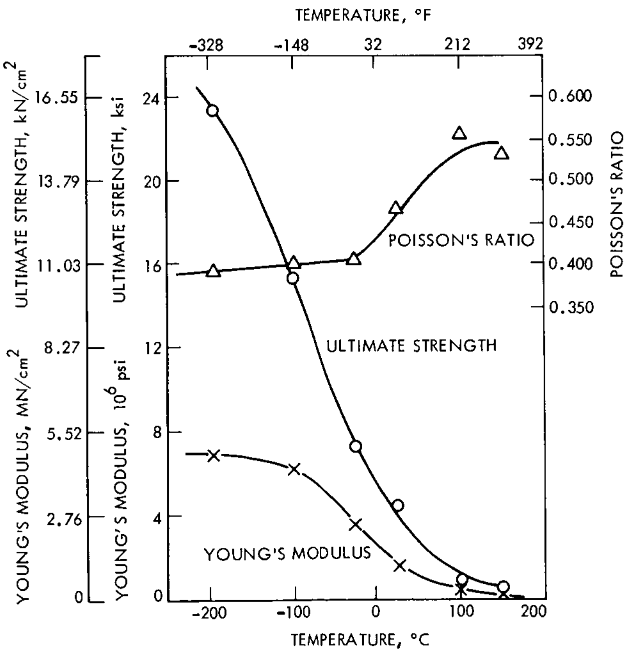

Fig. 42. Mechanical properties versus temperature for solder (62Sn-36Pb-2Ag)

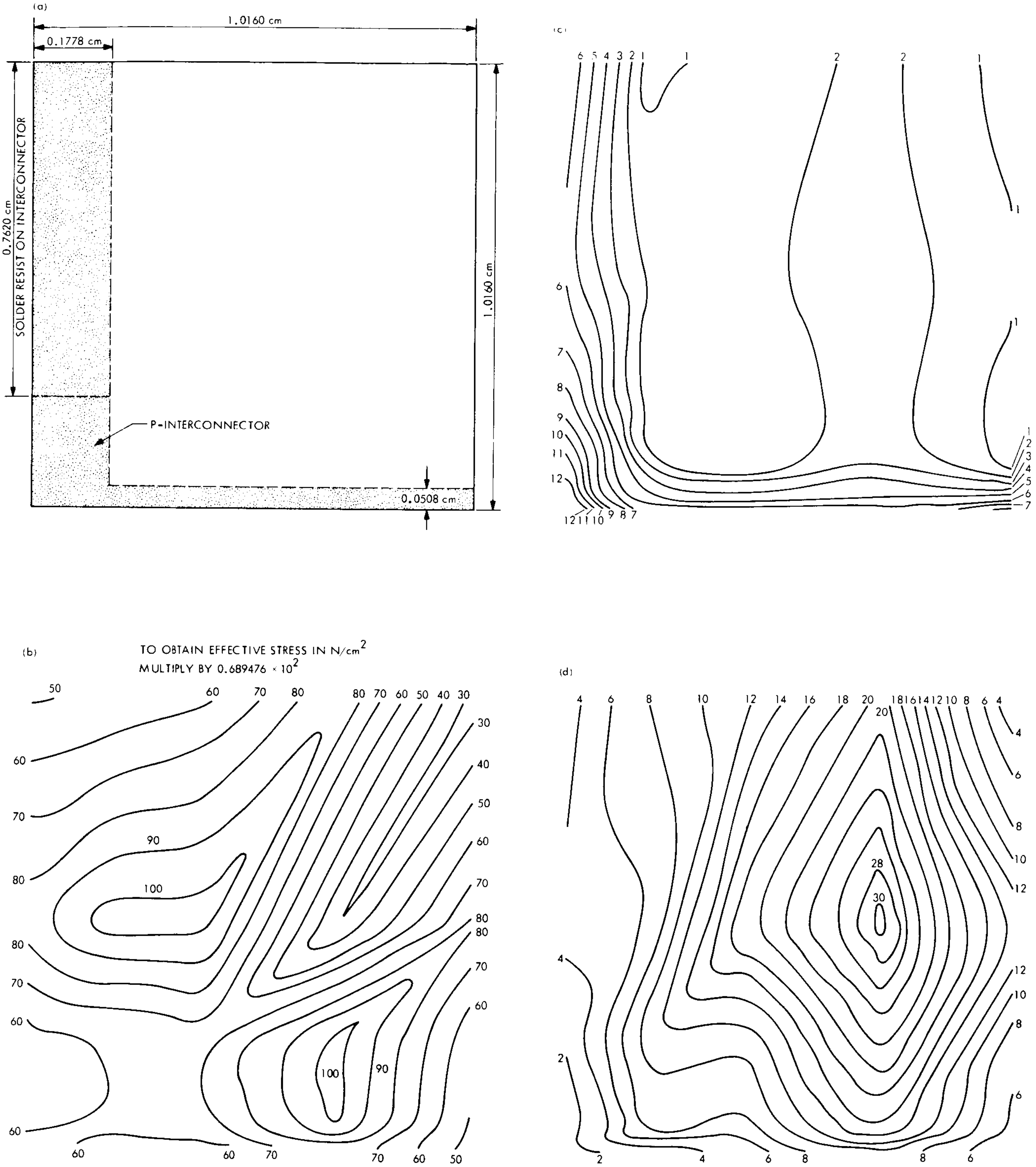

Fig. 43. Effective stresses for configuration Al-6 at -185 °C: (a) overall geometry and dimensions of segment (1), (b) filter, (c) filter adhesive, (d) silicon cell, (e) solder, (f) P-interconnector and adhesive, (g) cell-to-substrate adhesive

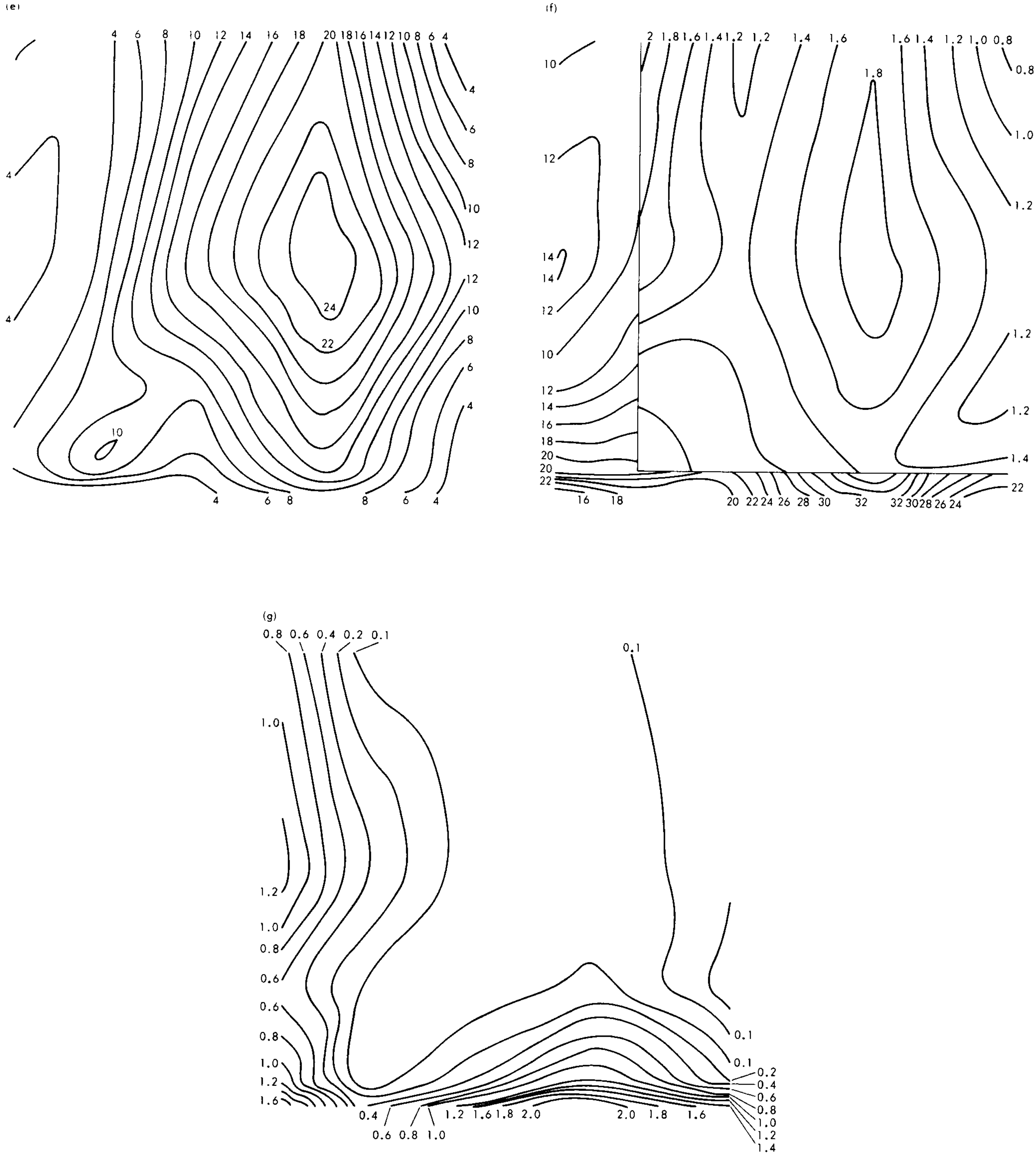
(e)
4 6 8 10 12 14 16 18 20 18 16 14 12 10 8 6 4
4 6 8 10 12 12 10 8 6 4
4
4
10
24
22
4 6 8 8 6 4
(f)
2 1.8 1.6 1.4 1.2 1.2 1.4 1.6 1.6 1.4 1.2 1.0 0.8
0.8 1.0 1.2 1.2 1.2 1.4 22
1.8
10 12 14 14 12 10 12 14 16 18 20 20 22
16 18 20 22 24 26 28 30 32 32 30 28 26 24
(g)
0.8 0.6 0.4 0.2 0.1
0.1
1.0
1.2 1.0 0.8 0.6 0.6 0.8 1.0 1.2 1.6
0.1 0.1 0.2 0.4 0.6 0.8 1.0 1.2 1.4
0.4 0.6 0.8 1.0 1.2 1.6 1.8 2.0 2.0 1.8 1.6

Fig. 43 (contd)

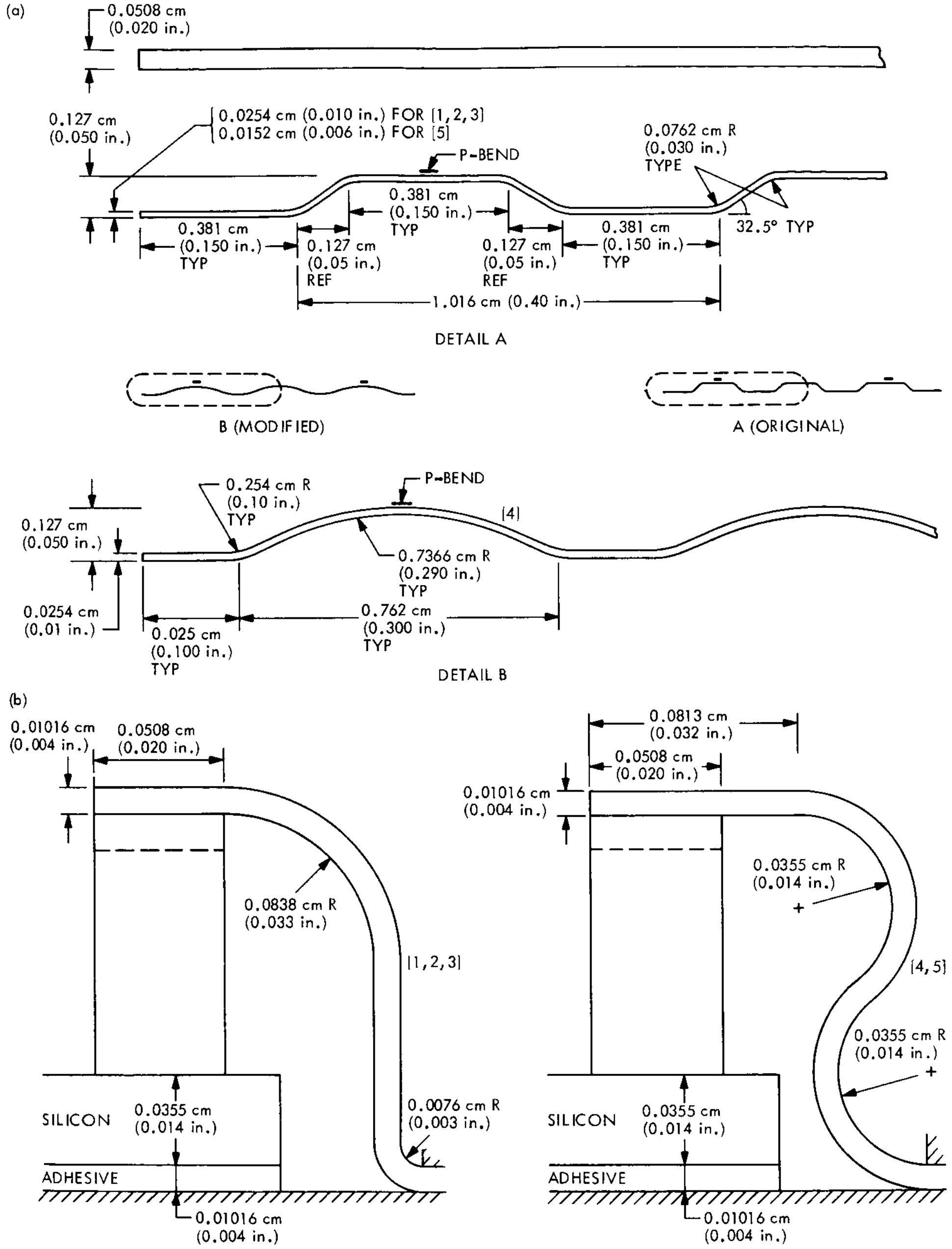

ORIGINAL P-INTERCONNECT BEND GEOMETRY

MODIFIED P-INTERCONNECT BEND GEOMETRY

NUMBERS IN BRACKETS CORRESPOND TO CONFIGURATION NUMBERS IN TABLE 8

MATERIAL OF BOTH P AND N-INTERCONNECTORS FOR [1,4,5] IS Sn-PLATED KOVAR, AND IS PURE PALLADIUM FOR [2,3]

SILICON WAFTER IS P-TYPE SILICON

RTV-41 ADHESIVE IS USED FOR CONFIGURATION [3] ONLY, AND RTV-560 ADHESIVE IS USED FOR [1,2,4,5]

Fig. 44. Interconnector geometries: (a) two N-interconnector bends, (b) P-interconnector bend

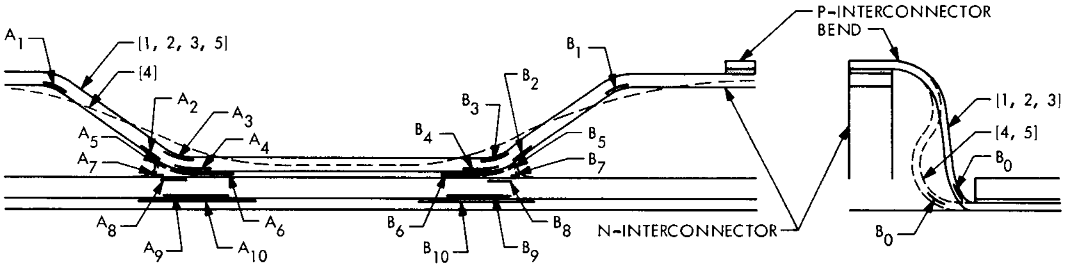

NUMBERS IN BRACKETS REFER TO TABLE 8 DATA

Fig. 45. Highly stressed areas in the neighborhood of the N-interconnector and P-interconnector bend

APPENDIX A. LISTING OF INPUT DATA FOR VISCEL COMPUTER PROGRAM (See Fig. A-1)

```
C
C         FILE ASSIGNMENT AND CONTROL CARDS FOR UNIVAC 1108 SYSTEM.
C
-DELETE,C LISTER
-ASG,T LISTER,F
-DATA,IL LISTER,,LISTEX
-HDG,P  SET A-1/6,1/4 CELL M71,3P COATED -25,-50,-75,-100,-125,-150,-185
-MSG, READ TAPE D198
-ASG,T TAPE,T,D198R
-FREE TPF$
-ASG,T TPF$,F///300
-COPY,G TAPE,TPF$
-FREE TAPE
-ASG,T    4,F2///1000
-ASG,T   10,F2///1000
-ASG,T   11,F2///1000
-ASG,T   12,F2///1000
-ASG,T   13,F2///1000
-ASG,T   14,F2///1000
-ASG,T   15,F2///1000
-FOR,S COMBK,COMBK,COMBK
 2,2
      PARAMETER LDATA=50000
-FOR,S MAIN,MAIN,MAIN
 2,2
      PARAMETER LDATA=50000
-PACK
-PREP
-MAP,EN MAPEL,ABSEL
-XQT ABSEL


C
C         BEGIN DATA
C


C
C         PROBLEM TITLE.
C
        SET A-1/6,1/4 CELL M71,3/P  COATED
C
C         PROBLEM CONTROL PARAMETERS.
C
 204 1123 1080 111          7   1                40      23
C
C         INITIALIZE MATERIAL PROPERTIES FOR STEP ZERO.
C
 1 19.0 E6 7.1  E6 6.5 E-6 2 3.5  E6 1.24 E6 22. E-6 3 18.0 E6 7.03 E6 2.0 E-6
 4 2.3  E2 .78  E2 220.E-6 5 .121 E6 .045 E6 22. E-6 6 10.3 E6 4.45 E6 .54 E-6
 7 1.8  E2 .62  E2 300.E-6
 1  0.
C
C         GRID POINTS COORDINATE DEFINITION.
C
   1   -.00          .40          .0237      2    -.12          .40          .0237
   3   -.24          .40          .0237      4    -.33          .40          .0237
   5   -.40          .40          .0237      6    -.00          .20          .0237
   7   -.12          .20          .0237      8    -.24          .20          .0237
   9   -.33          .20          .0237     10    -.40          .20          .0237
  11   -.00          .10          .0237     12    -.12          .10          .0237
  13   -.24          .10          .0237     14    -.33          .10          .0237
  15   -.40          .10          .0237     16    -.00          .02          .0237
  17   -.12          .02          .0237     18    -.24          .02          .0237
  19   -.33          .02          .0237     20    -.40          .02          .0237
  21   -.00          .00          .0237     22    -.12          .00          .0237
  23   -.24          .00          .0237     24    -.33          .00          .0237
  25   -.40          .00          .0237     26    -.00          .40          .0171
  27   -.12          .40          .0171     28    -.24          .40          .0171
  29   -.33          .40          .0171     30    -.40          .40          .0171
  31   -.00          .20          .0171     32    -.12          .20          .0171
  33   -.24          .20          .0171     34    -.33          .20          .0171
  35   -.40          .20          .0171     36    -.00          .10          .0171
  37   -.12          .10          .0171     38    -.24          .10          .0171
  39   -.33          .10          .0171     40    -.40          .10          .0171
  41   -.00          .02          .0171     42    -.12          .02          .0171
  43   -.24          .02          .0171     44    -.33          .02          .0171
  45   -.40          .02          .0171     46    -.00          .00          .0171
  47   -.12          .00          .0171     48    -.24          .00          .0171
  49   -.33          .00          .0171     50    -.40          .00          .0171
  51   -.00          .40          .017      52    -.12          .40          .017
  53   -.24          .40          .017      54    -.33          .40          .017
  55   -.40          .40          .017      56    -.00          .20          .017
  57   -.12          .20          .017      58    -.24          .20          .017
  59   -.33          .20          .017      60    -.40          .20          .017
  61   -.00          .10          .017      62    -.12          .10          .017
  63   -.24          .10          .017      64    -.33          .10          .017
  65   -.40          .10          .017      66    -.00          .02          .017
```

```
  67   -.12        .02        .017     68   -.24        .02        .017
  69   -.33        .02        .017     70   -.40        .02        .017
  71   -.00        .00        .017     72   -.12        .00        .017
  73   -.24        .00        .017     74   -.33        .00        .017
  75   -.40        .00        .017     76   -.00        .40        .007
  77   -.12        .40        .007     78   -.24        .40        .007
  79   -.33        .40        .007     80   -.40        .40        .007
  81   -.00        .20        .007     82   -.12        .20        .007
  83   -.24        .20        .007     84   -.33        .20        .007
  85   -.40        .20        .007     86   -.00        .10        .007
  87   -.12        .10        .007     88   -.24        .10        .007
  89   -.33        .10        .007     90   -.40        .10        .007
  91   -.00        .02        .007     92   -.12        .02        .007
  93   -.24        .02        .007     94   -.33        .02        .007
  95   -.40        .02        .007     96   -.00        .00        .007
  97   -.12        .00        .007     98   -.24        .00        .007
  99   -.33        .00        .007    100   -.40        .00        .007
 101   -.33        .40        .005    102   -.40        .40        .005
 103   -.33        .20        .005    104   -.40        .20        .005
 105   -.00        .40        .005    106   -.12        .40        .005
 107   -.24        .40        .005    108   -.33        .40        .005
 109   -.40        .40        .005    110   -.00        .20        .005
 111   -.12        .20        .005    112   -.24        .20        .005
 113   -.33        .20        .005    114   -.40        .20        .005
 115   -.00        .10        .005    116   -.12        .10        .005
 117   -.24        .10        .005    118   -.33        .10        .005
 119   -.40        .10        .005    120   -.00        .02        .005
 121   -.12        .02        .005    122   -.24        .02        .005
 123   -.33        .02        .005    124   -.40        .02        .005
 125   -.00        .00        .005    126   -.12        .00        .005
 127   -.24        .00        .005    128   -.33        .00        .005
 129   -.40        .00        .005    130   -.00        .40        .0008
 131   -.12        .40        .0008   132   -.24        .40        .0008
 133   -.33        .40        .0008   134   -.40        .40        .0008
 135   -.00        .20        .0008   136   -.12        .20        .0008
 137   -.24        .20        .0008   138   -.33        .20        .0008
 139   -.40        .20        .0008   140   -.00        .10        .0008
 141   -.12        .10        .0008   142   -.24        .10        .0008
 143   -.33        .10        .0008   144   -.40        .10        .0008
 145   -.00        .02        .0008   146   -.12        .02        .0008
 147   -.24        .02        .0008   148   -.33        .02        .0008
 149   -.40        .02        .0008   150   -.00        .00        .0008
 151   -.12        .00        .0008   152   -.24        .00        .0008
 153   -.33        .00        .0008   154   -.40        .00        .0008
 155   -.00        .40        .000    156   -.12        .40        .000
 157   -.24        .40        .000    158   -.33        .40        .000
 159   -.40        .40        .000    160   -.00        .20        .000
 161   -.12        .20        .000    162   -.24        .20        .000
 163   -.33        .20        .000    164   -.40        .20        .000
 165   -.00        .10        .000    166   -.12        .10        .000
 167   -.24        .10        .000    168   -.33        .10        .000
 169   -.40        .10        .000    170   -.00        .02        .000
 171   -.12        .02        .000    172   -.24        .02        .000
 173   -.33        .02        .000    174   -.40        .02        .000
 175   -.00        .00        .000    176   -.12        .00        .000
 177   -.24        .00        .000    178   -.33        .00        .000
 179   -.40        .00        .000    180   -.00        .40       -.850
 181   -.12        .40       -.850    182   -.24        .40       -.850
 183   -.33        .40       -.850    184   -.40        .40       -.850
 185   -.00        .20       -.850    186   -.12        .20       -.850
 187   -.24        .20       -.850    188   -.33        .20       -.850
 189   -.40        .20       -.850    190   -.00        .10       -.850
 191   -.12        .10       -.850    192   -.24        .10       -.850
 193   -.33        .10       -.850    194   -.40        .10       -.850
 195   -.00        .02       -.850    196   -.12        .02       -.850
 197   -.24        .02       -.850    198   -.33        .02       -.850
 199   -.40        .02       -.850    200   -.00        .00       -.850
 201   -.12        .00       -.850    202   -.24        .00       -.850
 203   -.33        .00       -.850    204   -.40        .00       -.850
C
C          DISPLACEMENT BOUNDARY CONDITIONS.
C
   51   51          101  101          151  151          201  201          212  212
  222  222          232  232          242  242          251  251          252  252
  301  301          351  351          401  401          451  451          462  462
  472  472          482  482          492  492          501  501          502  502
  551  551          601  601          651  651          701  701          712  712
  722  722          732  732          742  742          751  751          752  752
  801  801          851  851          901  901          951  951          962  962
  972  972          982  982          992  992         1001 1001         1002 1002
 1013 1083 1.      1021 1021         1023 1093 1.     1033 1133 1.      1041 1041
 1043 1143 1.      1091 1091         1141 1141         1191 1191         1241 1241
 1252 1252         1262 1262         1272 1272         1282 1282         1291 1291
 1292 1292         1341 1341         1391 1391         1441 1441         1491 1491
 1502 1502         1512 1512         1522 1522         1532 1532         1541 1541
 1542 1542         1591 1591         1641 1641         1691 1691         1741 1741
 1752 1752         1762 1762         1772 1772         1782 1782         1791 1791
 1792 1792         1803 1803         1813 1813         1823 1823         1833 1833
 1841 1841         1843 1843         1853 1853         1863 1863         1873 1873
 1883 1883         1891 1891         1893 1893         1903 1903         1913 1913
 1923 1923         1933 1933         1941 1941         1943 1943         1953 1953
 1963 1963         1973 1973         1983 1983         1991 1991         1993 1993
```

```
 2002 2002         2003 2003         2012 2012         2013 2013         2022 2022
 2023 2023         2032 2032         2033 2033         2041 2041         2042 2042
 2043 2043
C
C       ELEMENT DEFINITION.
C
-  11006    1   1   6   7   2  32  31  26  27
-  21006    1   2   7   8   3  33  32  27  28
-  31006    1   3   8   9   4  34  33  28  29
-  41006    1   4   9  10   5  35  34  29  30
-  51006    1   6  11  12   7  37  36  31  32
-  61006    1   7  12  13   8  38  37  32  33
-  71006    1   8  13  14   9  39  38  33  34
-  81006    1   9  14  15  10  40  39  34  35
-  91006    1  11  16  17  12  42  41  36  37
  101006    1  12  17  18  13  43  42  37  38
  111006    1  13  18  19  14  44  43  38  39
  121006    1  14  19  20  15  45  44  39  40
  131006    1  16  21  22  17  47  46  41  42
  141006    1  17  22  23  18  48  47  42  43
  151006    1  18  23  24  19  49  48  43  44
  161006    1  19  24  25  20  50  49  44  45
  171007    1  26  31  32  27  57  56  51  52
  181007    1  27  32  33  28  58  57  52  53
  191007    1  28  33  34  29  59  58  53  54
  201007    1  29  34  35  30  60  59  54  55
  211007    1  31  36  37  32  62  61  56  57
  221007    1  32  37  38  33  63  62  57  58
  231007    1  33  38  39  34  64  63  58  59
  241007    1  34  39  40  35  65  64  59  60
  251007    1  36  41  42  37  67  66  61  62
  261007    1  37  42  43  38  68  67  62  63
  271007    1  38  43  44  39  69  68  63  64
  281007    1  39  44  45  40  70  69  64  65
  291007    1  41  46  47  42  72  71  66  67
  301007    1  42  47  48  43  73  72  67  68
  311007    1  43  48  49  44  74  73  68  69
  321007    1  44  49  50  45  75  74  69  70
  331003    1  51  56  57  52  82  81  76  77
  341003    1  52  57  58  53  83  82  77  78
  351003    1  53  58  59  54  84  83  78  79
  361003    1  54  59  60  55  85  84  79  80
  371003    1  56  61  62  57  87  86  81  82
  381003    1  57  62  63  58  88  87  82  83
  391003    1  58  63  64  59  89  88  83  84
  401003    1  59  64  65  60  90  89  84  85
  411003    1  61  66  67  62  92  91  86  87

  421003    1  62  67  68  63  93  92  87  88
  431003    1  63  68  69  64  94  93  88  89
  441003    1  64  69  70  65  95  94  89  90
  451003    1  66  71  72  67  97  96  91  92
  461003    1  67  72  73  68  98  97  92  93
  471003    1  68  73  74  69  99  98  93  94
  481003    1  69  74  75  70 100  99  94  95
  491002    1  76  81  82  77 111 110 105 106
  501002    1  77  82  83  78 112 111 106 107
  511002    1  78  83  84  79 113 112 107 108
  521002    1  79  84  85  80 104 103 101 102
  531002    1  81  86  87  82 116 115 110 111
  541002    1  82  87  88  83 117 116 111 112
  551002    1  83  88  89  84 118 117 112 113
  561002    1  84  89  90  85 119 118 103 104
  571002    1  86  91  92  87 121 120 115 116
  581002    1  87  92  93  88 122 121 116 117
  591002    1  88  93  94  89 123 122 117 118
  601002    1  89  94  95  90 124 123 118 119
  611002    1  91  96  97  92 126 125 120 121
  621002    1  92  97  98  93 127 126 121 122
  631002    1  93  98  99  94 128 127 122 123
  641002    1  94  99 100  95 129 128 123 124
  651004    1 105 110 111 106 136 135 130 131
  661004    1 106 111 112 107 137 136 131 132
  671004    1 107 112 113 108 138 137 132 133
  681001    1 108 113 114 109 139 138 133 134
  691004    1 110 115 116 111 141 140 135 136
  701004    1 111 116 117 112 142 141 136 137
  711004    1 112 117 118 113 143 142 137 138
  721001    1 113 118 119 114 144 143 138 139
  731004    1 115 120 121 116 146 145 140 141
  741004    1 116 121 122 117 147 146 141 142
  751004    1 117 122 123 118 148 147 142 143
  761001    1 118 123 124 119 149 148 143 144
  771001    1 120 125 126 121 151 150 145 146
  781001    1 121 126 127 122 152 151 146 147
  791001    1 122 127 128 123 153 152 147 148
  801001    1 123 128 129 124 154 153 148 149
  811004    1 130 135 136 131 161 160 155 156
  821004    1 131 136 137 132 162 161 156 157
  831004    1 132 137 138 133 163 162 157 158
  841004    1 133 138 139 134 164 163 158 159
  851004    1 135 140 141 136 166 165 160 161
  861004    1 136 141 142 137 167 166 161 162
```

```
  871004   1 137 142 143 138 168 167 162 163
  881004   1 138 143 144 139 169 168 163 164
  891004   1 140 145 146 141 171 170 165 166
  901004   1 141 146 147 142 172 171 166 167
  911004   1 142 147 148 143 173 172 167 168
  921004   1 143 148 149 144 174 173 168 169
  931004   1 145 150 151 146 176 175 170 171
  941004   1 146 151 152 147 177 176 171 172
  951004   1 147 152 153 148 178 177 172 173
  961004   1 148 153 154 149 179 178 173 174
  971005   1 155 160 161 156 186 185 180 181
  981005   1 156 161 162 157 187 186 181 182
  991005   1 157 162 163 158 188 187 182 183
 1001005   1 158 163 164 159 189 188 183 184
 1011005   1 160 165 166 161 191 190 185 186
 1021005   1 161 166 167 162 192 191 186 187
 1031005   1 162 167 168 163 193 192 187 188
 1041005   1 163 168 169 164 194 193 188 189
 1051005   1 165 170 171 166 196 195 190 191
 1061005   1 166 171 172 167 197 196 191 192
 1071005   1 167 172 173 168 198 197 192 193
 1081005   1 168 173 174 169 199 198 193 194
 1091005   1 170 175 176 171 201 200 195 196
 1101005   1 171 176 177 172 202 201 196 197
 1111005   1 172 177 178 173 203 202 197 198
 1121005   1 173 178 179 174 204 203 198 199
                                                                          1END
C
C       TABLES OF MATERIAL PROPERTIES AND TEMPERATURE CHANGES FOR
C       STEPS 1,2,3,4,5,6,7.
C
                          7   1
 1 19.0 E6 7.1  E6 6.5 E-6 2 3.5  E6 1.24 E6 22. E-6 3 18.0 E6 7.03 E6 2.0 E-6
 4 2.3  E2 .78  E2 220.E-6 5 .121 E6 .045 E6 22. E-6 6 10.3 E6 4.45 E6 .54 E-6
 7 1.8  E2 .62  E2 300.E-6
 1 -25.
                                                                          1END
                          7   1
 1 19.0 E6 7.1  E6 6.5 E-6 2 3.5  E6 1.24 E6 22. E-6 3 18.0 E6 7.03 E6 2.0 E-6
 4 2.4  E2 .82  E2 220.E-6 5 .121 E6 .045 E6 22. E-6 6 10.3 E6 4.45 E6 .54 E-6
 7 1.7  E2 .59  E2 290.E-6
 1 -25.
                                                                          1END
                          7   1
 1 19.0 E6 7.0  E6 6.5 E-6 2 5.5  E6 1.96 E6 21. E-6 3 18.0 E6 7.00 E6 1.3 E-6
 4 2.7  E2 1.02 E2 200.E-6 5 .126 E6 .047 E6 19.5E-6 6 10.2 E6 4.4  E6 .40 E-6
 7 2.2  E2 .77  E2 275.E-6
 1 -25.
                                                                          1END
                          7   1
 1 19.0 E6 7.00 E6 6.5 E-6 2 5.5  E6 1.96 E6 21. E-6 3 18.0 E6 7.00 E6 1.3 E-6
 4 3.7  E2 1.46 E2 175.E-6 5 .126 E6 .047 E6 19.5E-6 6 10.2 E6 4.4  E6 .40 E-6
 7 6.0  E2 2.11 E2 260.E-6
 1 -25.
                                                                          1END
                          7   1
 1 18.9 E6 6.9  E6 6.5 E-6 2 6.5  E6 2.32 E6 18. E-6 3 18.0 E6 6.98 E6 0.2 E-6
 4 1.0  E3 .446 E3 140.E-6 5 .134 E6 .050 E6 16.5E-6 6 10.0 E6 4.35 E6 0.16E-6
 7 2.5  E3 .919 E3 330.E-6
 1 -25.
                                                                          1END
                          7   1
 1 18.9 E6 6.9  E6 6.5 E-6 2 6.5  E6 2.32 E6 18. E-6 3 18.0 E6 6.98 E6 0.2 E-6
 4 3.5  E3 1.59 E3  90.E-6 5 .134 E6 .050 E6 16.5E-6 6 10.0 E6 4.35 E6 0.16E-6
 7 1.2  E4 0.5  E4 180.E-6
 1 -25.
                                                                          1END
                          7   1
 1 18.8 E6 6.9  E6 6.5 E-6 2 7.0  E6 2.51 E6 16. E-6 3 18.0 E6 6.97 E6-0.9 E-6
 4 5.0  E4 2.27 E4  20.E-6 5 .143 E6 .054 E6 11. E-6 6 9.80 E6 4.30 E6-0.7 E-6
 7 1.0  E5 .454 E5  20.E-6
 1  -35.
                                                                            END
-END LISTEX
-ADD LISTER.
-FIN                                                                       NIF-
```

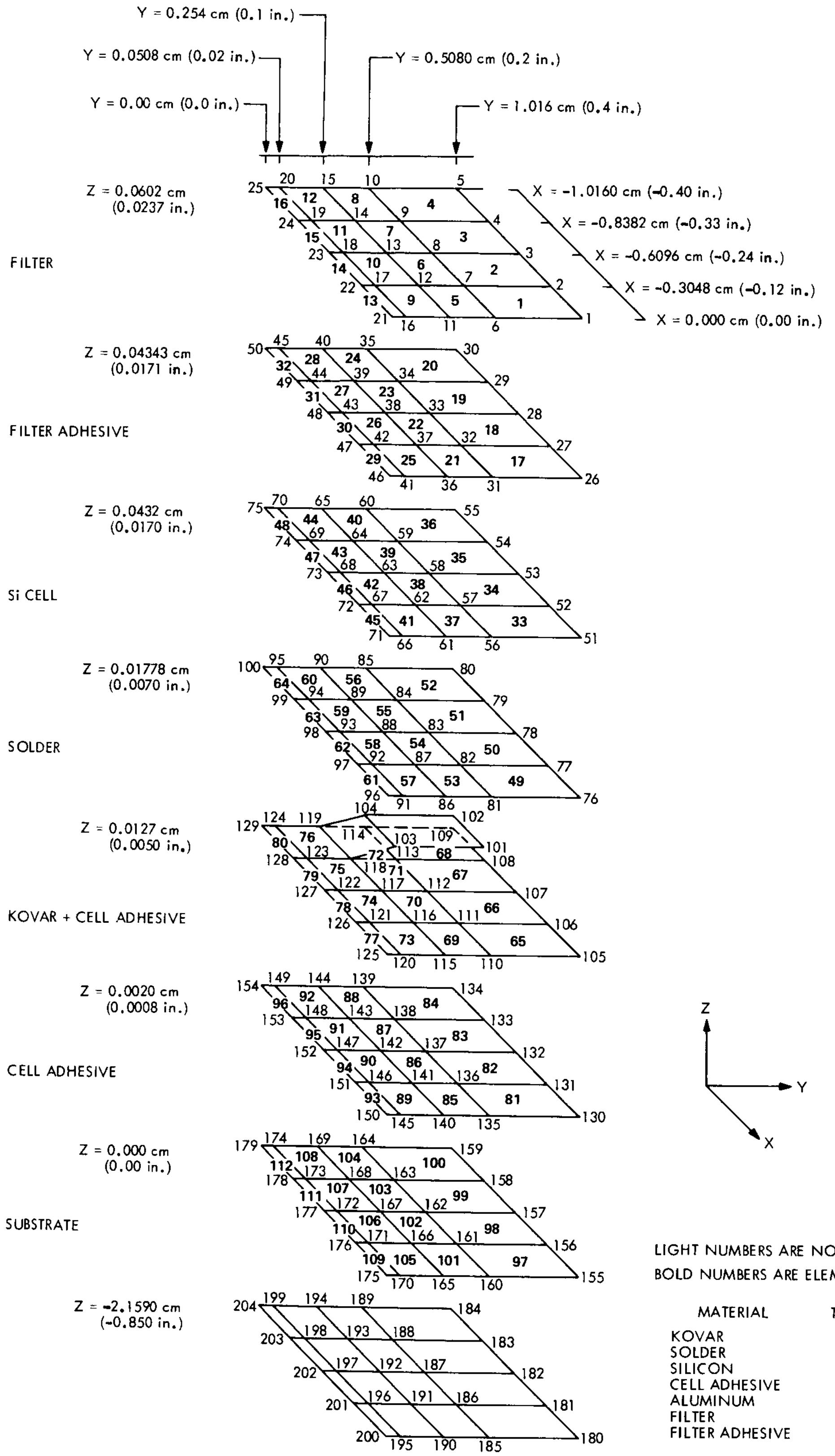

LIGHT NUMBERS ARE NODES
BOLD NUMBERS ARE ELEMENTS

MATERIAL	TYPES
KOVAR	1
SOLDER	2
SILICON	3
CELL ADHESIVE	4
ALUMINUM	5
FILTER	6
FILTER ADHESIVE	7

Fig. A-1. Solder-coated Al-6 configuration, cell interior segment (1) model

APPENDIX B. MECHANICAL PROPERTY SPECIMEN PREPARATION AND TEST PROCEDURE FOR SINGLE-CRYSTAL SILICON

I. Specimen Preparation

The P- and N- type, solar cell grade, single-crystal silicon rods were obtained from Centralab, Division of Globe-Union, Inc., and Heliotek Division of Textron, Inc. The compressive specimen blanks were 2.54 cm (1.0 in.) in diameter by 6.86 cm (2.7 in.) in length. The tensile specimen blanks were 1.52 cm (0.6 in.) in diameter by 10.67 cm (4.2 in.) in length. Thirty specimen blanks were obtained, fifteen from each of the two suppliers. The numbers and types of materials received are shown below:

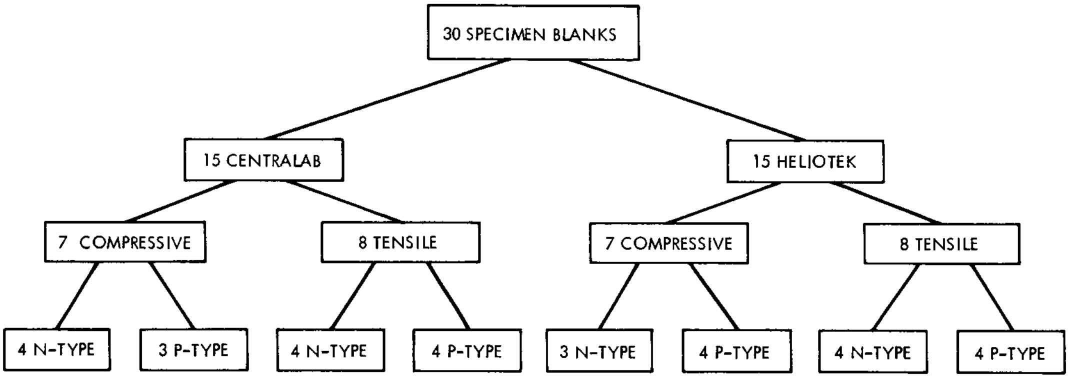

Specimen blanks were machined using 100 grit diamond grinding wheels. Tensile specimen blanks were machined to the configurations shown in Fig. B-1. Compressive specimen blanks were machined to the configuration shown in Fig. B-2.

The blanks were subjected to nondestructive testing (NDT) evaluations consisting of bulk density and sonic velocity determinations to ascertain the quality of the material prior to any machining. The sonic velocities of the P-type specimens were found to be significantly lower than those of the N-type. This relates to the orientation of the crystals.

One specimen from each of the groups was randomly chosen for precision elastic limit (PEL) tests. The two tensile PEL specimens were machined to the configuration shown in Fig. B-1, except that the gauge diameter was 0.42 cm (0.165 in.). Tensile specimens for the remainder of the program were machined to the configuration shown in Fig. B-1. The compressive specimens for the nondestructive evaluations were machined to the configuration shown in Fig. B-2. After nondestructive testing, the gauge section of the compressive specimens was reduced to 0.90 cm (0.354 in.) before ultimate strength evaluations.

Chemical polishing of the ground surfaces of the specimens with a nitric acid-hydrofluoric acid solution was necessary to remove the residual stresses from the grinding operations. The grip areas of the specimens were masked with wax to prevent material removal in these areas. The resulting surface roughness was 0.193×10^{-3} mm to 0.305×10^{-3} m rms (8 to 12 μin. rms) as opposed to the as-ground surface roughness of 3.05×10^{-3} mm rms (120 μin.)

BLH type FAE-12-12S6 strain gauges were attached to the finished specimens. The adhesive employed was T. Bean, BR 610. Two opposing axial gauges were attached to the tension and compression PEL specimens. Two opposing axial gauges and one lateral gauge were employed on the balance of the specimens.

II. Preliminary Tests

Since the test specimens for elastic modulus and Poisson's ratio determinations required repeated loadings, a limit had to be established below which no permanent changes in material response take place. The precision elastic limit (PEL) at room temperature was used to establish this limit. The PEL in this test program is defined as the stress level to which a material may be loaded and unloaded with no permanent (residual) strain.

A. Tensile PEL Tests

The apparatus used to load the tensile PEL specimens was a modification of a regular gas-bearing tensile facility and is shown in Fig. B-3. The primary components are the gas bearings, the load train, and the instrumentation for monitoring temperature and residual strain.

The spherical gas-bearing permits radial movement of the load train so that the seating surfaces on the chain links remain unchanged for any imbalance which might occur during loading.

The specimen was adapted to the load train by precision collect grips machined concentric to within 0.00127 cm (0.0005 in.). The chains, which connect to the grips and to the weight support platform were attached so that the line of application of the load was coincident with the centerline of the specimen. The load (stress) on the specimen was determined by the dead weight load, which was applied and removed using the lower crosshead (Fig. B-3).

The residual strain of the specimen was monitored using a Wheatstone bridge circuit that consisted of diametrically opposed active gauges on the specimen and two dummy compensator gauges for temperature compensation. Deflection of the galvanometer used for measuring residual strain was calibrated using standard specimens.

One half of the bridge circuit was mounted on a second specimen (dummy) in order to provide temperature compensation. Both specimens were wrapped in Fiberfrax blanket insulation and placed in close proximity to each other in the environmental box. The complete test facility was located in an isolated room with limited access to prevent any abrupt ambient temperature changes. However, even with these precautions it was necessary to monitor carefully the relative temperature difference between the specimen and the dummy since a 0.277°C (0.50°F) change in ΔT gives a strain signal of 1 μin./in. (1×10^{-6} cm/cm). The outputs from the thermocouples were read on a Leeds and Northrup Type K-3 Universal potentiometer.

B. Compressive PEL Tests

The compressive PEL evaluations were run in an apparatus designed especially for this purpose. The fixture is shown in Fig. B-4. An alignment jig with a single-precision hole guides both support and loading rams. Precision balls at each end of the load ram and at the lower end of the support ram help to prevent the introduction of externally applied bending moments into the specimen. Strains due to bending of the silicon specimens were about 2.2% of the strains due to axial loading. Loading was accomplished using dead weights and a lever system which gave a nominal force multiplication of 10:1. Load on the specimen was applied and released by moving the lever a small distance with a supporting screw.

Both tensile and compressive PEL sequencing were essentially the same. Tests were made in an isolated room. The system was assembled, specimens were installed, and several cycles were performed at the lowest load to seat all parts. All parts of the test apparatus were activated and allowed to equilibrate for 24 hours. After entering the room, the test technician waited a half hour, and then monitored the strain gauge and thermocouple data for at least a half hour to measure system drift. Once begun, the tests were run to completion. Load was applied to a specimen for one minute and then removed. Strain gauge and thermocouple data were recorded after one additional minute for equilibration. This cycle was applied three times at each load level. The dead weight load was then increased by 88.9 N (20 lb) and the loading-reading cycle was begun again.

The results of the PEL evaluations (Table B-1) led to the following guidelines for the subsequent nondestructive evaluation for elastic modulus and Poisson's Ratio:

(1) Machine all tensile specimens to 0.33-cm (0.130 in.) gauge diameter and then etch to remove approximately 0.01525 cm (0.006-in.) on the diameter.

(2) Load tensile specimens to a stress of approximately 13,800 N/cm^2 (20,000 psi) or 100×10^{-6} cm/cm (100 μin./in.) lateral strain, whichever occurs first.

(3) Machine compressive specimens to standard 0.127 cm (0.500 in.) gauge diameter and then etch to remove about 0.01525 cm (0.006 in.) from the diameter.

(4) Load compressive specimens to a stress of approximately 17,230 N/cm^2 (25,000 psi).

C. Tensile and Compressive Tests for Elastic Modulus and Poisson's Ratio

The tensile evaluations were conducted in a gas-bearing tensile testing facility. A photograph of the setup is shown in Fig. B-5.

The compressive evaluations were also conducted in a gas-bearing compressive facility. This facility was designed to permit precise alignment of the load train and provide rigid support to the ends of the specimen. A photograph of the gas-bearing compressive facility with a silicon specimen in place is shown in Fig. B-6.

Thermal conditioning of all specimens was accomplished using a two-zone Kanthal furnace for elevated temperature and a liquid-nitrogen-cooled cryogenic chamber for temperatures below room temperature. Temperature gradients were monitored using three thermocouples located at the top, middle, and bottom of the exposed gauge section of the specimen. Temperature gradients (typically 15°C) were greatest at -150°C. The temperature at the strain gauge locations were always within ±3°C of the target temperature.

The strain calibrations for the first few specimens at a given temperature were determined by applying a small static load and reading the strain from a BLH Strain Indicator, Model 120C. At least three stress, axial-strain, and lateral strain versus axial strain plots were then made on the X-Y recorders for each specimen at each temperature evaluated.

After the first 25°C tests on one of the compressive specimens, several radial cracks were discovered in the head of the specimen. Therefore, stress level for the P-type compressive specimens was decreased to 10, 330 N/cm^2 (15, 000 psi). Other precautions, such as the use of a thin sheet of Teflon between the specimen and pushrods to prevent uneven loading due to any possible rough or uneven surfaces were instituted to prevent a recurrence of the premature fracture. The stress level for all tensile testing was lowered to 6, 895 N/cm^2 (10, 000 psi). Compressive testing at cryogenic temperatures was limited to a maximum stress of 10, 330 N/cm^2 (15, 000 psi).

Testing was performed at eight temperatures: -185, -150, -50, -100, 25, 100, 150 and 200°C.

All specimens were tested for elastic modulus and Poisson's ratio at room temperature (25°C). At the other seven temperatures, tests were required from two specimens of each possible combination of supplier, material, type, and test direction. A pseudo-random process was used to assign test temperatures. Tables of random numbers were utilized in making decisions, but within a given group a generally uniform distribution of the number of tests per specimen was forced.

During the course of the testing some specimens were inadvertently broken. The remaining test temperature assignments for the broken specimens were reassigned to the surviving specimens in that group to the extent possible.

After completion of the nondestructive tests for elastic modulus and Poisson's ratio the surviving specimens were loaded to failure at -150 or -100°C to determine ultimate tensile and compressive strength.

Table B-1. Results of PEL evaluations

Specimen	Gauge diameter, cm (in.)	Maximum load, N (lb)	Stress, N/cm^2 (psi)	ΔT^a Range, °C	Drift, Residual Strain, etc., 10^{-6} cm/cm (μin./in.)	Remarks
N-type tensile	0.4069 (0.1602)	1,246 (280)	9,580 (13,890)	0.78-1.04	1.4	Broke in grip. Did not indicate inelastic strain
P-type tensile	0.3167 (0.1247)	1,690 (380)	21,460 (31,120)	1.10-1.47	3.6	Broke in gauge. Did not indicate inelastic strain
N-type compression	0.9030 (0.3555)	31,270 (7029)	-48,820 (-70,815) [132,000]	1.23-1.30	10.2	Did not indicate inelastic strain
P-type compression	0.8997 (0.3542)	39,500 (8880)	-62,120 (-90,100) [-32,200][b]	1.41-1.56	7.3	12 cm × 10^{-6}/cm (μin./in.) jump in residual strain on loading to 38,655 N (8690 lb). Off-scale jump on loading to 39,500 N (8880 lb)

[a] Temperature difference between the specimen being evaluated and the compensation specimen.

[b] Specimen was probably damaged on loading to 62,000 N/cm^2 (90 ksi).

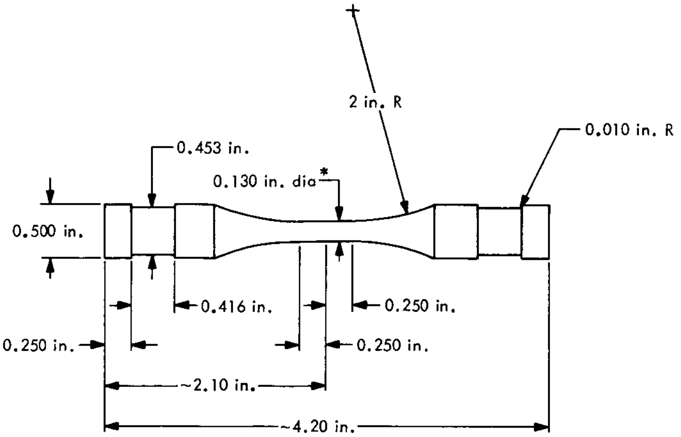

*0.165 in. diam. FOR PEL SPECIMEN

Fig. B-1. Tensile specimen configuration for single-crystal silicon

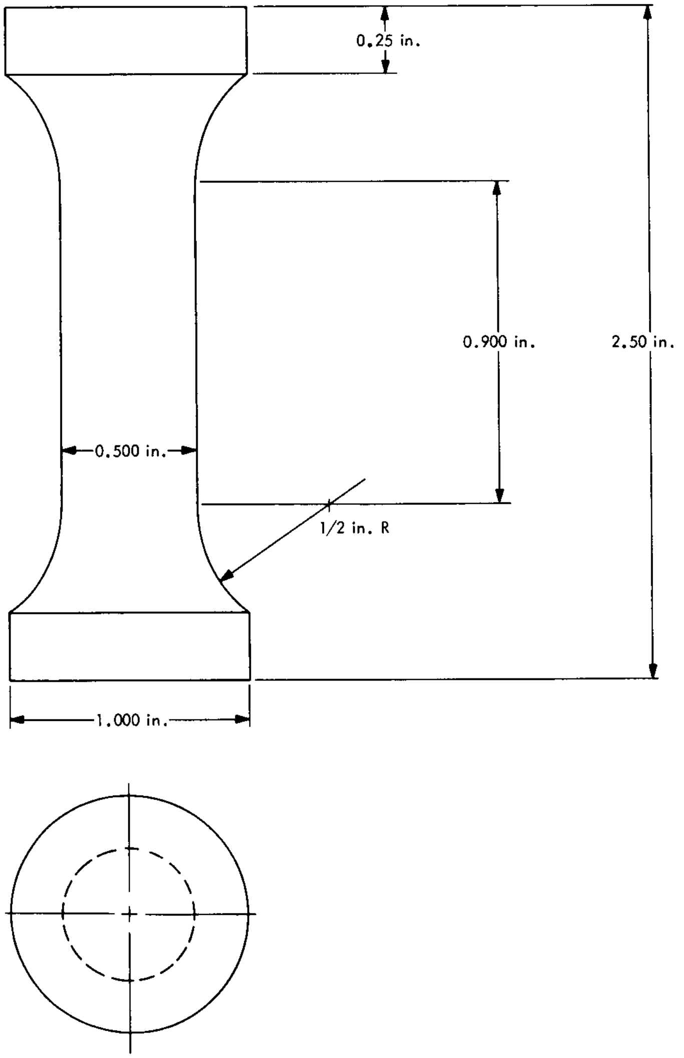

Fig. B-2. Compressive specimen configuration for single-crystal silicon for elastic modulus and Poisson's ratio tests

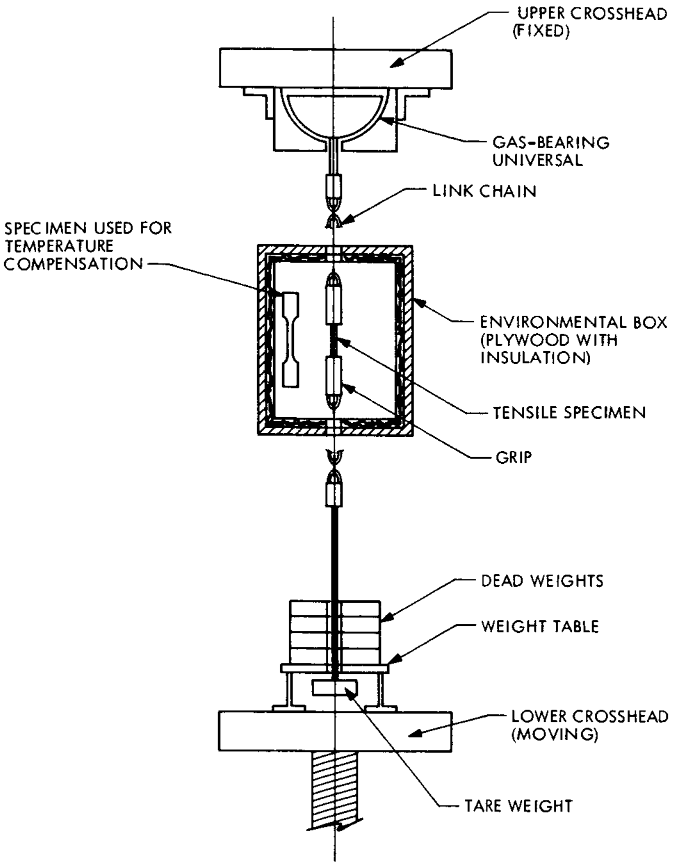

Fig. B-3. Schematic of tensile load train used in PEL evaluations

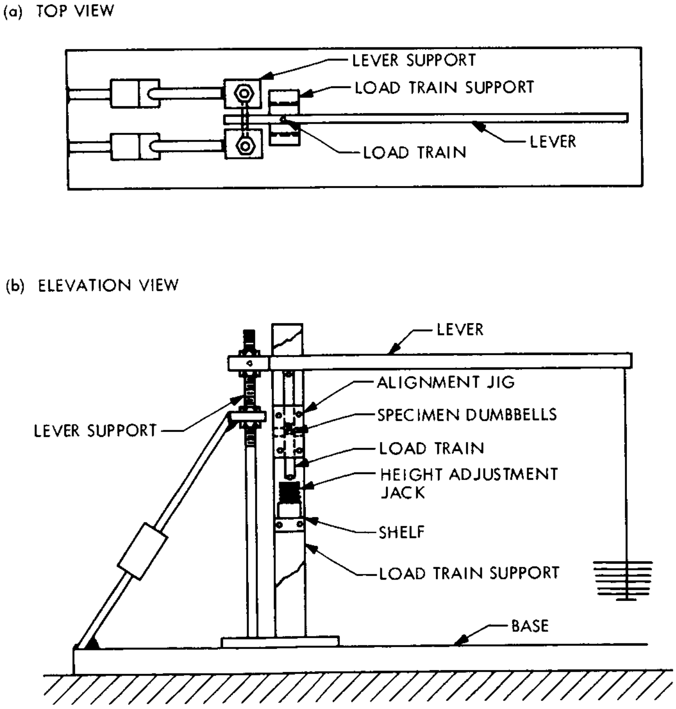

Fig. B-4. Sketch of compressive PEL loading system

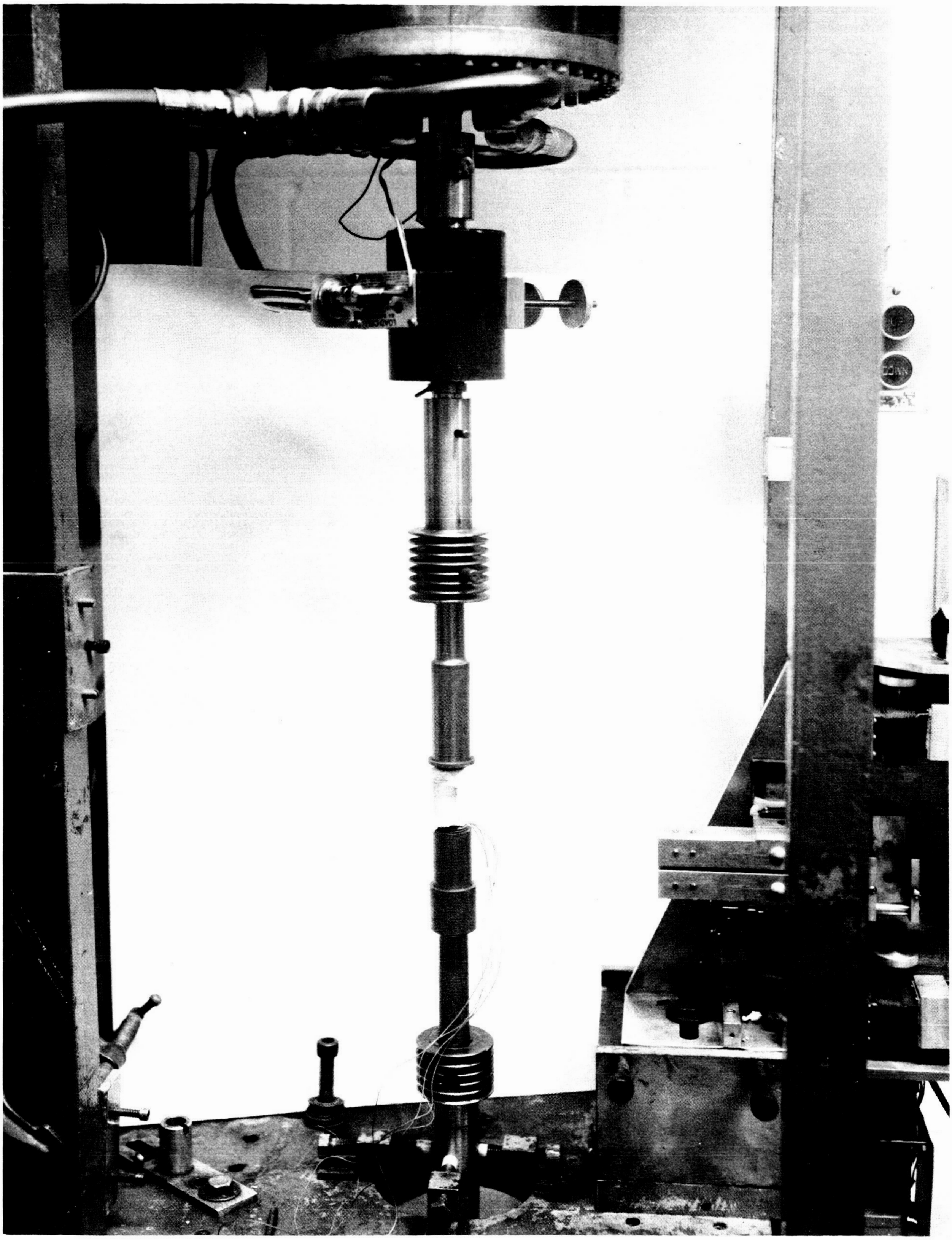

Fig. B-5. Tensile facility setup for evaluation of single-crystal silicon

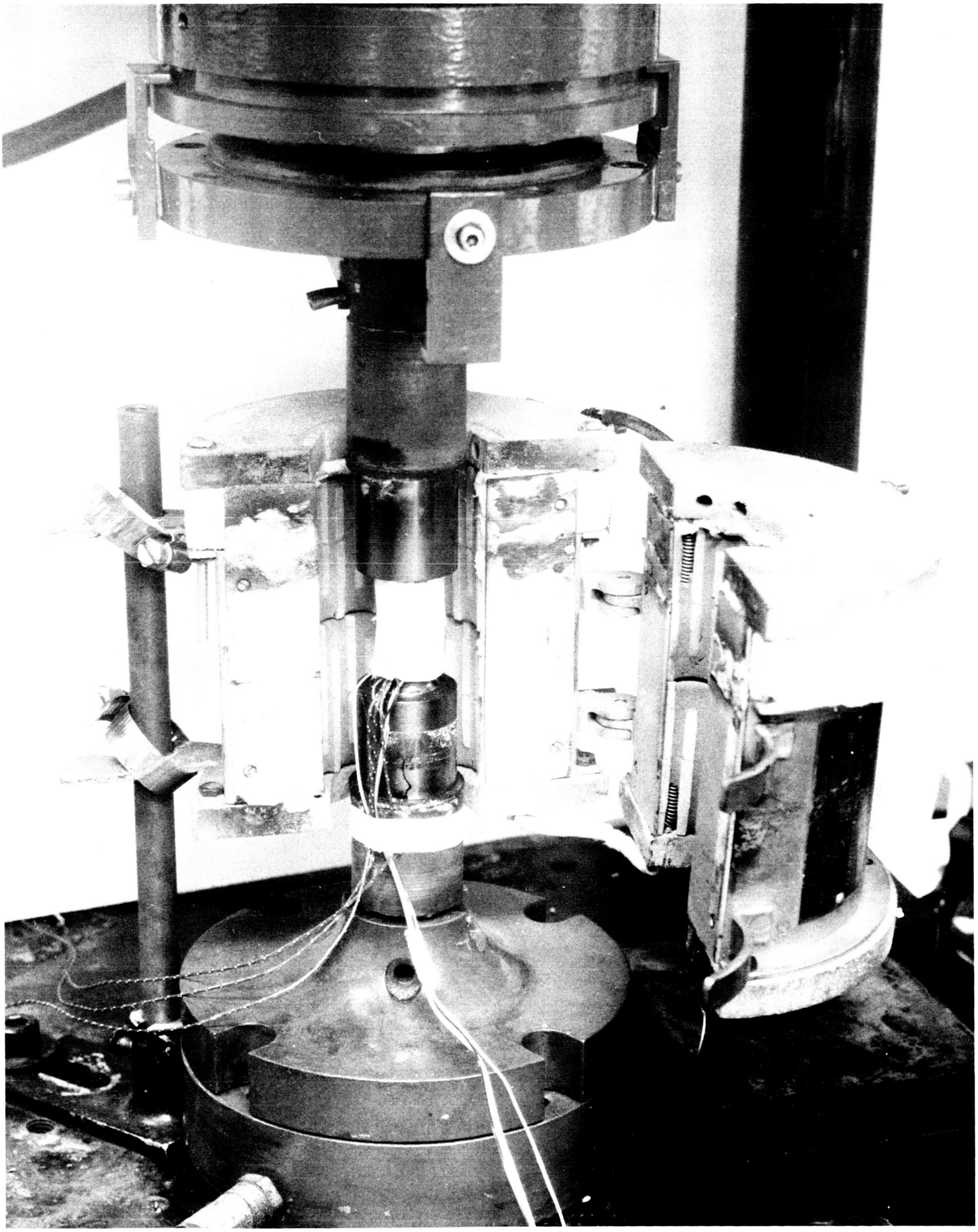

Fig. B-6. Compressive facility setup for evaluation of single-crystal silicon

APPENDIX C. MECHANICAL PROPERTY SPECIMEN PREPARATION AND TEST PROCEDURES FOR RTV SILICONE RUBBER ADHESIVES

I. Materials

Test specimens of seven RTV silicone rubber adhesive materials were prepared by casting and curing either flat sheets or cylindrical rods. The specimens used for determining elastic modulus and ultimate strength in tension were prepared from cast flat sheets of the materials 15.24 × 15.24 × 0.3175 cm (6 × 6 × 0.125 in.).

The specimens used for determining ultimate compressive strength and elastic modulus in compression were vacuum cast in the form of cylindrical rods 1.27 cm (0.5 in.) in diameter by 5.08 cm (2 in.) in length. The specimens for Poisson's ratio determinations were cast as right cylinders with a diameter of 2.868 cm (1.129 in.) and 1.27 cm (0.500 in.) in thickness.

The materials with their respective curing agents are listed in Table C-1. The manufacturer's recommended mix ratios of material to curing agent were followed and deaeration was used to remove entrapped air. The molds used for specimen fabrication were machined from aluminum, with the exception of the ones for the compressive modulus and strength measurements which were cast in 1.27 cm (0.5 in.) ID clear acrylic tubing.

Subsequent to preparing and curing the above materials, they were post-cured for 2 hours at a temperatures of 200°C for thermal stabilization. The 15.24 × 15.24 × 0.3175 cm (6 × 6 × 0.125 in.) sheets were used to fabricate tensile specimens of the die C configuration of ASTM D 412.

II. Testing

The tensile testing was performed on the 2.54-cm (1 in.) gauge length sheet specimens at a crosshead speed of 25.4 cm (10 in.) per minute. An Instron G5101 incremental extensometer was used to measure strains on specimens at test temperatures where the materials were in their normal rubbery state. However, at the subzero temperatures where the materials became stiff and brittle upon reaching crystalline transition temperatures (the dimethyls), or glass transition temperatures (both dimethyl and methyl-phenyl types), a Baldwin PS3M type of extensometer was employed to measure the strains. Stress-strain curves to failure were recorded during tensile testing.

The tests for the strength and elastic modulus in compression were performed with the entire length of the specimen as the gauge length. Baldwin TS MD-1003 extensometers were attached to the load head of the Instron test machine by means of mechanical linkage in such a manner that the strains were measured outside the test chamber. Because of the highly elastic nature of these materials, these specimens were not tested to failure. Instead, they were compressed 20% of their total length, and the load values at these deformations were used to compute the strengths. The elastic modulus values, reported for both tension and compression testing are the initial moduli, i.e., the best fit line to the load curve at the beginning of specimen deformation. The test machine for both tension and compression tests was an Instron, Model TTCM1-4-6, Universal Tester used in conjunction with an environmental chamber. The cryogenic temperatures were obtained through the use of liquid nitrogen.

Because of problems in gripping silicone samples in the three material states (amorphous, crystalline, and glassy) which are present in these materials at the various temperatures of interest, the compressive testing mode was selected for making the measurements for Poisson's ratio. Right circular cylinders were used as test specimens where the ratio of the radial strain to the axial strain would be Poisson's ratio. The aspect ratio of the cylinders, 0.127 cm (0.05 in.) long by 2.868 cm (1.129 in.) in diameter or the ratio of the length-to-diameter, was chosen to be about one-half.

A Missimer's environmental chamber was located in the test machine such that the load cell was below the chamber and the moving crosshead above the chamber. A hollow rod attached to the load cell passed through the bottom of the chamber and a platform was attached to the rod providing a horizontal flat surface on which the specimen was placed. A second rod with a flat polished end attached to the moving crosshead, passed through the top of the environmental chamber. This allowed the specimen to be compressed between two flat parallel plates and the resulting stress to be measured by means of the load cell. The specimen could be viewed through a window in the chamber. Seven parallel layers of glass with air between each layer gave a thermal barrier for the window yet caused no appreciable distortion when the specimen was viewed.

The specimens were photographed with a Super Cambo bellows-type camera which has a 355-mm focal length lens and a bellows length of up to 152.4 cm (60 in.). Kodak PXP 120 Plus-X Pan film was used to provide a 6 × 9 cm negative. This film has the maximum resolution of the commercially available 120 format films.

The desired focal length was calculated to be 362 mm. A commercially available 355-mm lens whose focal length was closest to this value was employed. Also, it was calculated that the image of the object formed by this lens would be 144.78 cm (57 in.) away from the lenses. Therefore, a single lens camera having a 152.4-cm (60 in.) bellows was employed.

Since the edge of the specimen was the part of most interest for photographing, and since light reflects best off a surface when the angle of incidence is low, it was decided to illuminate the specimen from the rear. A flashtube was used for this purpose.

No commercially available flash unit could be found that would withstand the temperature extremes of the tests, so a special unit was fabricated. Figure C-1 schematically depicts the placement of the two flash tubes and the supporting platform. The flash tubes were placed as near as possible to an imaginary line running from the lens of the camera to the edge of the specimen, but not so close that the flash tubes were in the view area of the camera. In this way the angle of incidence of the light on the edge of the specimen was the lowest without all the light from the flash reaching the film. This arrangement gave a negative which was black everywhere except for two fine lines caused by light reflected from the edge of the specimen. The edges of the specimen were easily detected on the film negative with this technique. In addition, a reflector was placed behind each flash tube so that a maximum amount of light was directed toward the edge of the specimen. A baffle was also used to prevent stray light from reaching the camera and reducing film contrast.

The intensity of the light output of flash tubes was selected to allow the aperture of the lens to be approximately one-half open. The lens employed had an aperture range from f9 to f90 and was found to have the best resolution between f22 and f45. General Electric FT-30 flash tubes were used that were powered by the discharge of several 30 μF capacitors, charged to 200 Vdc.

The test procedures employed were as follows: The samples were placed in the environmental chamber and allowed to equilibrate at a given temperature for at least 30 minutes before testing. After this preconditioning, the Instron crosshead was lowered manually just to contact the specimen and the initial height of the samples was noted from the crosshead dials. Two photographs of the sample were then made.

The crosshead was energized to run at the rate of 0.508 cm (0.02 in.) per minute. A photograph was taken every 30-s with the crosshead moving until six photographs had been taken, which resulted in the specimen being strained approximately 10%. The electrical circuitry of the Instron which indicates a measurement point of the recording was energized concurrent with each photo to allow the measurement of the specimen height from the stress-strain curve. Therefore, a total of eight photographs was taken for each specimen at a given temperature.

The above procedure was altered slightly for some of the low temperature tests. To obtain a sufficient number of data points at the low temperatures, photographs were taken at 15-s intervals. This was necessary because, with increased sample stiffness, the specimen load rose rapidly to the capacity of the test machine. In addition, at temperatures below -160°C the flash tubes would not fire and, therefore, photographs could not be taken.

Photographs from all the experimental runs were examined optically with a Nikon comparator. Measurements of the sample diameter on each of the eight photos per run were made on three points along the specimen height.

It was noticed that all samples bulged slightly with increased strain, probably due to end effects on the specimen. To find the average diameter of the sample, a mathematical approximation was devised which took into account sample bulging during stress. From examination of the photographs it was seen that the bulging took the form of a triangle.

After measurement of the sample diameters at various stress levels was completed, a plot was made for each run of the radial strain versus stress and the slope of this plot was calculated. A similar plot of axial strain versus stress for the same run was made from the Instron chart and its slope was calculated. Poisson's ratio was then calculated from the ratio of slopes derived above.

Table C-1. RTV-type silicone rubber materials

Material	Curing agent	Weight % curing agent[a]
RTV 41	Dibutyl-tin-dilaurate	0.5
RTV 511/577	Dibutyl-tin-dilaurate	0.5
RTV 560	Dibutyl-tin-dilaurate	0.5
RTV 566A	RTV 566B (tin octoate type)	0.05
RTV 602	SRC-05 (amine cured)	0.5
DC 93-500	DC 93-500 curing agent (platinum cured)	10
XR 63-489	XR 63-489 curing agent (platinum cured)	10

[a] Per hundred parts by weight of material

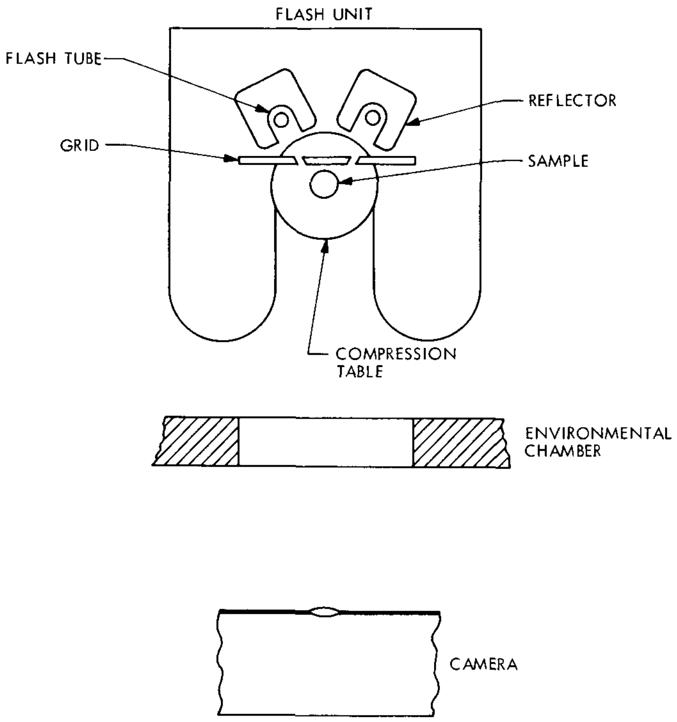

Fig. C-1. Schematic diagram of experimental setup for measuring Poisson's ratio of RTV silicone by photographic technique

APPENDIX D. MECHANICAL PROPERTY SPECIMEN PREPARATION, TEST PROCEDURES, AND DATA ERROR ANALYSIS FOR METAL ALLOY INTERCONNECTOR MATERIAL

I. Specimen Preparation

The materials whose mechanical properties were measured, were Kovar (29Ni-17Co-54Fe), molybdenum, palladium, silver and a lead-tin solder alloy (62Sn-36Pb-2Ag). The materials were all tested in the sheet form in thicknesses of 0.076 cm (0.030 in.), 0.127 cm (0.050 in.) and 0.152 cm (0.060 in.). The specimen configuration is shown in Fig. D-1. All specimens were pin loaded. Test temperatures were -196, -100, -25, 100, 150, and 200°C.

After machining, the specimens were cleaned and two longitudinal and two transverse strain gauges were attached to each. Figure D-2 shows a bare specimen, one with strain gauges attached, and one with lead wires and an acrylic coating over the strain gauges. The smaller strain gauge shown on the left of the specimen was the transverse gauge. The other was the longitudinal gauge.

The strain gauges were manufactured by Micro Measurements, Inc., with the specific type used for each condition described in Table D-1. The numbers and letters in this table are a combination catalog and code number identifying each particular strain gauge. Each material in this program required a slightly different gauge. Specifically, the numbers in the table identify the: (1) strain gauge material, (2) backing material, (3) temperature compensation, (4) gauge length, (5) pattern, and (6) resistance. The cement used in all cases was M-Bond-600.

II. Testing

All tests were conducted with a Baldwin universal hydraulic testing machine. Baldwin strain-gauge load cells applicable to the anticipated load limit for each particular material and temperature were used. Two Ellis bridge amplifiers increased the signal from the two pairs of strain gauges (longitudinal and transverse). An overall view of the test apparatus and setup is shown in Fig. D-3. For the low-temperature (-196, -100, and -25°C) tests, the furnace shown in Fig. D-3 was replaced with a cryostat for holding the cooling medium. The methods used for attaining each low temperature are listed in Table D-1.

The hold time at the subzero temperatures was 10 to 15 minutes, and at the elevated temperatures it was 25 to 30 minutes. The strain gauges were calibrated at temperature immediately prior to testing. Accuracy of the strain gauges is the best at room temperature and approximately equal at the higher and lower temperatures. Temperature control of the specimens was slightly better at low temperatures. Other than at room temperature, the best temperature control was probably at -196°C with the liquid nitrogen bath. In all cases, temperatures were maintained within ±2°C of the desired temperature.

The amplified signal from each pair of strain gauges was fed into a Hewlett-Packard X-Y recorder. Transverse strain was recorded on the ordinate scale and longitudinal strain on the abscissa scale. The slope of the resultant curve gave the Poisson's ratio. At periodic intervals the pen on the X-Y recorder was deflected momentarily to indicate the load level. The load intervals ranged from every quarter pound for solder at 150°C to every 22.7 kg (50 lb) for molybdenum at -196°C. Utilizing these load and longitudinal-strain data, typical stress-strain curves were plotted. Young's modulus, proportional limit, and 0.2% offset-yield data were then obtained from these stress-strain curves.

Most tests were conducted at a strain rate of 0.005 cm/cm/min (0.005 in./in./min) to a little beyond the 0.2% offset strain. Where total elongation was limited, this same strain rate was maintained to rupture. Where considerable ductility was present, the strain rate was increased to about 0.02 to 0.05 cm/cm/min so as to reduce overall test time.

An error analysis was performed on the data obtained using BMDOID "Simple Data Description" program (Ref. 13) on a CDC-6400 digital computer.

Table D-1. Method of obtaining test temperatures and types of strain gauges used

Temperatures		Means of temperature control	Types of strain gauges	
°C	°F		Longitudinal	Transverse
-196	-320	Liquid nitrogen	WK-XX-250BG-350	WK-XX-062AP-350
-100	-148	Liquid nitrogen and isopentane mixture	WK-XX-250BG-350	WK-XX-062AP-350
-25	-13	Methanol and dry ice mixture	EA-XX-250BG-120	EA-XX-062AP-120
+25	77	Ambient conditions	EA-XX-250BG-120	EA-XX-062AP-120
100	212	Resistance wound furnace	EA-XX-250BG-120	EA-XX-062AP-120
150	302	Resistance wound furnace	WK-XX-250BG-350	WK-XX-062AP-350
200	392	Resistance wound furnace	WK-XX-250BG-350	WK-XX-062AP-350

The "XX" in the gauge designations signifies temperature compensation, which was different for each material; solder -13, Ag -09, Pd -06, Mo -03, and Kovar 00.

All gauges were manufactured by Micro Measurements, Inc.

Cement for all specimens was M-Bond-600, a solvent-thinned epoxy.

Data obtained from Battelle Institute, Columbus, Ohio.

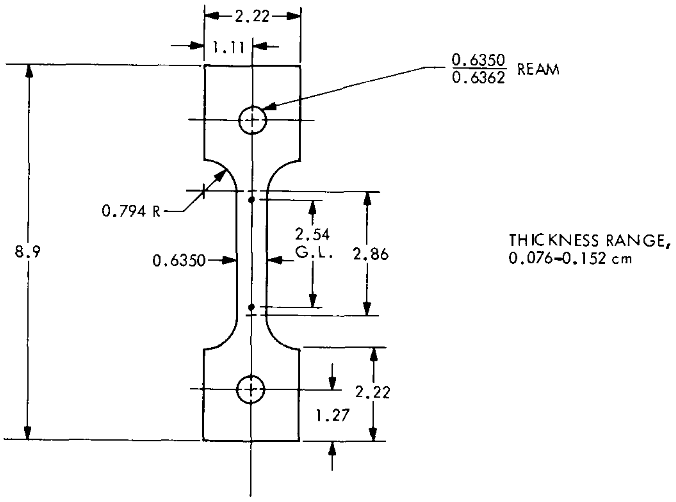

HOLES LOCATED ON AXIS OF REDUCED SECTION TO WITHIN 0.00127 cm

ALL DIMENSIONS IN CENTIMETERS

G.L. = GAUGE LENGTH

Fig. D-1. Test specimen configuration for all materials (data from Battelle Institute, Columbus, Ohio)

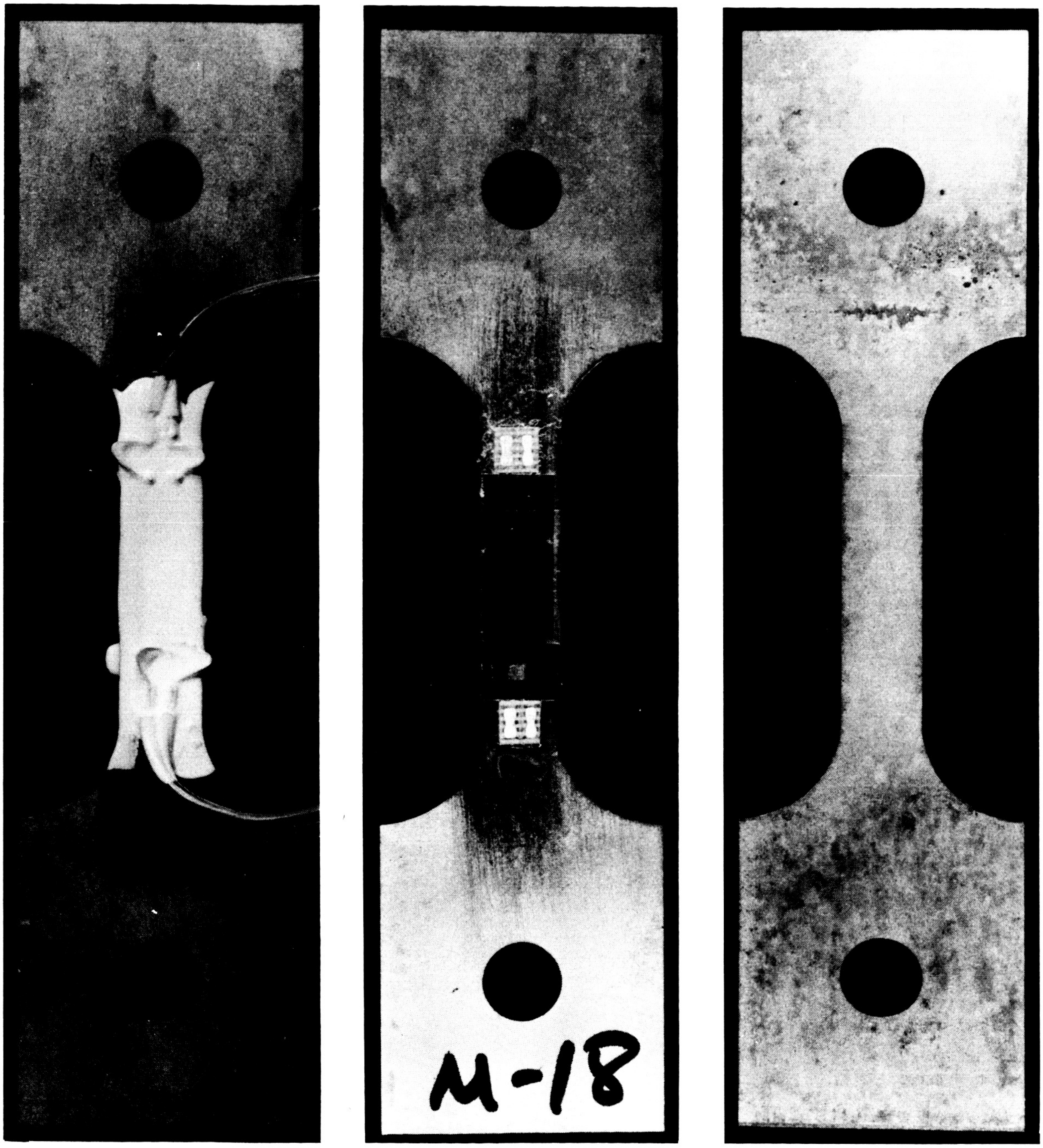

Fig. D-2. Bare specimen, specimen with gauges showing, and specimen with gauges, lead wires, and coating (obtained from Battelle Institute, Columbus, Ohio)

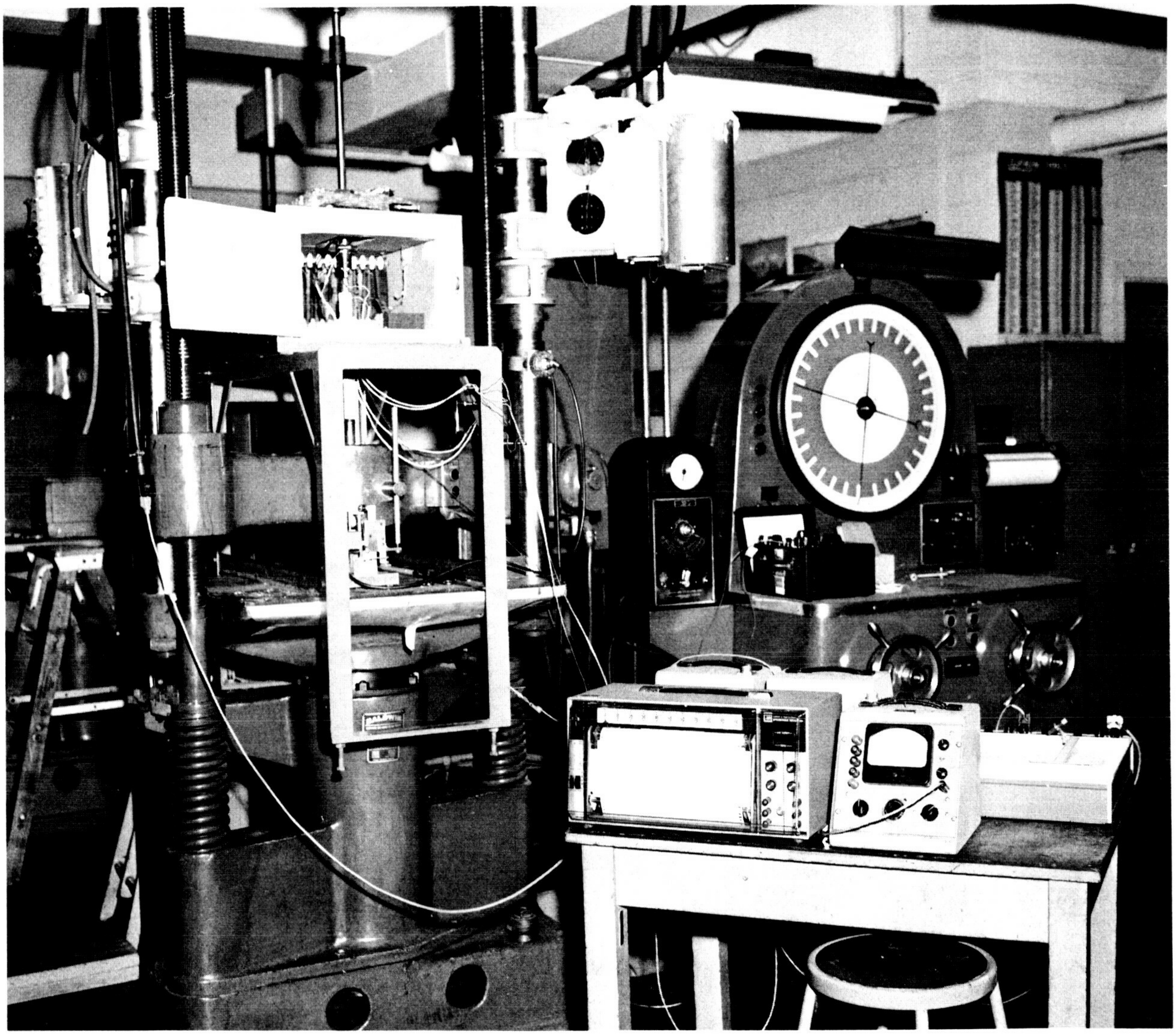

Fig. D-3. Overall view of test apparatus (obtained from Battelle Institute, Columbus, Ohio)

NASA — JPL — Coml., L.A., Calif.